NORSAR ROYAL NORWEGIAN COUNCIL FOR SCIENTIFIC AND INDUSTRIAL RESEARCH

Norsar Technical Report No. 4/81

3-D MAPPING OF THE ICELAND HOT SPOT

by
Kristjan Tryggvason

Kjeller, December 1981

NORSAR Contribution No. 311

3-D MAPPING OF THE ICELAND HOT SPOT

A Thesis in Geophysics

by

Kristjan Tryggvason

University of Oslo
December 1981

ACKNOWLEDGEMENT

The whole NORSAR staff and my colleagues in Iceland, Ragnar Stefansson and Thorunn Skaftadottir, are sincerely thanked for helpful advice which has greatly facilitated all the work. Special thanks are directed to my supervisor E.S. Husebye, NORSAR, and Colin Thomson, Department of Earth Sciences, Cambridge, for valuable advice, encouragement and helpful comments which have greatly contributed to the completion of this thesis.

Acquisition of data was financially supported by 'Visindasjodur Islands' Reykjavik.

Kjeller, 1 December 1981

Kristjan Tryggvason

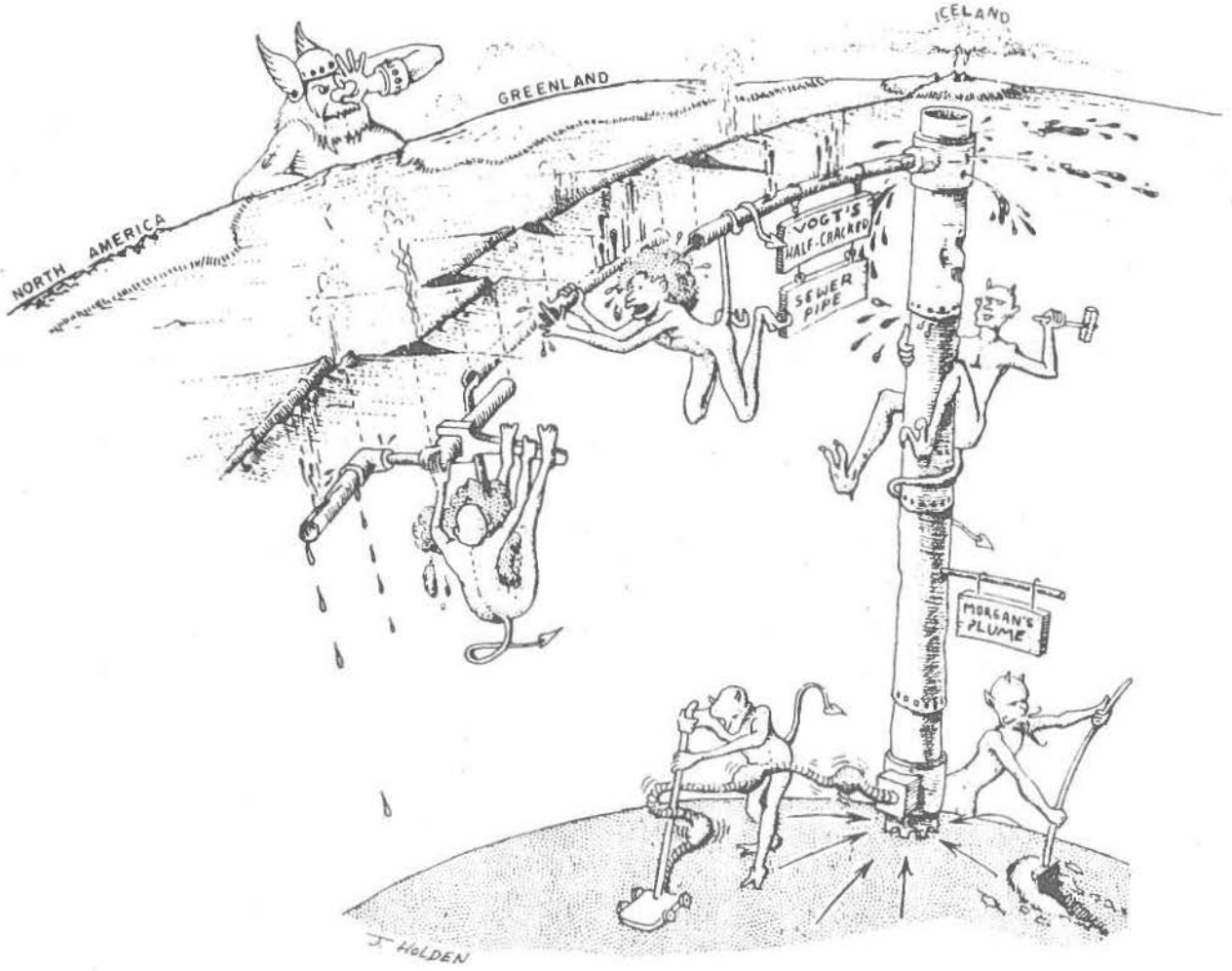

Dr. J. Holden's unorthodox modelling of the Iceland hot spot.

CONTENTS

		Page
	ACKNOWLEDGEMENT	ii
1.	INTRODUCTION	1-1
2.	ACQUISITION AND PROCESSING OF TELESEISMIC DATA	2-1
	2.1 Acquisition of data	2-1
	2.2 Data selection criteria	2-5
	2.3 Teleseismic P-wave residuals	2-6
	2.4 Calculation of the time residuals	2-7
3.	METHODOLOGY	3-1
	3.1 Ray-tracing formulation	3-1
	3.2 The inverse problem	3-8
	3.3 The stochastic inverse	3-11
	3.4 Non-spline representation	3-20
4.	RESULTS	4-1
	4.1 Initial models	4-1
	4.2 On the choice of an adequate smoothing parameter θ^2	4-5
	4.3 Inversion results	4-10
	4.4 On the linearity of the model	4-17
5.	GEOLOGY, GEOPHYSICS AND TECTONIC EVOLUTION OF ICELAND	5-1
	5.1 Stratigraphic classification and main tectonic features of Iceland	5-1
	5.2 Previous geophysical research in Iceland	5-6
	5.3 Mantle convection	5-13
	5.4 The Iceland hot spot	5-15

		Page
6.	INTERPRETATION	6-1
	6.1 On the velocity-density relation and inferred correlation with gravity thereby	6-1
	6.2 Layer 1	6-3
	6.3 Layers 2 and 3	6-4
	6.4 Layer 4	6-5
7.	CONCLUSIONS	7-1
8.	REFERENCES	8-1
	APPENDIX A - The stochastic inverse operator	A-1
	The covariance-resolution relationship	A-2
	APPENDIX B - The S_{300} and N_{300} solutions	B-1

1. INTRODUCTION

Neither the original hypothesis on sea-floor spreading nor its extended version, the plate tectonic hypothesis, both formulated in the early 60's, leave space for a land mass the size of Iceland situated in the middle of the North Atlantic. Wilson (1963) and Morgan (1971, 1972) explained such 'anomalies' (like Hawaii and Iceland) as surface expressions of deep mantle plumes. On the other hand, Ward (1971) proposed that Iceland might have resulted from a change in the stress pattern on a broad fracture zone, allowing large volumes of lava to be erupted while there was little regional spreading. These hypotheses are not contradictory, i.e., Iceland might have resulted from the interaction of 'normal' sea-floor spreading and the action of a deep 'Iceland plume'. In this connection several investigations on Iceland the last two decades indicate an anomalous mantle beneath Iceland.

In the present thesis we use teleseismic data from the Icelandic seismograph network for mapping of the upper mantle inhomogeneities below Iceland. In this process relative P-wave travel time residuals are input parameters to be inverted providing fractional P-wave velocity perturbations as output parameters.

The thesis is arranged as follows: In chapter 2 we present the Icelandic seismograph network, the data base used and a discussion of possible time residual errors. In chapter 3 a rather detailed method description is given. This is a nonblock inversion method due to Smith et al (1979), using cubic splines on the 3-D velocity anomalies. We have also used a modified version of the ACH block method (Aki et al, 1977), allowing bent rays and not neglecting any ray segments. Singularity problems are normally present in both of these methods, and such problems are met by introducing a smoothing (damping) parameter, as discussed in chapters 3 and 4. The derived model, which is a linear approach to the P-velocity structure of the uppermost 375 km, is displayed and discussed in chapter 4. Then the linearity of the model is commented upon and quantitatively demonstrated. A short outline of Iceland's geology, main tectonic features and relevant geophysical and geochemical studies is given in chapter 5. At last (Chapter 6) an attempt is made to relate the seismic anomalies with other geophysical observations like heat flow and gravity. The seismic results are interpreted and discussed within the tectonic regime of Iceland.

2. ACQUISITION AND PROCESSING OF TELESEISMIC DATA

This chapter gives a brief description of the seismological network of Iceland, and the acquisition of relevant P-wave residuals from its seismogram recordings. Potential errors in the data are also commented upon.

2.1 Acquisition of Data

The teleseismic data base used for this thesis was obtained from original event seismograms recorded by stations in the seismological network of Iceland. Names and locations of the 39 stations within this network are listed in Table 2.1. All of them are short period analog instruments mainly designed for microearthquake monitoring. Four of these stations (AKU, REY, SID, EYV) have response characteristics similar to the worldwide network of seismic stations (WWSSN) while the others are most sensitive below 1 second period. The fortieth station, ICE, is a reference point and thus a dummy. Its latitude and longitude are the average of those for the real stations. Figure 2.1 shows the location of the stations and the reference point. The network is inside a square (the model box) limited by the latitudes 61.8 and 67.8 degrees north and longitudes 26.0 and 11.0 degrees west. It covers mainly the riskiest areas in view of volcanic and seismic activity accompanied with population. Because of this the stations are rather unevenly distributed.

A reliable determination of the first P-wave motion on a seismogram requires an accurate comparison of waveforms. This is because the detectability of the stations within the network is very different. Poor detectability results in a tendency to miss the very first cycle(s) of the P-wave train, giving a late arrival. Therefore it is important to simultaneously compare the waveforms from all seismogram readings for each particular event. In some instances the PcP phase has a very clear beginning and therefore appropriate for comparison. As an example of the task of finding the corresponding peaks for different seismograms, Figure 2.2 shows how a clear peak (here PcP) may be used to get rid of possible 'detectability errors'.

The total number of events available was about 160, covering the time interval 1974 to 1980. The acquisition of the data was done by Ragnar Stefansson, Thorunn Skaftadottir and myself at 'Vedurstofa Islands', Reykjavik, Iceland.

TABLE 2.1

Seismograph Stations of Iceland

Station Number	Station Code	Station Name	Station Location Lat (°N)	Long (°W)	Elevation
1	REY	Reykjavik	64.14	21.91	51
2	SID	Sida	63.79	18.06	26
3	VIR	Vik	63.50	18.83	120
4	SKH	Skammadalsholl	63.45	19.10	50
5	SNB	Snæbyli	63.72	18.62	200
6	SEK	Selkot	63.55	19.61	180
7	ARS	Argilsstadir	63.79	20.12	90
8	LAU	Laugarvatn	64.22	20.75	100
9	HVE	Hveravellir	64.87	19.57	640
10	SIM	Sidumuli	64.71	21.38	78
11	SEF	Selfoss	63.94	21.00	20
12	KVI	Kvisker	63.98	16.44	30
13	HEL	Hella	64.01	20.16	100
14	MFE	Midfell	64.40	15.35	60
15	VFE	Vatnsfell	64.20	18.98	620
16	BJA	Bjallavad	64.10	19.16	560
17	SIG	Sigalda	64.18	19.12	580
18	VAL	Valahnukar	64.02	21.84	137
19	IRS	Ir-skali	64.04	21.38	300
20	STH	Storhöfdi	63.40	20.29	120
21	AKU	Akureyri	65.69	18.11	24
22	EYV	Eyvindara	65.28	14.38	25
23	HUS	Husavik	66.02	17.33	180
24	SIF	Siglufjördur	66.16	18.92	120
25	GST	Grimsstadir	65.64	16.13	450
26	SKI	Skinnastadir	66.06	16.44	80
27	HRN	Hraun	66.11	20.12	20
28	SAN	Sandbudir	64.93	18.00	820
29	SVA	Svartarkot	65.34	17.26	405
30	GRI	Grimsey	66.54	18.12	20
31	RHL	Reynihlid	65.65	16.91	340
32	GÆS	Gæsastadir	65.74	16.96	430
33	KRA	Krafla	65.70	16.78	450
34	ABO	Adalbol	65.02	15.58	480
35	RNI	Reykjanes	63.84	22.65	30
36	GUI	Gufuskalar	64.05	22.62	24
37	KLI	-	63.93	22.01	175
38	TOI	Thorbjörn	63.87	22.44	30
39	MVI	Midvik	64.02	22.23	19
40	ICE	Iceland	64.71	18.62	-

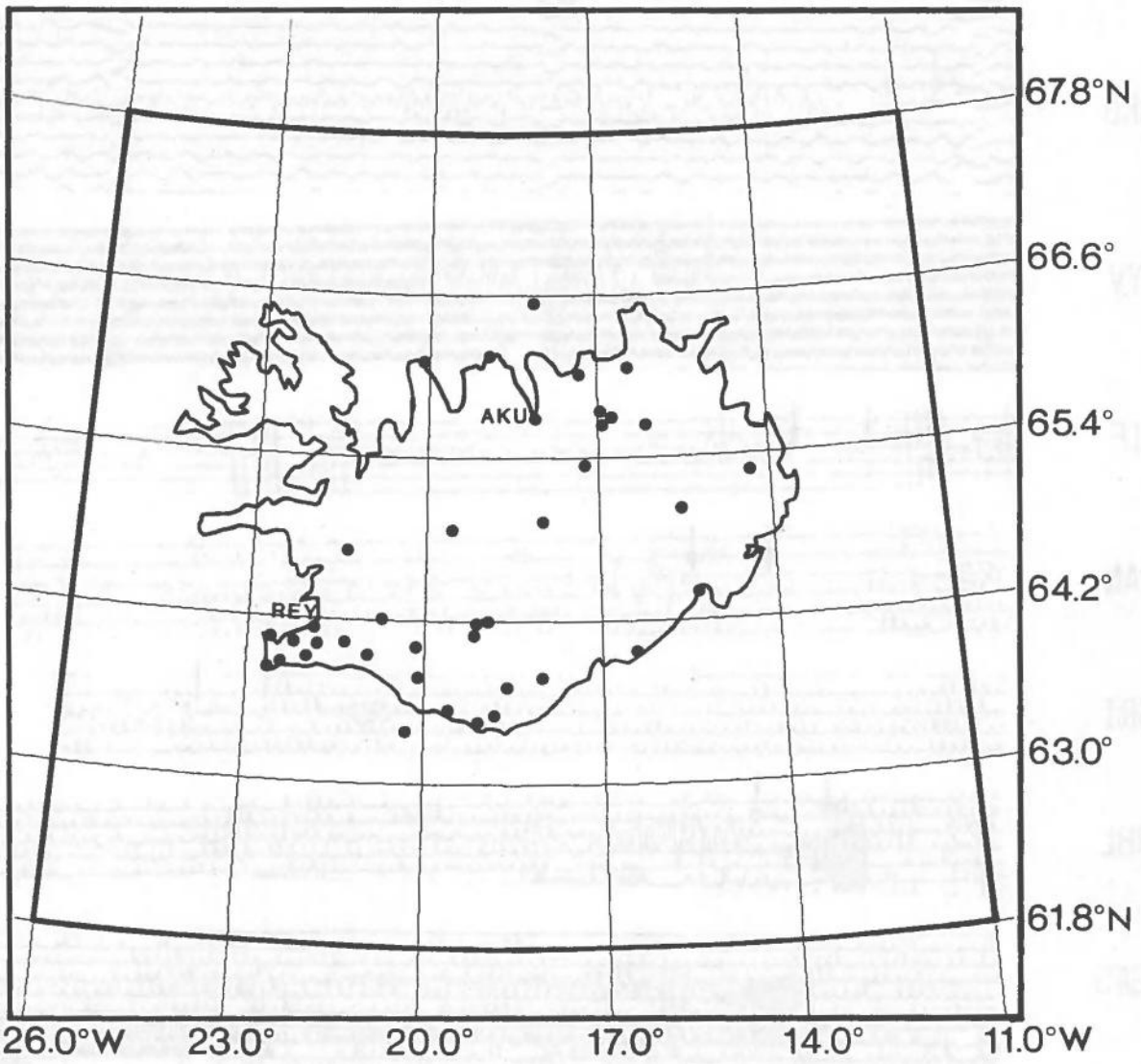

Fig. 2.1 The Icelandic network of 39 seismograph stations used in analysis. The model box is circumscribed with heavy lines. The latitude/longitude grid system intersections correspond to the model knots according to the time residual inversion method described in chapter 3.

7 MAR 1978, ISC: 02.48.39.1, 31.9N 137.6E, 436 KM, M_b 5.9

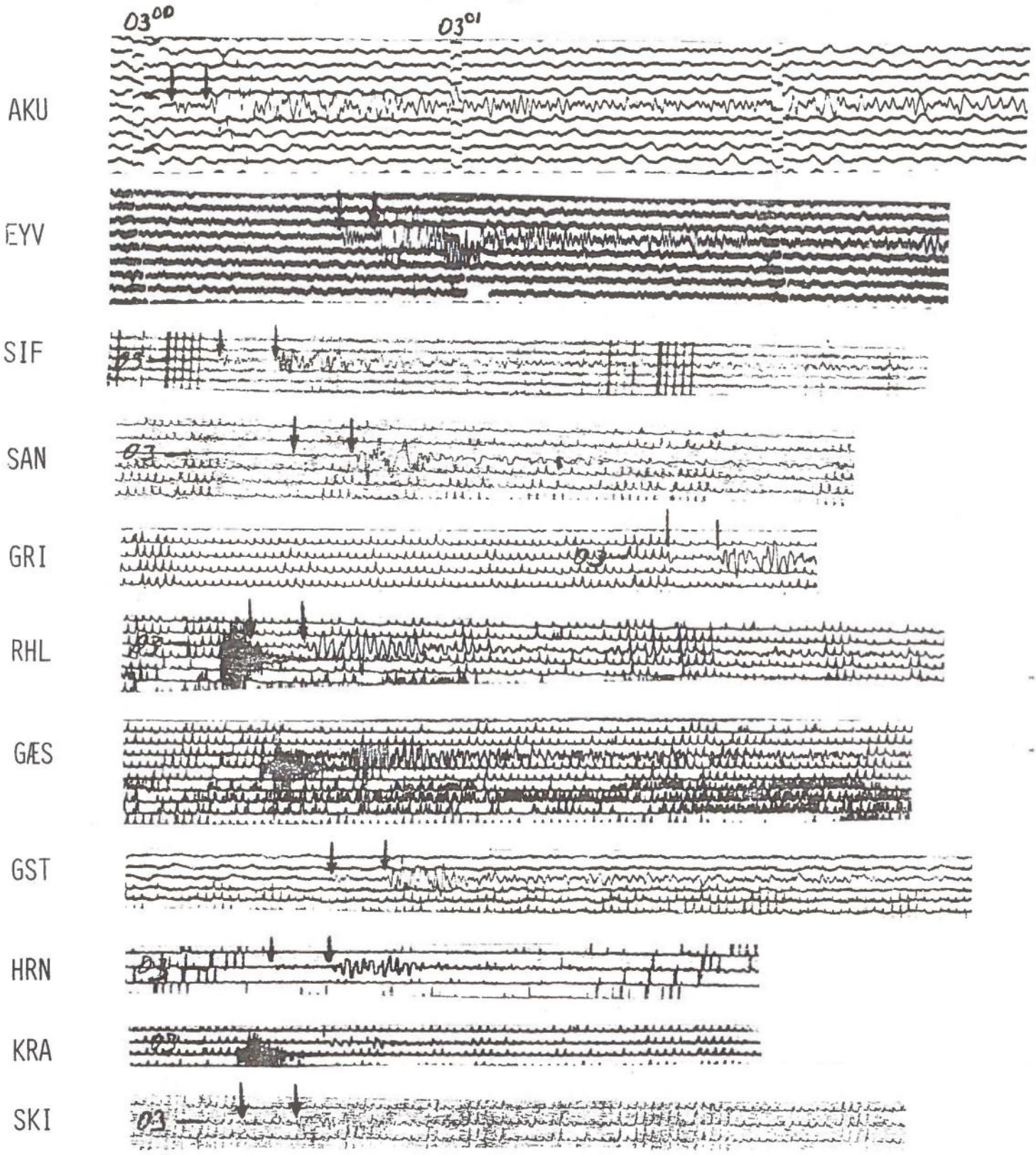

Fig. 2.2 A sample from the data base, 11 recordings from a deep earthquake off the south coast of Japan (recorded acceptably by 17 Icelandic stations), which demonstrates the importance of comparing wave forms. The arrows point out the first P arrival and the PcP phase.

2.2 Data Selection Criteria

Only the primary P-phase was used for analysis. All events were in the distance range 25° to 100°, with body wave magnitude m_b well above 5.0 and were reported by at least 150 of the global network of some 775 stations reporting regularly to the International Seismological Centre (ISC) (e.g., Ringdal et al 1977). After sorting the events into azimuth-delta intervals of 30°x25°, it was clear that many of them had to be omitted in order to avoid a strong sampling bias. Finally, only events recorded at 5 or more Icelandic stations were used. With this selection process, a data base of 61 events ($25° < \Delta < 100°$) from the time period September 1974 to May 1980 was obtained. An epicenter map of these events is presented in Fig. 2.3.

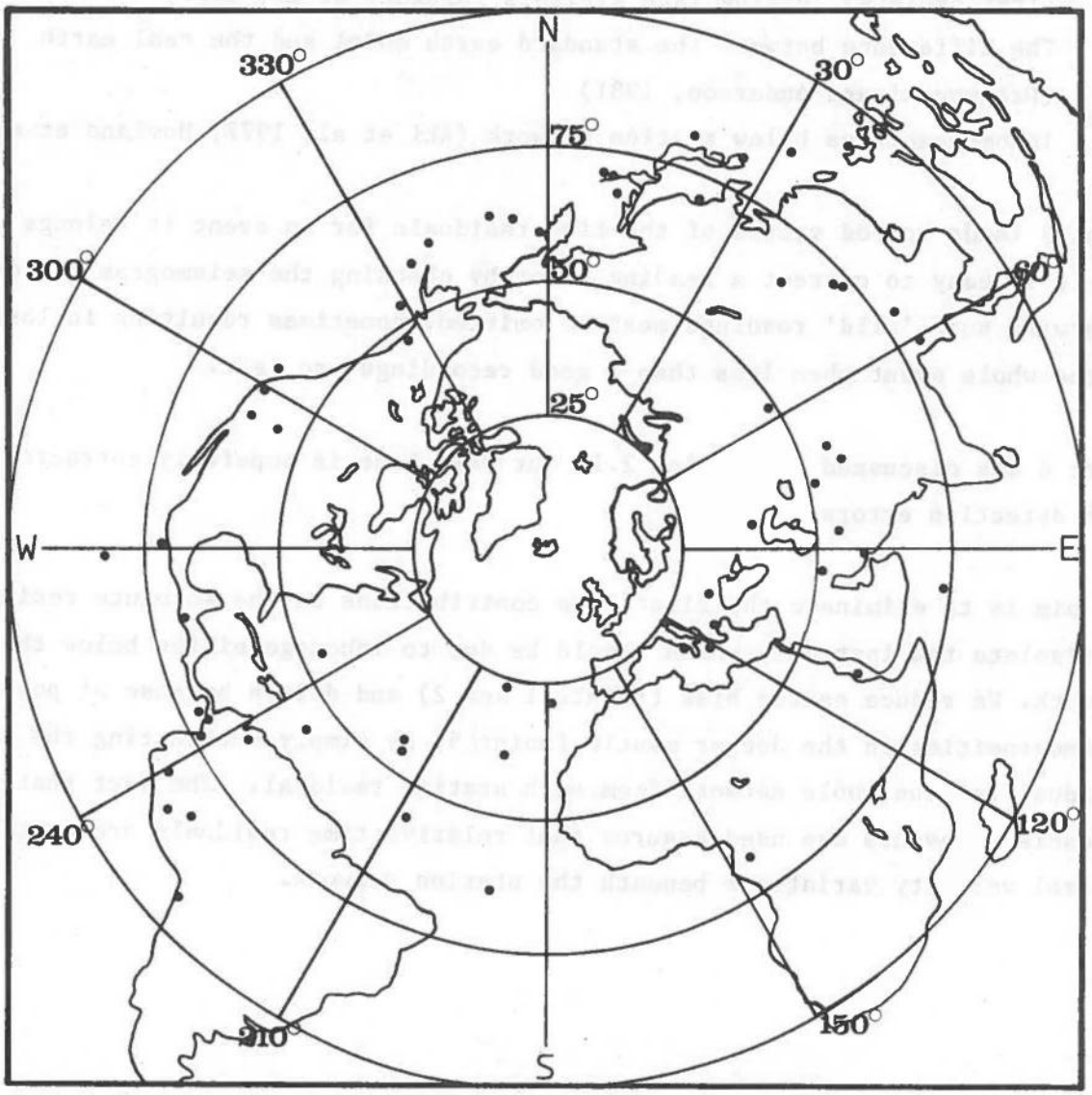

Fig. 2.3 Epicenter map of the 61 events used in analysis.

2.3 Teleseismic P-wave Residuals

An absolute travel time residual for a seismic P-wave is the difference in the observed arrival time at a station and the corresponding theoretical time based on some standard earth model and known or calculated hypocenter and origin time of the event. The contributions to the absolute time residuals are:

(1) Mislocation of the source in space and time

(2) Inhomogeneities below the source, e.g., the slab of a down-going plate (Jordan, 1977)

(3) Instrumental errors (timing problems) and reading errors

(4) Poor detectability of some stations resulting in loss of the very first cycle(s), giving late arrivals (Ringdal et al, 1977)

(5) The difference between the standard earth model and the real earth (Dziewonski and Anderson, 1981)

(6) Inhomogeneities below station network (Aki et al, 1977; Hovland et al, 1981).

Point 3 leads to odd values of the time residuals for an event it belongs to. It is easy to correct a reading error by checking the seismogram copies. Otherwise such 'wild' readings must be omitted, sometimes resulting in loss of the whole event when less than 5 good recordings are left.

Point 4 was discussed in section 2.1. Our data base is hopefully corrected for such detection errors.

Our aim is to eliminate the first five contributions to the absolute residual and isolate the last one, which should be due to inhomogeneities below the network. We reduce source bias (points 1 and 2) and delays because of possible inhomogeneities in the deeper mantle (point 5) by simply subtracting the average residual for the whole network from each station residual. The fact that only teleseismic events are used assures that relative time residuals are mostly due to lateral velocity variations beneath the station network.

2.4 Calculation of the Time Residuals

For calculating travel times the seismological tables of Jeffreys and Bullen (1940) were used, corrected for the earth's ellipticity (Dziewonski & Gilbert, 1976) using the method developed by Jeffreys and Bullen (Bullen 1937). This correction is of the form

$$\delta t = f(\Delta)(h+H)$$

where h and H are the heights of the station and epicenter above the mean sphere and $f(\Delta)$ is a function of the epicentral distance. Also taken into account was the height above sea level of each station within the station network. We introduce the following notations:

AT_{ij} - the arrival time of a wavefront measured at station j for event i

CT_{ij} - calculated travel time of the P-wave between event and station for JB model

OT_i - event origin time

The travel time residual ΔT_{ij} is then

$$\Delta T_{ij} = AT_{ij} - CT_{ij} - OT_i \qquad (1)$$

Then the event average residual is

$$\overline{\Delta T_i} = \frac{1}{n_i} \sum_{j=1}^{n_i} \Delta T_{ij} \qquad (2)$$

where n_i is the number of stations registering event i acceptably.

Subtracting $\overline{\Delta T_i}$ from each residual, we get

$$\delta T_{ij} = \Delta T_{ij} - \overline{\Delta T_i} \qquad (3)$$

the relative time residual. As mentioned before the δT_{ij} is mostly due to lateral variations in the P-wave velocity beneath the station network.

Substituting eqs. (1) and (2) in (3) gives

$$\delta T_{ij} = AT_{ij} - CT_{ij} - \overline{AT}_i + \overline{CT}_i \qquad \text{origin time cancels out}$$

$$= (AT_{ij} - \overline{AT}_i) - (CT_{ij} - \overline{CT}_i)$$

$$= \delta AT_{ij} - \delta CT_{ij} \qquad (4)$$

where

$$\overline{AT}_i = \frac{1}{n_i} \sum_{j=1}^{n_i} AT_{ij} \qquad \text{and} \qquad \overline{CT}_i = \frac{1}{n_i} \sum_{j=1}^{n_i} CT_{ij}$$

From eq. (4) we see that the rel. time residual (δT_{ij}) is the difference of the relative arrival time (δAT_{ij}) and the relative calculated time (δCT_{ij}). Therefore δT_{ij} is only weakly dependent on hypocenter mislocations and independent of error in origin time.

Furthermore, because of the large epicentral distances, near source and deeper mantle inhomogeneities are unlikely to affect δT_{ij}, due to path similarity on the source side.

3. METHODOLOGY

In this chapter we will outline the computational techniques used in inverting relative time residuals of P waves so as to find perturbations to a symmetric standard-earth model. This involves calculating ray paths in the initial model and then finding contributions to travel times made by perturbations in a specified number of velocity parameters. These parameters are slowness values at grid points and intermediate values are obtained by cubic spline interpolation. Once these contributions have been found, a system of simultaneous linear equations may be obtained. An estimate of the true solution is then found by applying the damped least squares method to solve this system of linear equations. This method is due to Smith et al (1979).

3.1 Ray-Tracing Formulation

As the travel time anomalies are caused by velocity variations within an a priori confined volume immediately beneath the station network, we can relate them to departures from some initial earth model throughout this volume. The initial model used for this study represents a mean structure for the Icelandic region. For comparison three other starting models were also used (see Section 4.1).

Fermat's principle states that the variation in the travel time caused by a small change in the ray path is zero to the first order. In other words, the effects of changes in velocity structure on travel times can be found to first order accuracy without knowing the effect on the ray path. This is the basis for linear inversion of travel time data. Therefore, we may obtain a linearized relationship between travel time residuals and velocity variations:

$$\Delta T_{ij} = \int_{A_j}^{B_i} \delta s \, d\ell \qquad (5)$$

where $s=1/v$ is the slowness or reciprocal velocity in $s \cdot km^{-1}$. Because of Fermat's principle we may take the integral over the ray path in the initial earth model, where A_j is the j-th receiver and B_i is the i-th source. It is not meaningful to use iterative ray tracing (and therefore necessarily three dimensional) if the errors introduced by assuming linearity are much less than the errors in the data. We have checked the validity of this basic assumption for linear inversion by 3-D ray tracing through the 3-D medium found from the currently described method - the so-called SGJ method. These subjects will be qualitatively and quantitatively presented in section 4.4. The 1-D ray tracing method applied is the so-called 'shooting' method. It was modified to deal only with the anomalous region immediately beneath the station network:

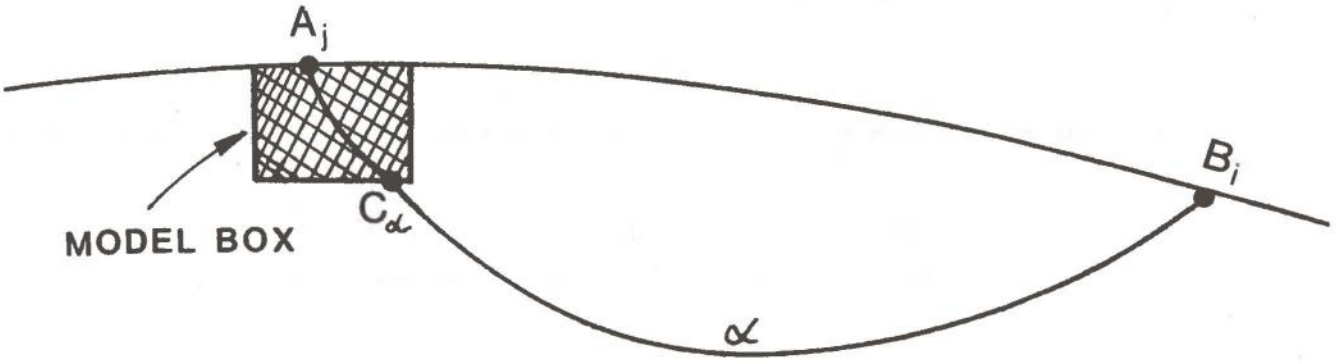

Fig. 3.1 For each ray path α the spherically symmetric initial model is traced from receiver A_j until crossing some edge of the box. C_α is the point of intersection.

Now

$$\delta T_\alpha = \int_{A_j}^{C_\alpha} \delta s \cdot d\ell \qquad (6)$$

Spherically Symmetric Earth

The starting model is spherically symmetric, i.e., the velocity is only a function of depth. A complete treatment is given by Bullen (1963, Chap. 7).

The input data for this ray tracing calculation are source and receiver co-ordinates, ray parameter (p_o), azimuth (z_o) from each event to the reference point (ICE - see Fig. 2.1). On an average there were about 12 recordings for each of the 61 events, which gave a total of 714 recordings. p and z for these 714 source-receiver pairs are estimated by the linear formulae:

$$p = p_o + \frac{\partial p}{\partial \Delta}\,\partial\Delta$$

where $\partial\Delta = - D \cos(z_o-\theta)$

$$z = z_o + \frac{D\sin(z_o-\theta)}{\Delta}$$

where Δ is the distance from event to reference point ICE and D,θ are the relative distance and azimuth from ICE to the receiver under consideration. In the program z is the azimuth from receiver to event. Knowing p and z the ray paths are traced through one of the spherically symmetric starting models outlined in section 4.1.

The 3-D velocity anomaly was represented by a smooth cubic spline interpolation between velocity values on a three-dimensional grid. This representation was developed by Smith et al (1979) as being suitable for three-dimensional ray tracing. The method is described here in one dimension and for equally spaced points, which then easily can be generalized to three dimensions. The development closely follows that of Schultz (1973).

The Hermite interpolate for equal spacing, Δx, is defined as:

$$f(x) = \sum_{i=1}^{N} f_i\, H\left(\frac{x-x_i}{\Delta x}\right) + f_i' H^1\left(\frac{x-x_i}{\Delta x}\right) \qquad (7)$$

where $f_i = f(x_i) = g(x_i)$ and $f_i' = g_i'$ are known and g(x) is the function under consideration and f(x) is the interpolate.

$$H(x) = \begin{cases} (1+x)^2(1-2x) & \\ (1-x)^2(1+2x) & \text{for} \\ 0 & \end{cases} \quad \begin{matrix} -1 \leq x \leq 0 \\ 0 \leq x \leq 1 \\ \text{otherwise} \end{matrix}$$

$$H^1(x) = \begin{cases} x(1+x)^2 & \\ x(1-x)^2 & \text{for} \\ 0 & \end{cases} \quad \begin{matrix} -1 \leq x \leq 0 \\ 0 \leq x \leq 1 \\ \text{otherwise} \end{matrix}$$

$$\Delta x = x_{i+1} - x_i \qquad - \qquad \text{equal spacing}$$

The cubic functions, H(x) and $H^1(x)$, have the property that they and their derivatives vanish at all knot points except the i-th, where H(x) is unity and its derivative zero, and $H^1(x)$ is zero and its derivative is unity.

Spline representation

This cubic spline interpolation procedure is an improvement over the piecewise cubic Hermite interpolation procedure in the sense that it yields a smoother interpolate. The Hermite interpolate is only a first order continuous differentiable function and requires both f_i and f_i' to be known. However, if only f_i is known, we may still obtain a unique interpolation by requiring that f''(x) is continuous.

If we specify that the interpolation function, f(x), has continuous second derivatives everywhere, it requires at the knot points

$$f_{i-1}'+4f_i'+f_{i+1}' = \frac{3}{\Delta x}(f_{i+1}-f_{i-1}) \qquad (8)$$

i.e., a set of N-2 linear equations relating f_i' to f_i. Two more conditions are required to determine f'. With appropriate consideration of the end points, for instance, linear extrapolation of the derivatives:

$$f_1' = f_2' - (f_3' - f_2') = 2f_2' - f_3'$$

$$f_N' = f_{N-1}' + (f_{N-1}' - f_{N-2}') = 2f_{N-1}' - f_{N-2}$$

we can write:

$$\begin{bmatrix} 1 & -2 & 1 & . & . & 1 \\ 1 & 4 & 1 & 0 & \cdots & 0 \\ 0 & 1 & 4 & 1 & \cdots & . \\ . & . & . & . & & . \\ . & . & . & . & & . \\ . & . & . & . & & . \\ 0 & . & . & 1 & 4 & 1 \\ 0 & . & . & 1 & -2 & 1 \end{bmatrix} \begin{bmatrix} f_1' \\ . \\ . \\ . \\ . \\ . \\ f_N' \end{bmatrix} = \frac{3}{\Delta x} \begin{bmatrix} 0 & . & . & . & . & 0 \\ -1 & 0 & 1 & 0 & \cdots & 0 \\ 0 & -1 & 0 & 1 & \cdots & . \\ . & . & . & . & & . \\ . & . & . & . & & . \\ 0 & . & 0 & -1 & 0 & 1 \\ 0 & . & . & . & . & . \end{bmatrix} \begin{bmatrix} f_1 \\ . \\ . \\ . \\ . \\ . \\ f_N \end{bmatrix}$$

i.e., $B \cdot f' = \frac{3}{\Delta x} \cdot A \cdot f$.

Therefore we can write:

$$f' = G\, f \qquad (9)$$

where $G = \frac{3}{\Delta x} B^{-1} A$, G is an NxN matrix.

Now

$$f(x) = \sum_{i=1}^{N} \left(f_i H\left(\frac{x-x_i}{\Delta x}\right) + \sum_{j=1}^{N} G_{ij} f_j \, H^1\left(\frac{x-x_i}{\Delta x}\right) \right) \qquad (10)$$

Defining the cardinal splines as:

$$c_i(x) = H\left(\frac{x-x_i}{\Delta x}\right) + \sum_{j=1}^{N} G_{ji} H^1\left(\frac{x-x_j}{\Delta x}\right)$$

then finally we can write

$$f(x) = \sum_{i=1}^{N} f_i c_i(x) \qquad (11)$$

This cubic spline representation is not local as f(x) depends on all the quantities f_i, $1 \leq i \leq N$.

Modified Splines

The non-local representation (eq. (10)) was rated too expensive to compute. If we demand that the interpolate value at x, $x_{i-1} \leq x \leq x_i$, depends only on the values at x_{i-2}, x_{i-1}, x_i, x_{i+1}, it is equivalent to assuming that $c_i(x)$ is zero outside this range. This speeds up evaluation of f(x) because only 4 terms need to be summed. In constructing the matrix G, we assume the condition (8) applies at x_i and x_{i-1}, so the second derivatives of the respective $c_i(x)$ are conditions. Taking linear extrapolation of the derivatives:

$$f'_{i-2} = f'_{i-1} - (f'_i - f'_{i-1}) = 2f'_{i-1} - f'_i$$

$$f'_{i+1} = f'_i + (f'_i - f'_{i-1}) = 2f'_i - f'_{i-1}$$

we have got 4 linear independent equations required to determine the $\{f_i\}$. Now the modified system of linear equations will be:

$$\underset{B}{\begin{bmatrix} 1 & -2 & 1 & 0 \\ 1 & 4 & 1 & 0 \\ 0 & 1 & 4 & 1 \\ 0 & 1 & -2 & 1 \end{bmatrix}} \quad \underset{f'}{\begin{bmatrix} f'_{i-2} \\ f'_{i-1} \\ f'_i \\ f'_{i+1} \end{bmatrix}} = \frac{3}{\Delta x} \underset{A}{\begin{bmatrix} 0 & 0 & 0 & 0 \\ -1 & 0 & 1 & 0 \\ 0 & -1 & 0 & 1 \\ 0 & 0 & 0 & 0 \end{bmatrix}} \quad \underset{f}{\begin{bmatrix} f_{i-2} \\ f_{i-1} \\ f_i \\ f_{i+1} \end{bmatrix}}$$

Recalling eq. (9), we can construct the 4x4 matrix G

$$G = \frac{1}{2\Delta x} \begin{bmatrix} -2 & 1 & 2 & -1 \\ -1 & 0 & 1 & 0 \\ 0 & -1 & 0 & 1 \\ 1 & -2 & -1 & 2 \end{bmatrix}$$

The spline interpolate function can now be expressed as:

$$f(x) = \sum_i f_i c_i(x) \tag{12}$$

where

$$c_i(x) = H\left(\frac{x-x_i}{\Delta x}\right) + \sum_{j=1}^{4} G_{ji} H^1\left(\frac{x-x_j}{\Delta x}\right)$$

The $c_i(x)$ need only be calculated once and stored. In practice they are computed for 301 values in the range (0, 1). The 'cardinal splines' $\{c_i(x)\}$ are then looked up in this table.

Generalizing to three dimensions we get:

$$s(x,y,z) = \sum_{i,j,k} s_{ijk}\, c_i(x) c_j(y) c_k(z) \tag{13}$$

by defining $c_j(y)$ and $c_k(z)$ in the same way as $c_i(x)$.

Rewriting this in favour of more convenient notations:

$$s = \sum_k w_k s_k \tag{13}$$

Invoking the familiar travel time equation $T = \int s d\ell$. Partial differentiation of the travel time with respect to slowness gives then:

$$\frac{\partial T}{\partial s_k} = \int w_k d\ell \tag{14}$$

where Fermat's principle has been used.

The integral on the right hand side is calculated by the trapezium rule from known points on the ray path. These partial derivatives are the coefficients in the system of simultaneous linear equations to be solved.

3.2 The Inverse Problem

$$\Delta T_\alpha = \sum_{\ell=1}^{N} A_{\alpha\ell}\, \delta s_\ell + \varepsilon \tag{15}$$

$N = n_x \cdot n_y \cdot n_z$, where n_x, n_y, n_z are the number of grid points in the x,y,z directions, respectively, and δs is a slowness perturbation.

$$\ell = i + (j-1)n_x + (k-1)n_x n_y$$

where i,j,k are whole numbers running from 1 to n_x, n_y, n_z, respectively.

Positive directions of x,y,z axis are:

x (Up) y (South) z (East)

Eq. (15) is in the form of the standard linear inverse problem for δs_ℓ. We solve this equation by the damped least squares method following Aki et al (1977). In order to reduce errors we subtract the mean from the residuals and consequently the same must be done to the right hand side of eq. (15). Therefore we write the linear inverse problem for δs_ℓ in terms of relative residuals (δT_α):

$$\delta T_\alpha = \Delta T_\alpha - \overline{\Delta T_\alpha} = \sum_{\ell=1}^{N} (A_{\alpha\ell} - \bar{A}_{\alpha\ell})\, \delta s_\ell + \varepsilon - \bar{\varepsilon} \qquad (16)$$

where

$$\bar{A}_{\alpha\ell} = \frac{1}{n_i} \sum_{\alpha=\alpha_1}^{\alpha_i} A_{\alpha\ell}$$

n_i is the number of stations registering event i acceptably.

In effect, for an incident plane wavefront any change in mean P wave velocity from that in the starting model is precluded by this operation (eq. (16)). However in the method used slightly curved rays are allowed, so this is not exactly true.

In solving the linear inverse problem the methods most commonly used are either generalized inverse (Lanczos, 1961) or stochastic inverse (Franklin, 1970). We preferred the latter one. The main reason lies in the spectrum of the normal equation matrix. The range of non-zero eigenvalues is very large, greater than 10^7, and reflects the model parameterization. The fall off in size of the eigenvalues is gradual, and there is no obvious place at which to truncate the spectrum to form a generalized inverse (Marquardt, 1970; Wiggins, 1972; Aki & Richards, 1980).

Writing eq. (16) in matrix form:

$$d = A\, s + e \qquad (17)$$

where d is a vector of relative time residuals (δT_α), A is a matrix of partial derivatives defined by eq. (14) belonging to different knots, s is a vector of unknown slowness perturbations at individual knots, and e is a vector of random errors in data.

The stochastic inverse solution (Franklin, 1970) is given by

$$\hat{s} = (A^t A + \theta^2 I)^{-1} A^t d \qquad (18)$$

where the circumflex indicates the damped least-squares estimate of the vector s. The scalar θ^2 is the smoothing (damping) parameter and is expressed as a fraction of the largest element on the diagonal of the normal equations matrix A^tA.

This solution may be obtained by minimizing the quantity:

$$E[(\hat{s}-s)(\hat{s}-s)^t]$$

A useful quantity is the reduction in variance which may be written as:

$$\hat{s}^t(A^td) + \theta^2\ \hat{s}^t\hat{s}$$

It is a measure of the model's success or ability to fit the data.

The resolution matrix, R, is a measure of the resolving power of each particular parameter estimate and is expressed as:

$$R = (A^tA+\theta^2I)^{-1}A^tA \qquad (19)$$

(Wiggins, 1972; Jackson, 1972). In practice it is sufficient to check only the diagonal elements of R, which for well-resolved model parameters will be close to unity. The accuracy with which the model parameters are determined is measured by the covariance matrix of the model estimates:

$$C_\delta = (A^tA+\theta^2I)^{-1}R\sigma_d^2 \qquad (20)$$

where σ_d^2 is the variance of the relative time residuals which are presumed uncorrelated and all with equal variance. Again it is sufficient to display only the diagonal of C_δ which gives the variance of individual parameter estimates. We should like to remark here that maps of model vector $\underline{s}$ (estimated upper mantle slowness perturbations, ch. 4) always should be interpreted in conjunction with the corresponding maps or tabulation of resolution and standard error estimates.

3.3 The Stochastic Inverse

Lanczos's novel solution of the inversion problem, the generalized inverse, requires comprehensive eigenvector analysis. The stochastic inverse, on the other hand, requires only matrix multiplication (plus a constant added to the diagonal) and inversion, thus providing a very efficient inversion technique. The normal equations matrix (A^tA) normally has singularities which are met by introducing a smoothing parameter θ^2 added to the diagonal of A^tA before inversion. In effect, this operation suppresses all eigenvalues lower than θ^2. The optimal solution by the stochastic inverse method gives a good approximation to the generalized inverse. This is when θ^2 equals the noise to solution variance ratio σ_e^2/σ_x^2.

We introduce the following notations:

A - a known nxm matrix - matrix of condition

x - a vector of length m, with unknowns and expected to have zero mean and correlation equal to zero

e - a vector of length n, with random data errors and expected to have zero mean and correlation equal to zero

d - a vector of length n, with data.

$$Ax + e = d \qquad - \qquad \text{eq. of condition} \tag{21}$$

Solving this system of linear equations (21), we get an estimate, $\hat{x}$, of the unknown vector x. We seek a matrix operator H such that

$$\hat{x} = Hd \tag{22}$$

is a good approximation of the correct vector x. Combining (21) and (22) gives:

$$\hat{x} = HAx + He = Rx + He$$

Therefore R must not have large deviations from the identity matrix I, and the random error e must not be unacceptably large; otherwise $\hat{x}$ cannot be considered as a solution of the system. The estimation error (total error) is:

$$\hat{x}-x = (HA-I)x + He \tag{23}$$

$\hat{x}$ is a good approximation of x if $\hat{x}-x$ is small and therefore both $(HA-I)x$ and He must be small.

In the stochastic inversion one looks on x as a vector of random variables and $\hat{x}$ as a vector of extimates to these variables. Then the correlation matrix of total errors is:

$$C = E[(\hat{x}-x)(\hat{x}-x)^t]$$

$$= E[((HA-I)x+He)((HA-I)x+He)^t]$$

$$= (HA-I)E[xx^t](HA-I)^t+(HA-I)E[xe^tH^t]+E[Hex^t](HA-I)^t+HE[ee^t]H^t$$

$$= (HA-I)\, C_{xx}(HA-I)^t+HC_{ee}H^t$$

because $E[Hex^t] = E[xe^tH^t] = 0$, i.e., the random errors in the data and the solution are uncorrelated. C_{xx} is the covariance matrix of the true solution vector and C_{ee} the covariance matrix of random errors.

The correlation matrix of total errors

$$C = (HA-I)\, C_{xx}(HA-I)^t + HC_{ee}H^t \tag{24}$$

is a sum of two components; the one is due to imperfect resolution and the other due to random errors in data. Thus for a perfect resolution, i.e., when $R = HA$ equals the identity matrix I, the correlation matrix reduces to:

$$C = HC_{ee}H^t \tag{25}$$

In that case the estimation or total errors are solely due to random errors in data.

The task is now to find a matrix operator H which minimizes:

$$E[(H_{ij}d_j - x_i)^2]$$

where E is expectance. The minimization of this with respect to H can be made by differentiating with respect to $H_{i\ell}$ and equating to zero:

$$E[2(H_{ij}d_j - x_i)d_\ell] = 0$$

$$H_{ij}E[d_j d_\ell] - E[x_i d_\ell] = 0$$

$$HC_{dd} - C_{xd} = 0$$

giving

$$H = C_{xd}C_{dd}^{-1} \tag{26}$$

On the other hand, if the vectors x and e are uncorrelated ($C_{xe} = 0$) we obtain

$$C_{xd} = E[x(Ax+e)^t] = E[xx^tA^t + xe^t] = C_{xx}A^t \tag{27}$$

and

$$C_{dd} = E[(Ax+e)(Ax+e)^t] = E[Axx^tA^t + Axe^t + ex^tA^t + ee^t] = AC_{xx}A^t + C_{ee} \tag{28}$$

Substituting eqs. (27) and (28) into eq. (26), we obtain

$$H = C_{xx}A^t(AC_{xx}A^t + C_{ee})^{-1} \tag{29}$$

The operator H can also be written as (see Appendix A.1)

$$H = C_{xx}(A^tC_{xx}A + C_{ee})^{-1} \tag{30}$$

Hence, the estimated solution $\hat{x}$ will be

$$\hat{x} = C_{xx}(A^tC_{xx}A + C_{ee})^{-1}d$$

and the resolution matrix:

$$R = HA = C_{xx}(A^t C_{xx} A + C_{ee})^{-1} A$$

Finally, the correlation matrix of total errors:

$$C = (A^t C_{ee}^{-1} A + C_{xx}^{-1})^{-1}$$

is found by combining eqs. (24) and (30).

A special case of the stochastic inverse, in which

$C_{ee} = \sigma_d^2 I$ where σ_d^2 is the average variance of relative time residuals and $\sigma_d^2 = \sigma_e^2$ because the vector e is expected to have zero mean

$C_{xx} = \sigma_x^2$ where σ_x^2 is the expected (unknown) variance of the true solution

gives a good approximation to the generalized inverse.

Accordingly

$$H = (A^t A + \theta^2 I)^{-1} A^t \tag{31}$$

$$\hat{x} = (A^t A + \theta^2 I)^{-1} A^t d \tag{32}$$

$$R = (A^t A + \theta^2 I)^{-1} A^t A \tag{33}$$

$$C = \sigma_d^2 (A^t A + \theta^2 I)^{-1} \tag{34}$$

where $\theta^2 = \dfrac{\sigma_d^2}{\sigma_x^2}$, the ratio of data variance to model variance, is called the smoothing (damping) parameter.

From eq. (34) it follows immediately that C is a symmetric matrix as $C = C^t$. Hence R is symmetric too, as it is a multiple of two symmetric matrices, $(A^t A + \theta^2 I)^{-1}$ and $A^t A$.

The errors $\hat{\delta x}$ in the solution estimates due to random errors e in data

$$\hat{\delta x} = (A^tA+\theta^2I)^{-1}A^te$$

can be described by their covariance matrix

$$C_{\delta x\delta x} = E\left[\hat{\delta x}\hat{\delta x}^t\right] =$$

$$= E\left[(A^tA+\theta^2I)^{-1}A^tee^tA(A^tA+\theta^2I)^{-1}\right]$$

For convenience we reduce the subscripts of the covariance matrix, so $C_{\delta x\delta x}$ becomes:

$$C_\delta = (A^tA+\theta^2I)^{-1}A^tE[ee^t]A(A^tA+\theta^2I)^{-1}$$

$$C_\delta = HC_{ee}H^t = \sigma_d^2HH^t$$

This is exactly the second term in eq. (24) discussed earlier. It is clear from this last equation that the covariance matrix C_δ due to errors in data may be expressed in terms of the resolutin matrix. For uncorrelated data errors the equality

$$C_\delta = \frac{\sigma_d^2}{\theta^2}(R-R^2) \qquad (35)$$

is valid. This simple relationship between covariance and resolution is derived in Appendix A.2

Variance and Standard Errors

The diagonal elements in C, which are the variance of the slowness perturbation estimates, can be written as

$$C_{ii} = \frac{\sigma_d^2}{\theta^2}(R_{ii}-(R^2)_{ii})$$

where $(R^2)_{ii} = \sum_j R_{ij}R_{ji} = \sum_j R_{ij}^2$ because R is symmetric, i.e.,

$$C_{ii} = \frac{\sigma_d^2}{\theta^2}\left(R_{ii} - \sum_j R_{ij}^2\right)$$

But $\sum_j R_{ij}^2 \geq R_{ii}^2$ therefore

$$0 < C_{ii} \leq \frac{\sigma_d^2}{\theta^2}\left(R_{ii}-R_{ii}^2\right) \tag{36}$$

In other words the diagonal elements in C_δ are bound by an ellipse formed of the diagonal elements in the resolution matrix. This relation is due to Ellsworth (1977) and affords a criterion for choosing θ^2 on the basis of solution variance as will be discussed in section 4.2 (see also Hovland, 1980; Aki & Richards, 1980). If we now define $\Delta\hat{m}$ as a vector containing the standard errors, we get

$$\Delta\hat{m}_i \leq \frac{\sigma_d}{\theta}\left(R_{ii}-R_{ii}^2\right)^{\frac{1}{2}} \tag{37}$$

The function $F(R_{ii}) = (R_{ii}-R_{ii}^2)^{\frac{1}{2}}$ has its maximum value for the derivative $\frac{1}{2}(R_{ii}-R_{ii}^2)^{-\frac{1}{2}}(1-2R_{ii}) = 0$, i.e., $F(R_{ii})_{max} = \frac{1}{2}$ for $R_{ii} = \frac{1}{2}$.

Therefore

$$\Delta\hat{m}_i \leq \frac{\sigma_d}{2\theta} \tag{38}$$

This means that the standard errors are absolutely bounded from above by $\frac{\sigma_d}{2\theta}$ increasing when θ decreases, so $\lim_{\theta\to 0} \frac{\sigma_d}{2\theta} = \infty$. For $\theta > 0$ the points on the resolution-standard error diagram are bound by the ellipse in (33).

Variance Improvement

We have used stochastic inverse to get an estimate

$$\hat{x} = (A^tA+\theta^2I)^{-1}A^td$$

of the solution vector x satisfying the linear system Ax+e = d. A measure of how large fraction of the residuals can be answered or explained by the model $\hat{x}$ is achieved by calculating the variance improvement:

$$\frac{\langle|d|^2\rangle-\langle|e|^2\rangle}{\langle|d|^2\rangle} \qquad \text{where } e = d - A\hat{x} \tag{39}$$

$\langle|d|^2\rangle$ is an estimate of the square of the Euclidian length of d.
$\langle|e|^2\rangle$ is an estimate of the square of the Euclidian length of e.

$e^te = d^td - 2\hat{x}^tA^td+\hat{x}^tA^tA\hat{x}$ and by using $A^tA\hat{x}=A^td-\theta^2\hat{x}$ we get
$e^te = d^td - \hat{x}^tA^td-\theta^2\hat{x}^t\hat{x}$ which can be written as

$$|e|^2 = |d|^2-\hat{x}^tA^td-\theta^2|\hat{x}|^2$$

or

$$\langle|e|^2\rangle = \langle|d|^2\rangle - \langle\hat{x}^tA^td\rangle-\theta^2\langle|\hat{x}|^2\rangle$$

The variance improvement (eq. (35)) will then be

$$\frac{\langle\hat{x}^tA^td\rangle+\theta^2\langle|\hat{x}|^2\rangle}{\langle|d|^2\rangle} \tag{40}$$

A^td is the right-hand side, rhs, in the normal equations for the model x. $\langle\hat{x}^tA^td\rangle$ is an estimate of the model times rhs, and $\theta^2\langle|\hat{x}|^2\rangle$ is the smoothing constant, added to the diagonal in the normal matrix A^tA, times the square of the model estimates. The numerator

$$\langle \hat{x}^t A^t d \rangle + \theta^2 \langle |\hat{x}|^2 \rangle .$$

is the reduction in variance. In the inversion program this parameter is called redr.

The rms of the data is:

$$\sigma_d = \sqrt{1/n}\, \langle |d|^2 \rangle \qquad \text{i.e.,} \quad \langle |d|^2 \rangle = n\sigma_d^2$$

where n is the number of data points (ray paths). Henceforth,

$$\text{var. improvement} = \frac{\text{redr.}}{n\sigma^2_d} . \tag{41}$$

Modified Solution

Our task is to solve the linear equation Ax+e = d which is over-determined. We do that by minimizing the expression:

$$(d-A\hat{x})^t(d-A\hat{x})+\theta^2 \hat{x}^t \hat{x}$$

which gives us the damped least-squares estimate of the x vector as:

$$\hat{x} = (A^tA+\theta^2 I)^{-1} A^t d \tag{42}$$

The $\hat{x}$ vector is an estimate of the slowness perturbations Δs of the model. We are searching for the relative velocity anomalies, $\frac{\Delta v}{v}$. But as $\frac{\Delta v}{v} = -\frac{\Delta s}{s}$ we get the desired solution by dividing by the average slowness for each layer and changing signs. More preferable though is to solve directly for the relative slowness $\frac{\Delta s}{s}$.

$$\Delta s_\alpha = \sigma_\alpha \frac{\Delta s_\alpha}{s_\alpha} \qquad \text{or} \quad x_\alpha = n_\alpha y_\alpha \quad (\alpha = 1,m)$$

The original equation of condition

$$a_{i\alpha}x_\alpha + e_i = d_i \qquad (\alpha = 1,m;\ i=1,n)$$

can now be written as

$$a_{i\alpha}n_\alpha y_\alpha + e_i = d_i \qquad \text{or in vector form}$$

$$By + e = d$$

The damped least-squares estimate of the solution vector y is then according to eq. (42)

$$\hat{y} = (B^tB+\theta^2I)^{-1}B^td \tag{43}$$

In terms of the original A matrix and by using the same subscripts as above we have

$$\hat{y}_\alpha = (a_{i\beta}n_\beta a_{i\alpha}n_\alpha+\theta^2\delta_{\alpha\beta})^{-1}a_{i\beta}n_\beta d_i \quad (\beta=1,m)$$

where $\hat{y}_\alpha$ is the estimated relative slowness for knot-point α in the model and n_α, n_β are slowness values from the starting model.

When solving for $\frac{\Delta s}{s}$ instead of Δs alters both the normal equation matrix A^tA and the right-hand side vector A^td to B^tB and B^td respectively. The effect of these changes is a better smoothing with depth. The anomalies in the upper layers are enhanced while those in the lower layers are suppressed. The same applies for the resolution.

3.4 Non-spline representation

The ACH block method (Aki, Christoffersson and Husebye, 1977) is an example of what here is named non-spline representation. The method assumes a constant velocity for each layer and therefore linear ray paths. Furthermore, within each layer the ray segment could be associated with one block only. Naturally the block size is then slightly larger than formally defined. In practice this means, however, that the estimated velocity perturbation for a block is a block-average estimate.

In this study a more flexible ray tracing technique is used allowing bent rays and properly accounting for those cases where the rays sample more than one block within a layer. Henceforth, this non-spline version is called a modified version of the ACH method.

4. RESULTS

The solution by the stochastic inverse method depends on the choice of initial model and the smoothing parameter θ^2, These subjects will be discussed in the first two sections of this chapter, then presentation of major results will follow.

4.1 Initial Models

Selecting the parameters of the initial model we have (a) the velocity throughout the model, (b) the model's block configuration, i.e., number and thickness of the horizontal layers and the number and dimension of the blocks in each layer (or their images for the cubic spline represented non-block model, S_{300}).

(a) Velocity models for a spherically symmetric earth

We examined to what extent a proper choice of a velocity model may improve the solution in view of reduced variance in residuals. Four different velocity models (labeled C,K,T,S) were tested, all represented by smooth continuous functions as illustrated in Fig. 4.1. The layered model D (also shown in Fig. 4.1) is the parameterized earth model PEM-O for oceanic structure while the model C is based on PEM-C for continental structure (Dziewonski et al, 1975). The composite model K is constructed from refraction studies down to ~ 60 km (Palmason, 1971; Flovenz, 1980; and Gebrande et al, 1980) and follows Dziewonski's PEM-O model thereafter. Additional information from surface wave studies (R. Stefansson, 1980, unpublished, see section 5.2) on an upper mantle low velocity zone with top at ~ 60 km resulted in the model T. Figure 4.2 illustrates how the model S is constructed as an average structure for the Iceland region down to ca 60 km. From ca 60-110 km depth above mentioned low velocity zone is incorporated. Thereafter it follows Dziewonski's oceanic model. All the four starting models gave about the same variance improvement which demonstrates that the inversion method is reasonably robust and does not demand a detailed knowledge about the upper mantle velocity. For comparison a straight line between v(0)=2 and v(300)=8 gave about 6% lower variance improvement than the above-mentioned models. In our computations the model S was used as the initial velocity model.

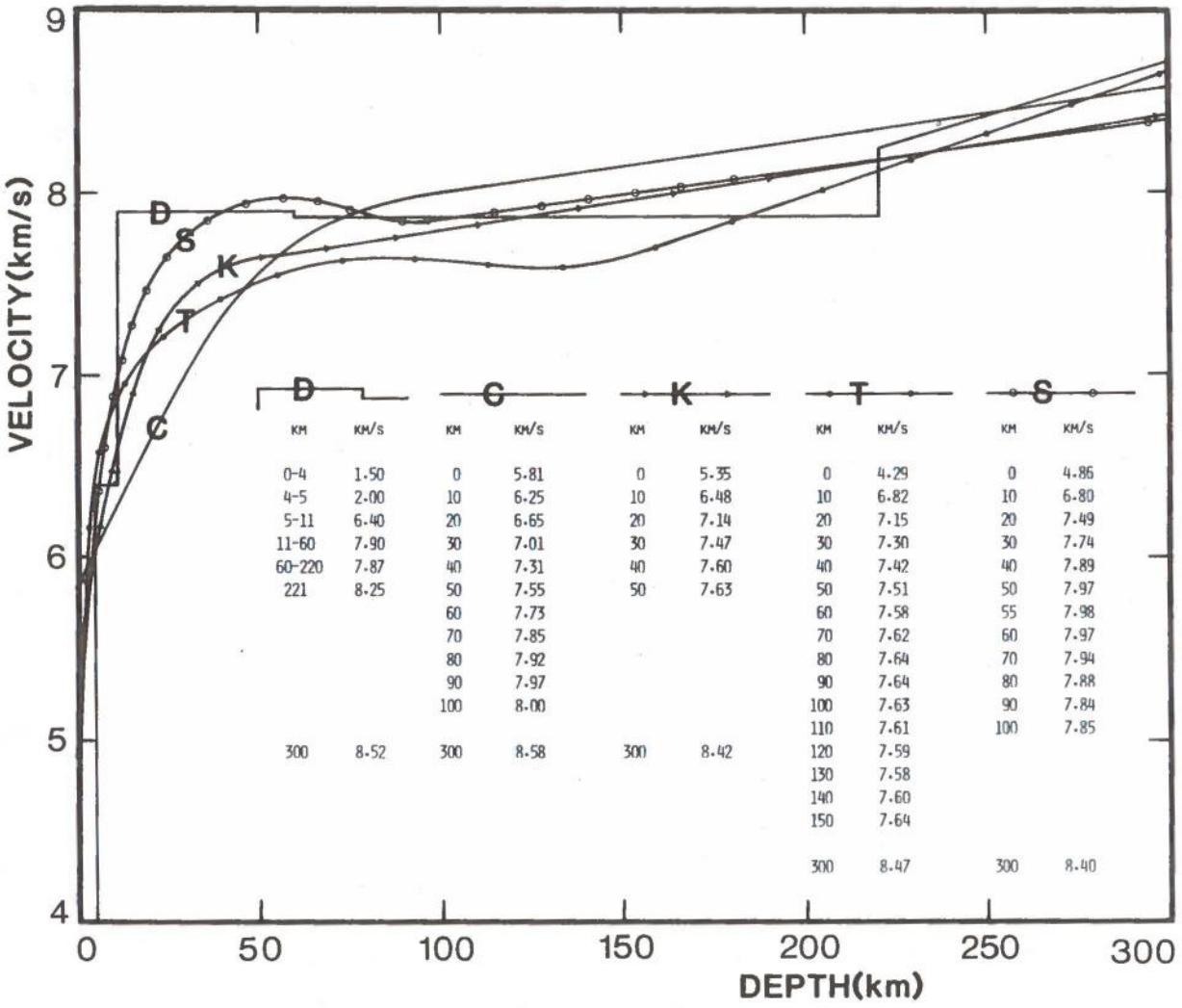

D		C		K		T		S	
KM	KM/S	KM	KM/S	KM	KM/S	KM	KM/S	KM	KM/S
0-4	1.50	0	5.81	0	5.35	0	4.29	0	4.86
4-5	2.00	10	6.25	10	6.48	10	6.82	10	6.80
5-11	6.40	20	6.65	20	7.14	20	7.15	20	7.49
11-60	7.90	30	7.01	30	7.47	30	7.30	30	7.74
60-220	7.87	40	7.31	40	7.60	40	7.42	40	7.89
221	8.25	50	7.55	50	7.63	50	7.51	50	7.97
		60	7.73			60	7.58	55	7.98
		70	7.85			70	7.62	60	7.97
		80	7.92			80	7.64	70	7.94
		90	7.97			90	7.64	80	7.88
		100	8.00			100	7.63	90	7.84
						110	7.61	100	7.85
300	8.52	300	8.58	300	8.42	120	7.59		
						130	7.58		
						140	7.60		
						150	7.64		
						300	8.47	300	8.40

Fig. 4.1 The four velocity models which have been tested, represented by smooth functions together with the 'reference' oceanic model D.

D Parameterized earth model PEM-Oceanic (Dziewonski et al, 1975)

C Based on PEM-continental (Dziewonski et al, 1975)

K Based on refaction studies (Palmason, 1971; Flovenz, 1980; Gebrande et al, 1980)

T Additional information to those for K on upper mantle low velocity zone from surface wave studies (R. Stefansson, 1980)

S A mean structure for the Iceland region as shown on Fig. 4.2 (R. Stefansson, 1980).

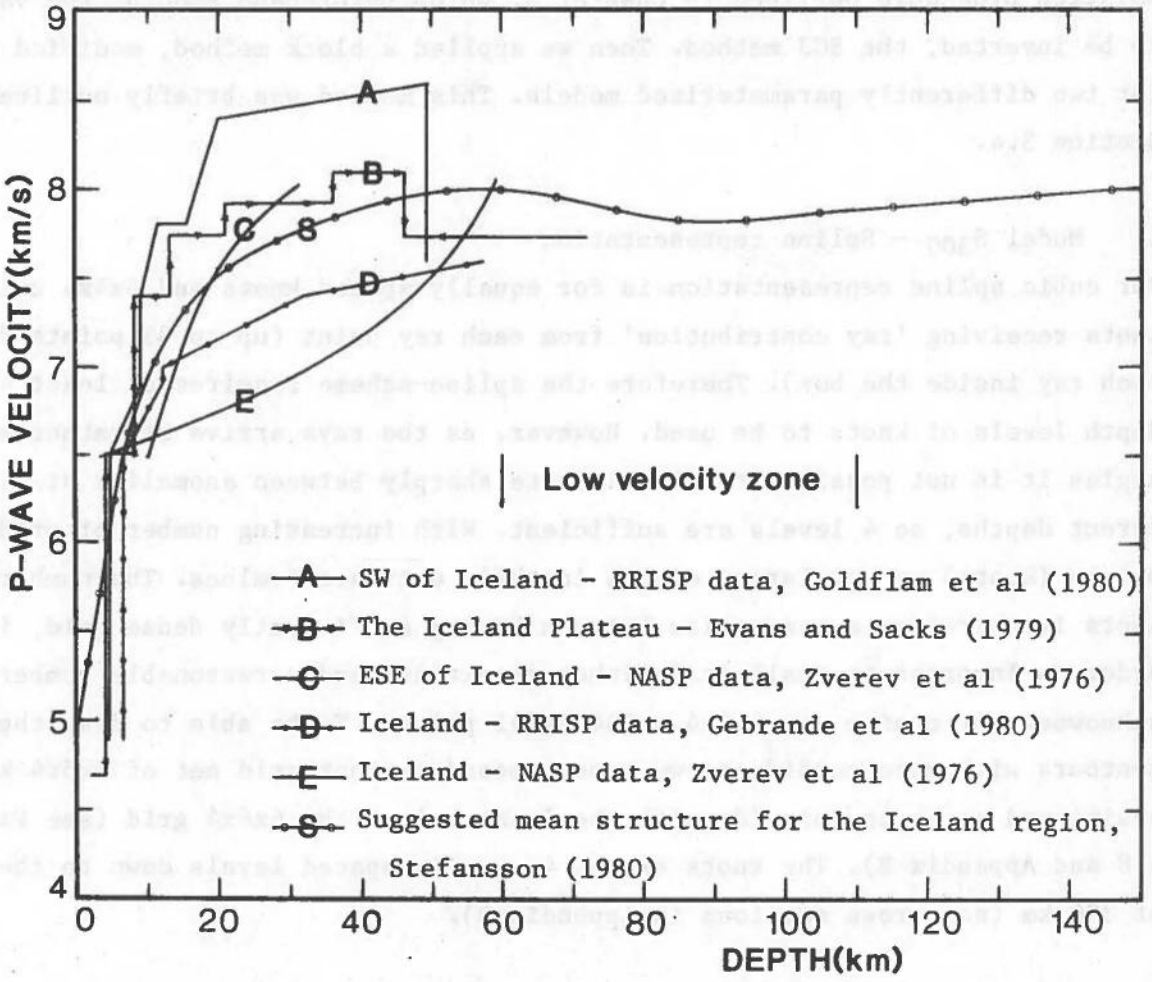

Fig. 4.2 For the uppermost 60 km the model S is constructed as the average of the 5 other models, representing different ares of the Iceland region. At approx. 60 km depth a low velocity zone comes into being as inferred from recent surface wave studies (Stefansson & Halldorsson, 1980). Below the low velocity zone (40-60 km thick) S follows a standard oceanic model, PEM-O (Dziewonski et al, 1975).

(b) 3-D model parameterization

Analogously, a few experiments with model parameterization were made for the purpose of improving the data variance reduction, and secondly to better establish the velocity anomalies. In our first trial we utilized the spline interpolation procedure outlined in Chapter 3, which beforehand smooths the values to be inverted, the SGJ method. Then we applied a block method, modified ACH, for two differently parameterized models. This method was briefly outlined in Section 3.4.

I. Model S_{300} - Spline representation

Our cubic spline representation is for equally spaced knots and 4x4x4 units of knots receiving 'ray contribution' from each ray point (up to 35 points for each ray inside the box). Therefore the spline-scheme requires at least 4 depth levels of knots to be used. However, as the rays arrive at rather steep angles it is not possible to discriminate sharply between anomalies at different depths, so 4 levels are sufficient. With increasing number of grid points (knots) we get larger errors in their estimated values. The number of knots is therefore a compromise between having sufficiently dense grid, in order to incorporate small-scale inhomogeneities, and a reasonable number of unknowns. Our choice was 6x6x4 = 144 model points. To be able to draw the contours with more confidence we superimposed another grid net of 5x5x4 knots positioned so as to coincide with the 'centers' of the 6x6x4 grid (see Fig. 4.8 and Appendix B). The knots are at 4 equally spaced levels down to the depth of 300 km (see cross sections in Appendix B).

II. Model N_{300} - Non-spline representation

Instead of giving 64 knots some ray values for each ray point as in the spline representation we now assign the exact ray length inside each block to its imagined centered knot. In order to have an option for a direct comparison to the spline representation, we used the same basic configuration here as for S_{300}. Not unexpectedly the essential features of the velocity anomalies for this model are similar to those of the S_{300} model (see Appendix B).

III. Model N_{375} - Non-spline representation

Here the uppermost layer is 75 km thick, which is close to the presumed standard thickness of the oceanic lithosphere. The depth range of this model is 375 km (75+100+100+100) and it represents a more uniform block structure than model N_{300}. The N_{375} model gave a better fit to the observed residual times than the other two (Figs. 4.3, 4.4). Therefore, in the presentation of results (Section 4.3) we will present the results from this particular model but refer to models S_{300} and N_{300} in the Appendix regarding special features.

4.2 On the Choice of an Adequate Smoothing Parameter θ^2

A graphical display was used for finding the 'best' smoothing parameter. By plotting the RMS slowness-perturbation (rmsslo) against the variance improvement yields a set of tradeoff curves (Figs. 4.3-4.4). From these curves it is obvious at which range a decrease of θ^2 will strongly alter the parameter estimates almost without improving the fit. The parameter rmsslo is defined as $\sqrt{1/m \langle|\hat{x}|^2\rangle}$, where m is the number of unknowns in the models and $\langle|\hat{x}|\rangle$ is the square length of the estimation solution vector.

Let us call the maximal diagonal element of the normal equation matrix A^tA for M_d. The smoothing parameter θ^2 is a fraction of M_d depending upon the fractional number F, often called the supplied smoothing parameter, that is, $\theta^2 = FM_d$. The figures 4.3 and 4.4 show how the supplied smoothing parameters F affect the solution. With decreasing F the fit of the derived model to the data increases but exhibits larger anomalies characterized by relatively rapid fluctuation between adjacent knots. The resolution and standard error for each knot were also plotted and these points lie within a semi-ellipse as illustrated in Fig. 4.5. The effect of increasing the smoothing parameter is to reduce the standard error of poorly resolved knots but not to the same extent for those with good resolution. This is because points with high resolution 'have to' move towards the peak of the semi-ellipse as the resolution decreases with increasing θ^2 (see Fig. 4.6).

The 'cut off' point for the non-spline curves in Figs. 4.3 and 4.4 is much clearer than for the spline curve. There is obviously no sense in using lower

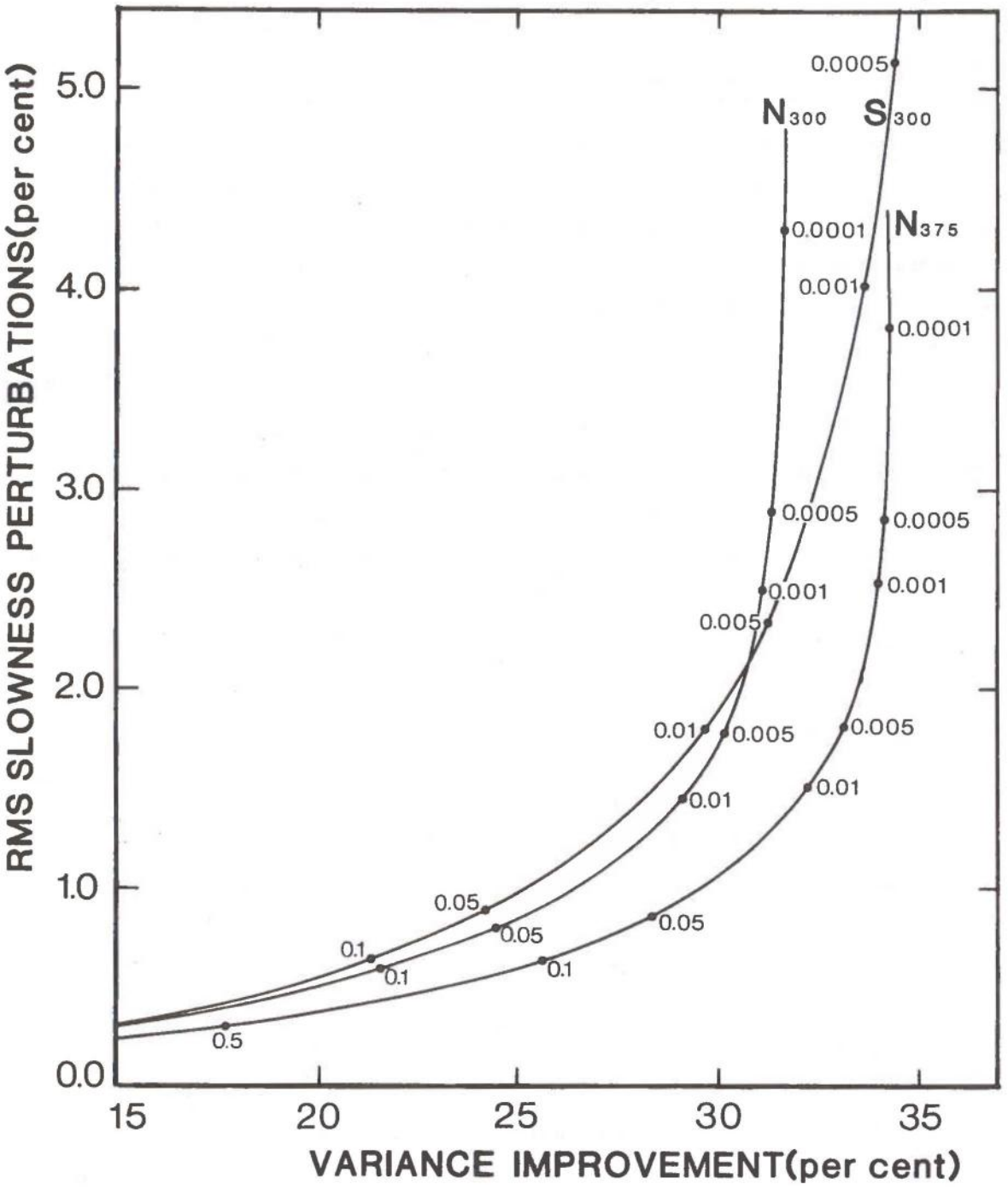

Fig. 4.3 The RMS slowness perturbations versus variance improvement in residuals for various values of the supplied smoothing parameter F. The relation between F and the actual stochastic smoothing parameter $\theta^2 = FM_d$, where M_d is max. (diagonal element of A^tA). The trade-off curves correspond to models of 5x5x4 knots and F = 0.01 was chosen in this study.

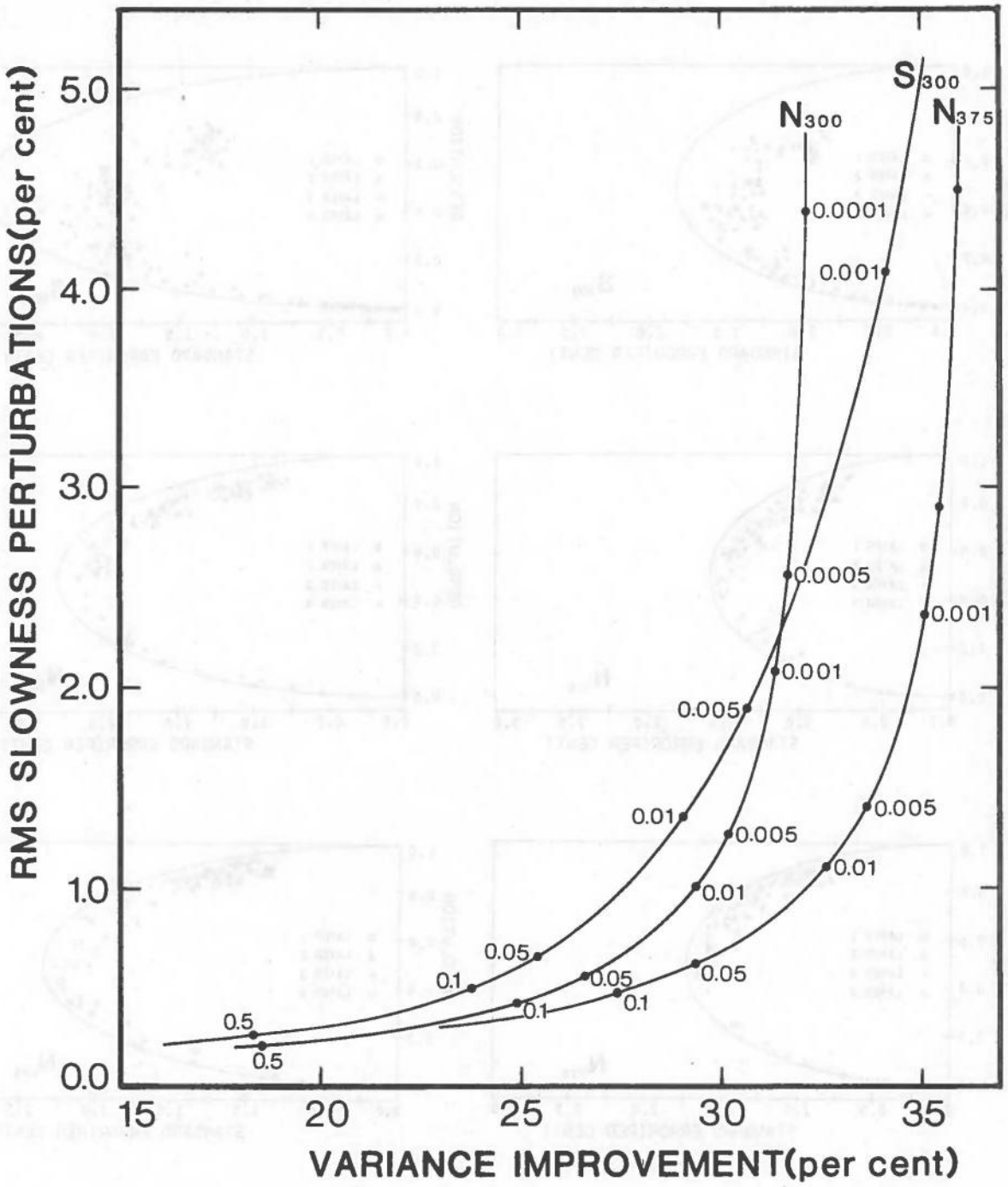

Fig. 4.4 The RMS slowness perturbations versus variance improvement in residuals for various values of the supplied smoothing parameter F. The relation between F and the actual stochastic smoothing parameter $\theta^2 = FM_d$, where M_d is max. (diagonal element of A^tA). The trade-off curves correspond to models of 6x6x4 knots and F = 0.005 was chosen in this study.

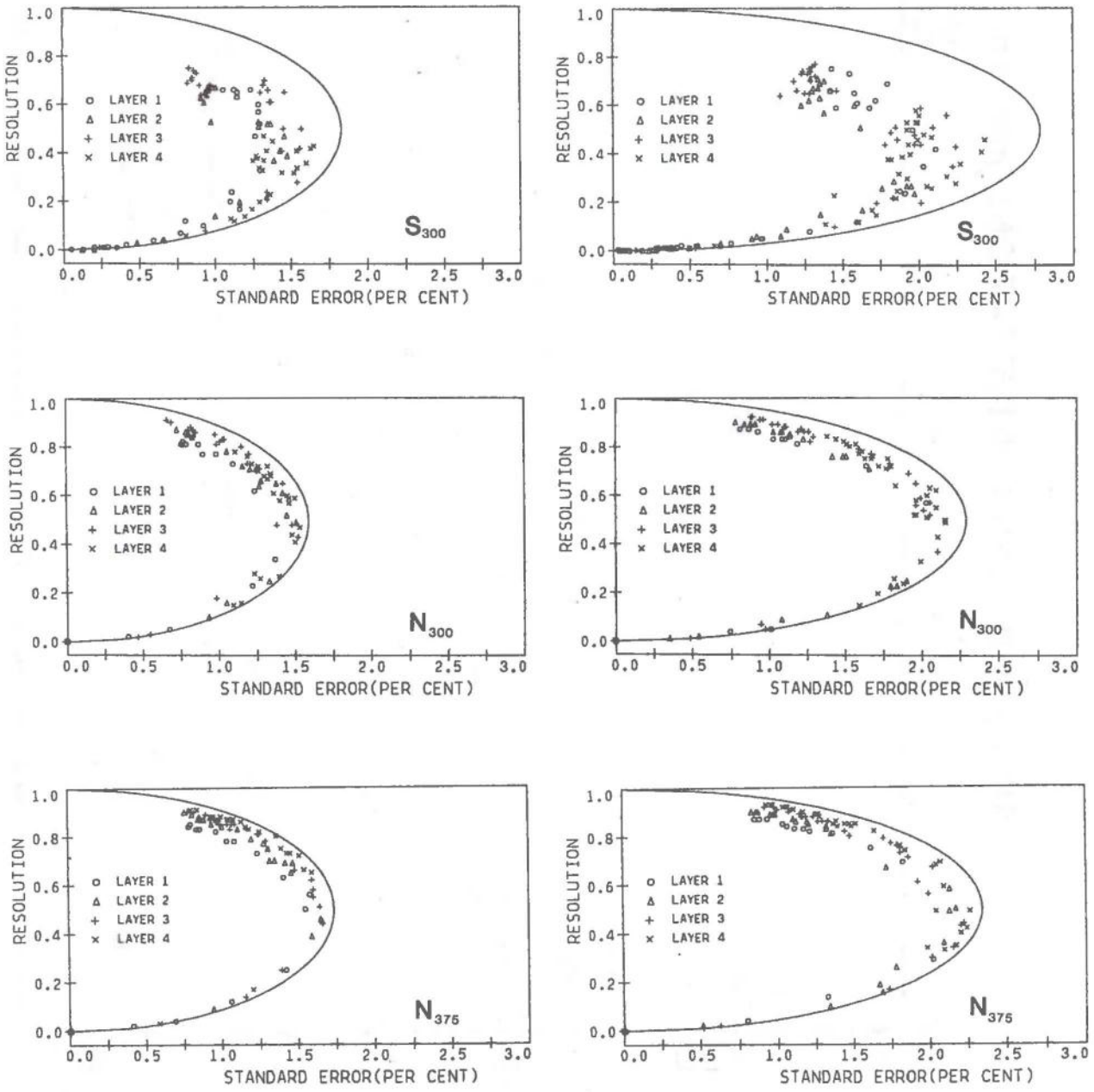

MODEL BOXES OF 5x5x4 KNOTS

SMOOTHING PARAMETER F = 0.01

MODEL BOXES OF 6x6x4 KNOTS

SMOOTHING PARAMETER F = 0.005

Fig. 4.5 Resolution versus standard error for all knots in the three different models, N_{375} presented in Fig. 4.7 and S_{300}, N_{300} shown in Appendix B. The points lie within a semi-ellipse given the formula $s = \sigma_d(r-r^2)^{\frac{1}{2}}/\theta$ (ch. 3, eq. (37)).

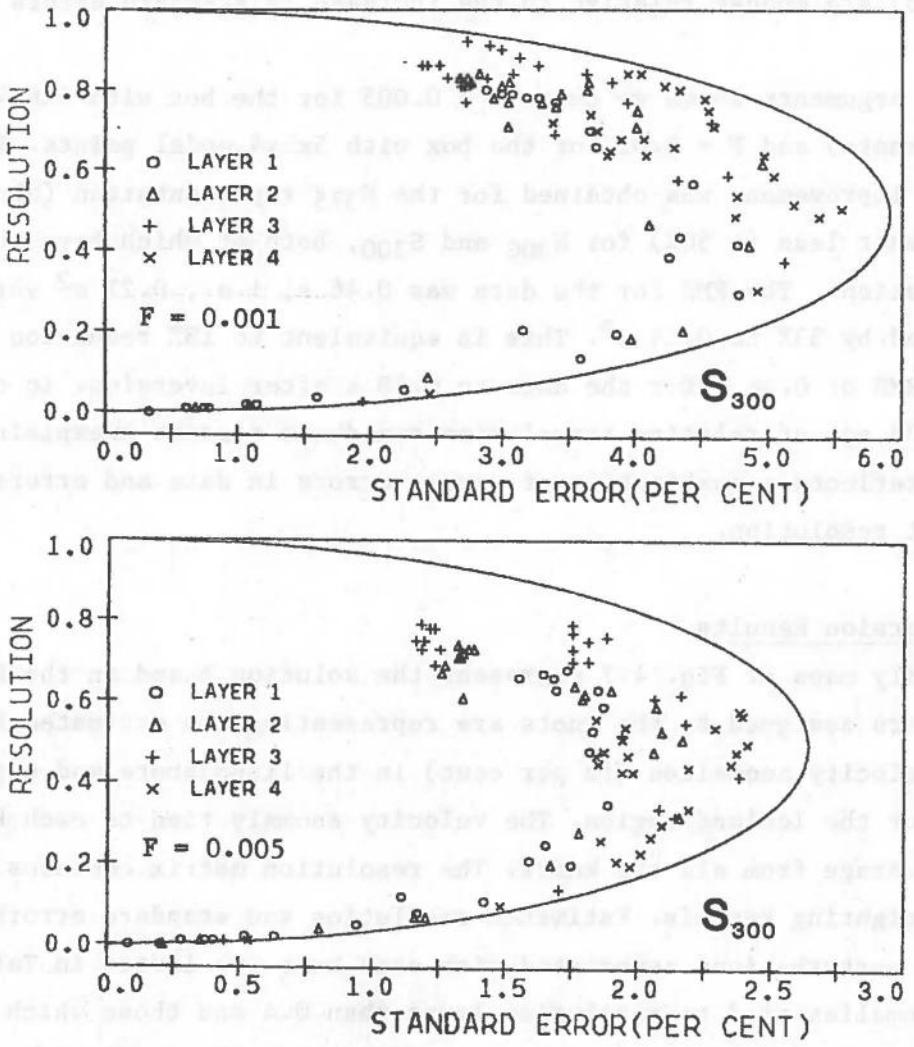

Fig. 4.6 The graphic plots demonstrate the effects on the resolution and standard error by varying θ^2 (note the change in scale on the horizontal axis). When resolution is poor, relaxation of the damping (θ^2) greatly magnifies the error with little improvement in resolution. Conversely, when resolution is good, decreased damping results in substantially improved resolution with only modest increase in the error.

F than 0.005 for the non-spline representation. For the spline representation one can get nearly 2% better variance improvement by using 0.001 instead of 0.005, but not considered significant as the increase in the anomaly estimates (Fig. 4.3) are modest relative to the increase in standard errors (Fig. 4.6).

From the arguments above we chose F = 0.005 for the box with 6x6x4 model points (knots) and F = 0.01 for the box with 5x5x4 model points. The best variance improvement was obtained for the N_{375} representation (about 33%) but somewhat less (~ 30%) for N_{300} and S_{300}, both of which have the same basic configuration. The RMS for the data was 0.46 s, i.e., 0.21 s^2 variance, this is reduced by 33% to 0.14 s^2. This is equivalent to 18% reduction in residuals, from an RMS of 0.46 s for the data to 0.38 s after inversion. In other words about 0.38 sec of relative travel time residuals remains unexplained, which in turn reflects a combination of random errors in data and errors owing to imperfect resolution.

4.3 Inversion Results

The anomaly maps of Fig. 4.7 represent the solution based on the N_{375} model. The numbers assigned to the knots are representing the estimated P-wave fractional velocity anomalies (in per cent) in the lithosphere and upper asthenosphere for the Iceland region. The velocity anomaly tied to each knot is a weight average from all the knots. The resolution matrix contains information on the weighting kernels. Estimated resolution and standard errors for the velocity perturbations associated with each knot are listed in Table 4.1. We rated anomalies tied to resolution lower than 0.4 and those which are lower than their standard errors not to be significant. The standard error estimates for significant anomalies are all around 1% in relative velocity deviation. The resolution values indicate how well each block is sampled, e.g., a block with 0.6 in resolution has got 60% contribution on its estimated velocity perturbation from the block itself and 40% from the other blocks. Blocks with zero resolution are not sampled at all and their assigned velocity anomalies are therefore ignored. For the non-spline representation the anomalies assigned to unsampled blocks are zero but have small, non-zero values for the spline representation as a result of the interpolation to nearby knots. The contours were drawn in view of the information from the resolution-standard error tables. Major results are as follows.

In layer 1 (Fig. 4.7a), which represents the uppermost 75 km, a broad and dominant low velocity zone is extending from the Tjörnes shearing (fracture) zone north of Iceland, southward to the Krafla area and then west-southwestward in direction to the Snæfellsnes area. This low coincides with a major part of the neovolcanic zone in northern and central Iceland together with late Quaternary and early Tertiary areas west of it. Pronounced low velocity values are tied to the Tjörnes shearing zone and the active Krafla volcanic area. Offshore there are only few significant anomalies and all of them represent a continuation of the pronounced high velocity regions in the southeastern and northwestern parts of the country. The grid points within Island itself are well resolved, that is, the resolution is around 80% and up to 90% in southern Iceland, which reflects a denser station network there. The standard error estimates for these most significant grid point values are around 1% relative velocity change. The capital letters A-A' and B-B' together with the heavy arrows indicate vertical cross-sections through the model box (Fig. 4.8).

In layer 2 (Fig. 4.7b), which ranges from 75 to 175 km depth, the low velocity zone is shifted southeastward compared to layer 1 and with the strongest anomalies south of Reykjanes, beneath the Hekla area and northeast of Kverkfjöll. A continuation of the high in the northwestern part of the country is obvious. In addition, two highs are prominent, namely, south of Iceland and northeast of Iceland. These areas are poorly sampled in layer 1, so a comparison between the two layers is not possible there.

For layer 3 (Fig. 4.7c), depth range 175-275 km, somewhat different features appear compared to the two uppermost layers. A significant low is covering an area south of the Tjörnes shearing zone and extending westward to the southwest of the Kolbeinsey ridge. Another low velocity zone, but a weaker one, is underneath central and southwest Iceland. The resolution values are even higher here than in layer two, most of them around 0.9 and with accompanying standard errors down to 0.8%.

Compared to the other two models S_{300}, N_{300} (see Appendix B) the low west of the Kolbeinsey ridge has almost extinguished but is comparatively strong south of the Tjörnes shearing zone. Also a weak but significant anomaly is found underneath central Iceland but the low east of the Reykjanes ridge is not observed. The downward shift in depth range of the N_{375} model's third layer by 25 km compared to the other two models seems to be enough to visualize a pattern from layer 4 of the S_{300} and N_{300} models.

Layer 4 (Fig. 4.7d) covering the depth range of 275-375 km, is marked by a prominent velocity low beneath central Iceland. This is a relatively broad area with maximal east-west and north-south extension around 300 and 200 km respectively. The resolution and standard error estimates are about the same as for layer 3. Comparing the main features of layer 4 for models S_{300} and N_{300} (see Appendix B) to this model (N_{375}) the areal extension of the low velocity area (in view of significant values) is obviously about the same. On the other hand the anomalies are generally stronger in the S_{300}, N_{300} models than in the N_{375} model, which in turn presumably reflects the difference in depth extent. In general larger depth extent of the model claims weaker anomalies to explain the observed time residuals.

For the lower layers most of the edge points are sufficiently well resolved. Significant anomaly contours can therefore be drawn quite to the edge of the box, as is the case for the highs around the country in layers 3 and 4.

Vertical cross-sections

We made two vertical cross-sections (Figs. 4.8) of the above-mentioned four-layer anomaly patterns. The sections visualize the main lows and highs of all four layers, indicating an anomalous mantle beneath Iceland. Below circa 250 km depth of central Iceland a dominant low velocity zone might indicate a mantle plume or a so-called hot spot. Another strong low in the uppermost 70-80 km is beneath almost the whole of Iceland except for the periphery of the oldest rocks mainly in the SE and NW parts of the country. A broad 'transition zone' of relatively low velocities including a few strong low velocity pockets (see layers 2,3 of the anomaly maps) is clearly connecting the two major lows. Analogous cross-sections through the other two model boxes (S_{300}, N_{300}) indicate the same main features as well (see Appendix B).

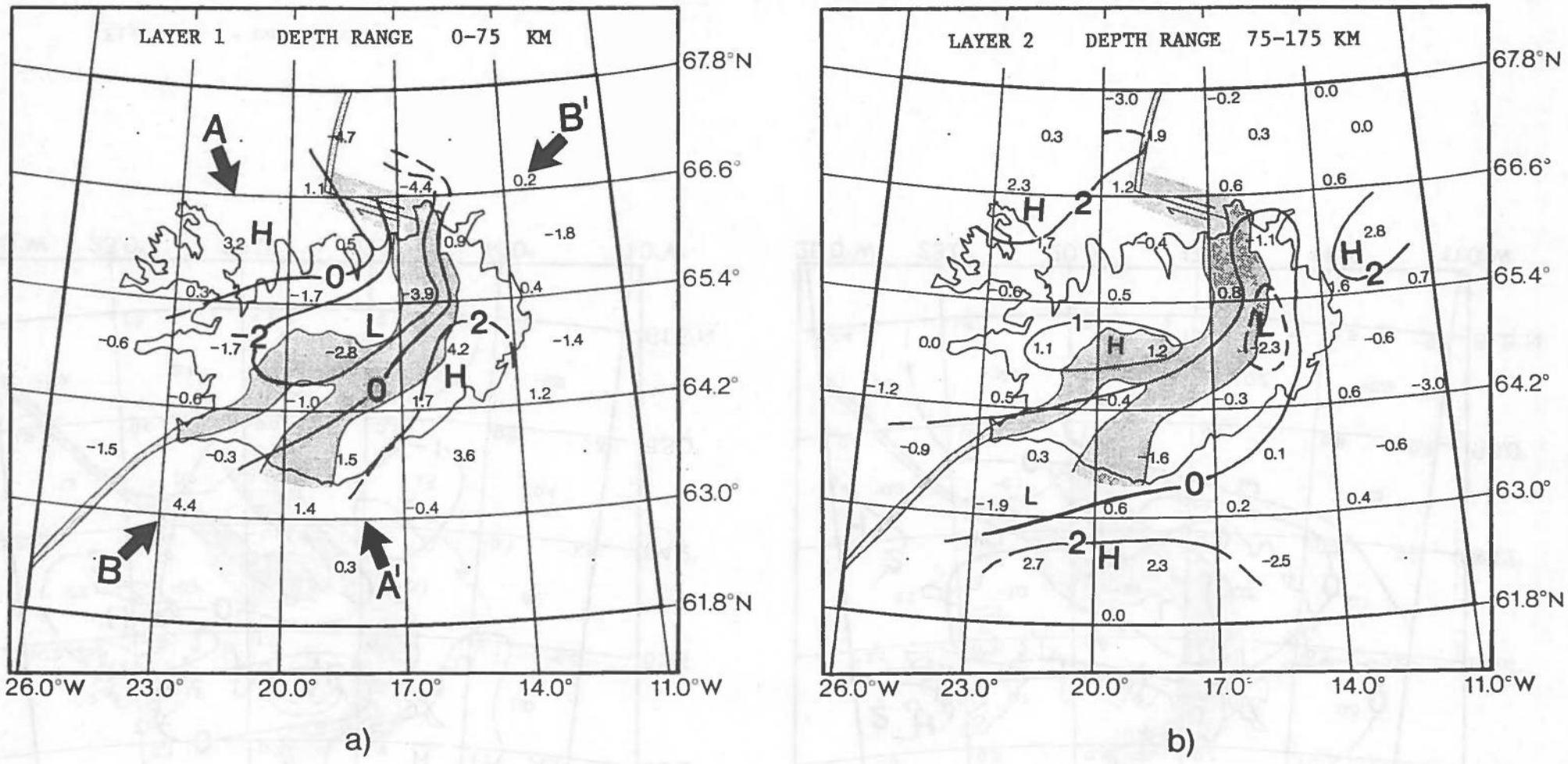

Fig. 4.7 (a) Velocity perturbations (in per cent) for layer 1. Areas of high and low velocities are indicated by capital letters H and L. The capital letters A-A' and B-B' together with the heavy arrows indicate vertical cross-sections through the model box as shown in Fig. 4.8. Resolution and standard errors for all knots are displayed in Table 4.1. (b), (c) and (d): caption as in (a) applied to the respective layers.

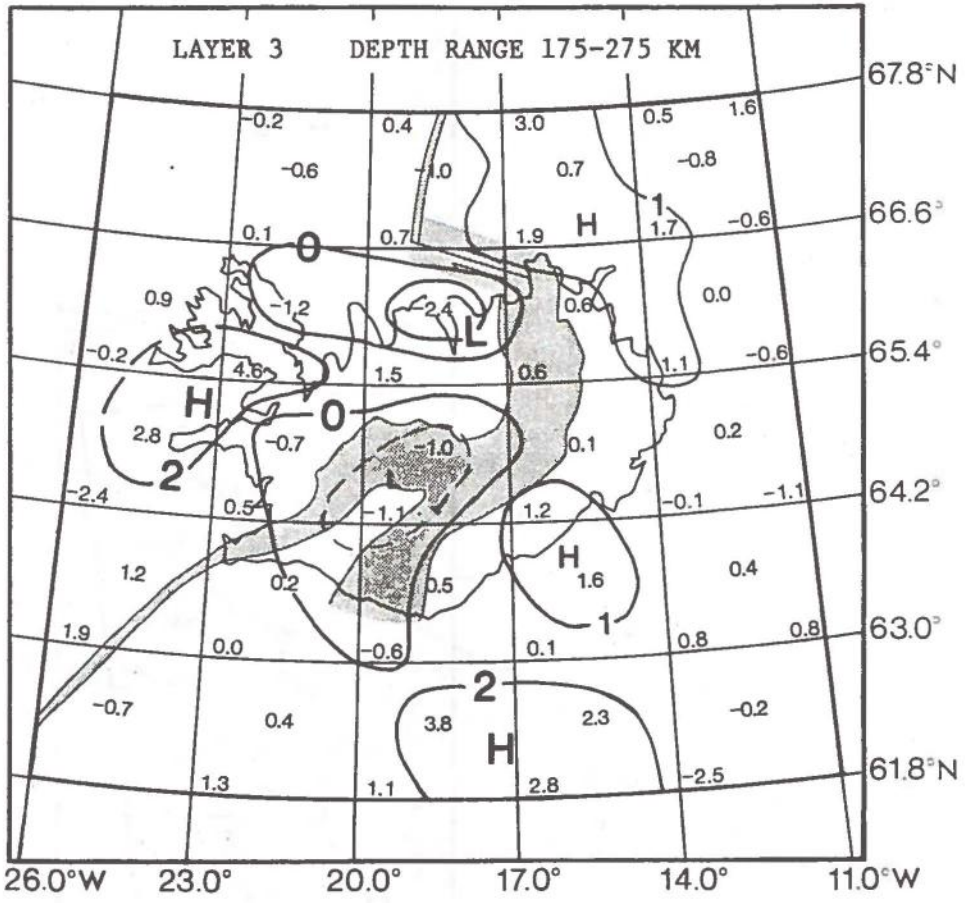

c)

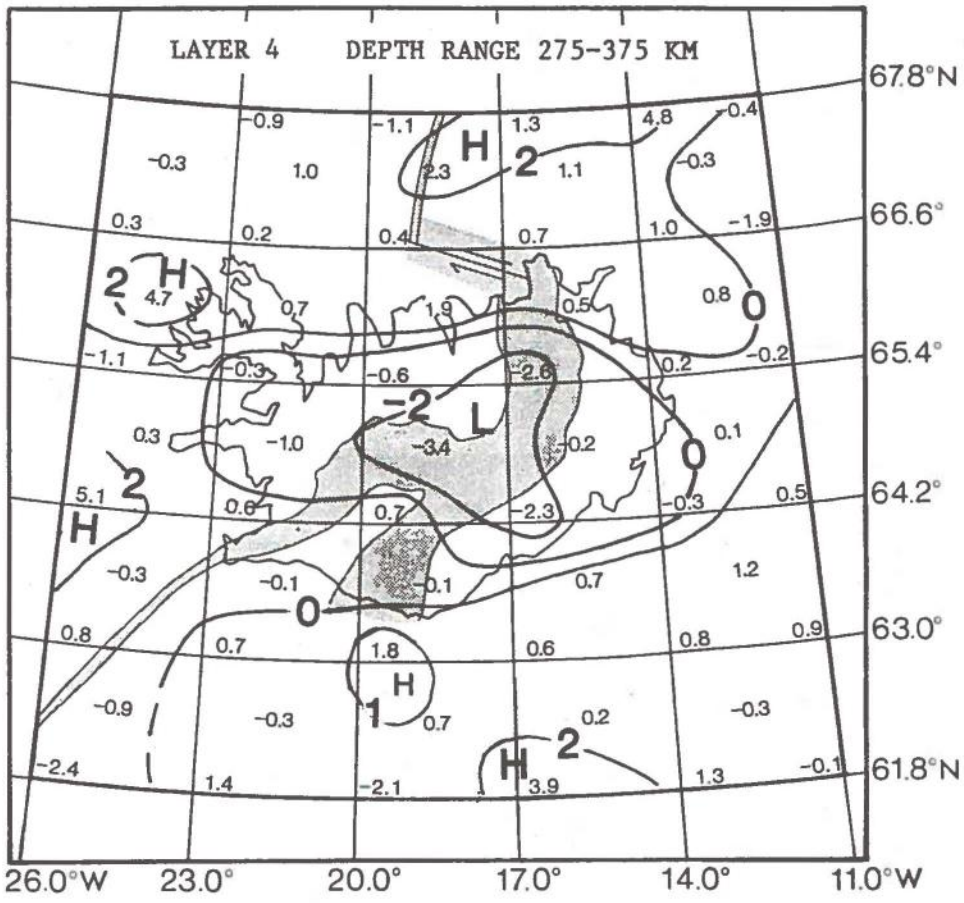

d)

Fig. 4.7 - continued.

RESOLUTION DISTRIBUTION IN LAYER...1...

0.0	0.0	0.0	0.0	0.0	0.0
	0.0	0.0	0.6	0.0	0.0
0.0	0.0	0.8	0.8	0.0	0.0
	0.0	0.6	0.9	0.8	0.1
0.0	0.1	0.8	0.9	0.8	0.0
	0.0	0.8	0.8	0.8	0.5
0.0	0.8	0.9	0.9	0.8	0.0
	0.8	0.8	0.8	0.7	0.0
0.0	0.3	0.9	0.7	0.0	0.0
	0.0	0.0	0.0	0.0	0.0
0.0	0.0	0.0	0.0	0.0	0.0

RESOLUTION DISTRIBUTION IN LAYER...2...

0.0	0.0	0.2	0.4	0.0	0.0
	0.0	0.4	0.8	0.7	0.1
0.0	0.2	0.9	0.9	0.8	0.0
	0.0	0.7	0.9	0.9	0.8
0.0	0.7	0.9	0.9	0.9	0.6
	0.7	0.9	0.9	0.9	0.8
0.1	0.9	0.9	0.9	0.8	0.5
	0.8	0.9	0.9	0.8	0.5
0.0	0.8	0.9	0.9	0.3	0.0
	0.0	0.6	0.7	0.4	0.0
0.0	0.0	0.5	0.0	0.0	0.0

STD-ERR. DISTRIBUTION IN LAYER...1...

0.0	0.0	0.0	0.0	0.0	0.0
	0.0	0.0	1.6	0.0	0.0
0.0	0.0	1.2	1.1	0.8	0.0
	0.0	1.4	0.8	0.9	1.1
0.0	1.3	1.4	0.9	1.1	0.0
	0.4	1.1	1.0	1.0	1.6
0.0	1.2	0.9	0.9	1.6	0.0
	1.4	0.8	0.8	1.2	0.0
0.0	2.0	1.0	1.8	0.0	0.0
	0.0	0.0	0.7	0.0	0.0
0.0	0.0	0.0	0.0	0.0	0.0

STD-ERR. DISTRIBUTION IN LAYER...2...

0.0	0.0	1.7	2.1	0.5	0.0
	0.0	1.6	1.1	1.5	0.9
0.0	1.7	1.2	1.0	1.3	0.0
	0.0	1.3	0.9	0.9	1.3
0.0	1.7	1.0	0.9	1.0	2.1
	1.4	0.9	0.8	0.9	1.3
1.3	1.1	0.8	0.9	1.3	2.2
	1.2	0.9	0.8	1.0	1.6
0.0	1.4	1.1	1.2	1.8	0.0
	0.0	1.5	1.4	1.7	0.0
0.0	0.0	2.1	0.0	0.0	0.0

RESOLUTION DISTRIBUTION IN LAYER...3...

0.0	0.6	0.7	0.8	0.7	0.3
	0.0	0.6	0.9	0.9	0.4
0.0	0.6	0.9	0.9	0.9	0.3
	0.3	0.8	0.9	0.9	0.9
0.0	0.8	0.9	0.9	0.9	0.8
	0.7	0.9	0.9	0.9	0.8
0.7	0.9	0.9	0.9	0.9	0.7
	0.8	0.9	0.9	0.9	0.6
0.8	0.9	0.9	0.9	0.8	0.2
	0.5	0.8	0.6	0.8	0.1
0.0	0.6	0.7	0.4	0.4	0.0

RESOLUTION DISTRIBUTION IN LAYER...4...

0.0	0.4	0.8	0.9	0.8	0.4
	0.0	0.7	0.7	0.9	0.8
0.3	0.8	0.9	0.9	0.9	0.9
	0.8	0.9	0.9	0.9	0.9
0.6	0.9	0.9	0.9	0.9	0.8
	0.7	0.9	0.9	0.9	0.8
0.7	0.9	0.9	0.9	0.9	0.8
	0.8	0.9	0.9	0.9	0.8
0.9	0.9	0.9	0.9	0.9	0.5
	0.2	0.8	0.7	0.8	0.6
0.4	0.7	0.7	0.5	0.8	0.3

STD-ERR. DISTRIBUTION IN LAYER...3...

0.0	0.6	1.9	1.8	2.0	2.0
	0.0	1.6	1.1	1.1	1.7
0.0	2.0	1.3	1.2	1.2	2.2
	1.4	1.1	1.0	1.0	1.1
0.5	1.5	1.0	1.0	1.1	1.7
	1.5	1.0	0.8	0.9	1.3
1.8	1.3	1.0	0.9	1.2	1.8
	1.2	1.1	0.8	0.9	1.6
1.8	1.3	1.2	1.2	1.5	1.7
	1.6	1.3	1.6	1.3	1.2
0.0	1.9	1.8	2.2	2.2	0.0

STD-ERR. DISTRIBUTION IN LAYER...4...

0.0	2.2	1.5	1.4	1.8	2.2
	0.6	1.4	1.5	1.1	1.4
2.1	1.4	1.3	1.3	1.0	1.5
	1.4	0.9	1.1	1.1	1.1
2.1	1.4	0.9	1.0	1.0	1.5
	1.6	0.9	0.8	0.9	1.3
2.1	1.2	1.3	0.9	1.1	1.7
	1.2	1.0	1.0	1.0	1.4
1.5	1.1	1.0	1.1	1.1	2.1
	1.2	1.2	1.5	1.2	1.6
2.3	1.8	2.0	2.3	1.7	2.1

Table 4.1

Resolution and standard error for model N375. These data are also plotted in Fig. 4.5.

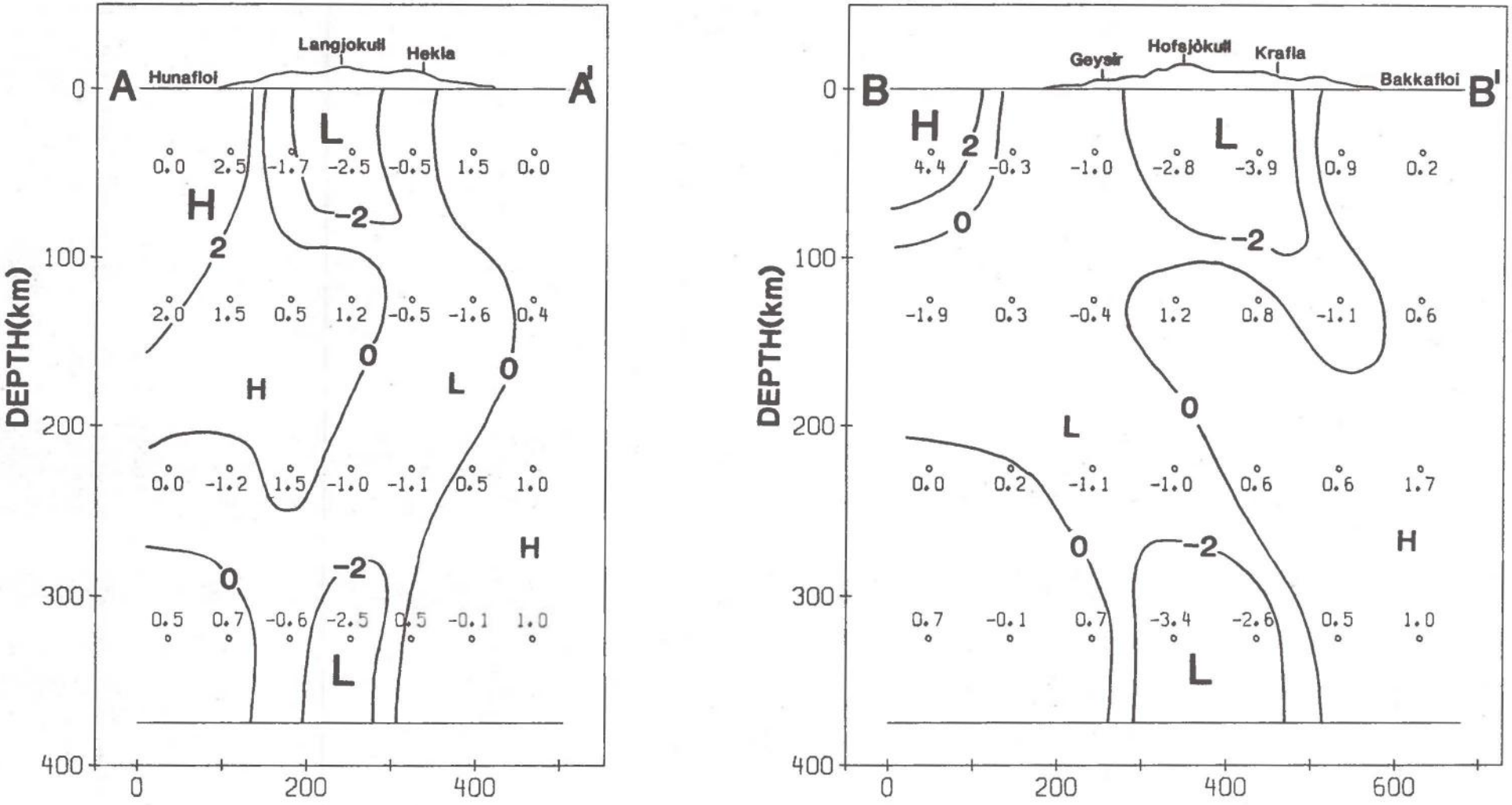

Fig. 4.8 The cross-sections span the latitude range from 63.0°N to 66.0°N, from NW to SE (A-A') and from SW to NE (B-B'). The depth to distance scale is 2:1.

4.4 On the Linearity of the Model

Our particular aim in this section is to examine the linearity of the method (Thomson & Gubbins, 1981) or more precisely to quantitatively estimate the nonlinear terms neglected by linearization of the travel time problem. In other words, the question is whether non-iterative inversion is sufficient or if an iterative procedure is needed.

If the linearization (Ch. 3, eq (5)) yields meaningful approximation to the truth (nonlinear terms are negligible) then noniterative inversion is sufficient. On the other hand, if the nonlinear terms neglected are significant (nonlinear problem), nonlinearity arises in the solution. In that case, by linearized inversion, it is necessary to solve the problem step-wise, which assures a good approximation for each step (iteration) provided a proper damping reducing each step length sufficiently (Levenberg, 1944; Marquardt, 1963).

According to Fermat's principle, small changes in the velocity structure of the medium produce changes in travel time which can be resolved into two components. The first of these is the contribution due to change in velocity along the initial ray path. The second is the effect of the change in ray path in the initial medium which is zero to first order because of Fermat's principle.

By 3-D ray tracing it is possible to estimate quantitatively the contribution to travel time due to non-linear terms. Defining

$$\partial T_{true} = T_{3D} - T_{1D}$$ where T is travel time obtained by ray tracing, and

$$\partial T_{pred} = \sum \frac{\partial T}{\partial s_k} \partial s_k$$ where $\frac{\partial T}{\partial s_k}$ are the 1-D partial derivatives

('ray contributions') defined by eq. (14) and ∂s_k is the derived solution after first iteration. ∂T_{pred} gives the contribution to the travel time caused only by change in medium, but along the initial ray path in the 1-D medium. By ∂T_{true} the 'true' or total time difference due to both changes

in medium and ray path is obtained. Therefore the difference $\partial T_{true} - \partial T_{pred}$ measures the actual non-linear terms omitted in the linearization of the travel time problem by use of Fermat's principle. Table 4.2 gives the magnitude of δT_{true} and δT_{pred} for the events of the data base. By comparison it is clear that a typical time difference is around 0.03 seconds which only contributes to about 0.2 km in ray path differences.

Generally $\frac{|\partial T_{true} - \partial T_{pred}|}{\partial T_{true}} \cdot 100$ ranges from zero to ten per cent.

ON THE WEST COAST OF AFRICA			ALEUTIAN ISLANDS		
23 09 74	0.282 S	12.830E	26 03 77	32.656N	48.922E
Station	∂T_{true}(s)	∂T_{pred}(s)	Station	∂T_{true}(s)	∂T_{pred}(s)
REY	-0.06	-0.06	REY	-0.57	-0.57
SNB	-0.56	-0.56	SID	0.16	0.16
LAU	0.00	0.01	VIR	0.20	0.20
AKU	0.28	0.25	SKH	0.17	0.18
EYV	-0.34	-0.37	SNB	0.20	0.21
			SEK	0.11	0.13
			LAU	-0.36	-0.33
			HVE	0.05	0.06
			SIM	-0.23	-0.17
			AKU	0.23	0.27
			EYV	-0.50	-0.46
			GST	-0.28	-0.27
			SKI	-0.23	-0.21
			HRN	-0.68	-0.63
			GÆS	-0.19	-0.18

Table 4.2

A tabulation of ∂T_{true} and ∂T_{pred} for two events of the data base.

5. GEOLOGY, GEOPHYSICS AND TECTONIC EVOLUTION OF ICELAND

5.1 Stratigraphic Classification and Main Tectonic Features of Iceland

Conventionally the volcanic pile of Iceland, which ranges in age back to around 16 m.y., is divided into four stratigraphic series. This division is based on climatic evidence from inter-lava sediments or volcanic breccias and on paleomagnetic reversal patterns supported by absolute age data. The four series are:

Postglacial : last 9000 to 13000 years

Upper Pleistocene : back to 0.7 m.y., corresponding to the present normal geomagnetic epoch, Brunhes

Plio-Pleistocene : 0.7-3.1 m.y., includes the Matsuyama epoch and terminates in the Gauss epoch at the Mammoth event

Tertiary : rocks older than 3.1 m.y.

The general tectonics of Iceland and the distribution of the four basic stratigraphic series just quoted are shown on Fig. 5.1. Of particular interest is the increasing age of the lava pile away from the neovolcanic zones. Note the direction of the regional dips towards the neovolcanic zones and the dominant dyke trends almost parallel to them. The dips increase gradually from near zero at the highest exposed levels of the pile to about 5-10° at sea level. The increase in depth is matched by individual lava groups thickening down the direction of dip (Fig. 5.2). Walker's interpretation that the regional dips (Walker, 1960; Bödvarsson & Walker, 1964) are due to sagging resulting from a stacking of lavas in an active zone agrees well with available observation. Furthermore, studies of regional dips accompanied with, e.g., age determinations, mapping of nonconformities, synclines and anticlines have led to the idea of shifts in activity of volcanic zones (see section 5.4).

The tectonics of Iceland is undoubtedly a result of its position on the Mid-Atlantic Ridge. Extensional features are dominating but on a minor level the tectonic pattern is, however, complicated. Active tectonism occurs in the neovolcanic zones and along transverse tectonic zones (shear zones) that connect offset segments of the neovolcanic zones, either internally or to the submarine mid-ocean ridge. The Tertiary and Plio-Pleistocene areas appear to be tectonically inactive except for transverse tectonic zones. Recent stress measurements in the

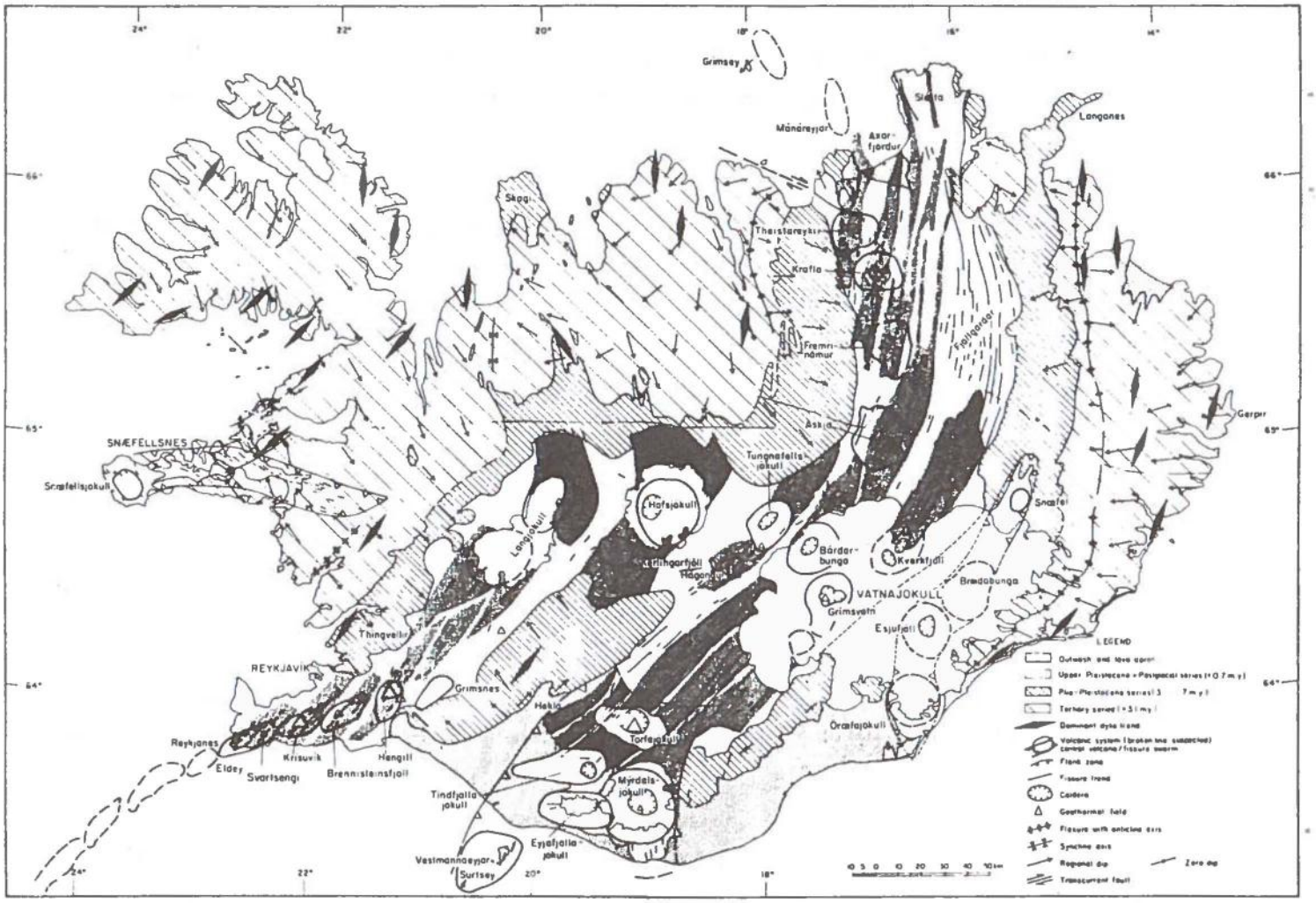

Fig. 5.1 Tectonic map of Iceland. From Sæmundsson (1979).

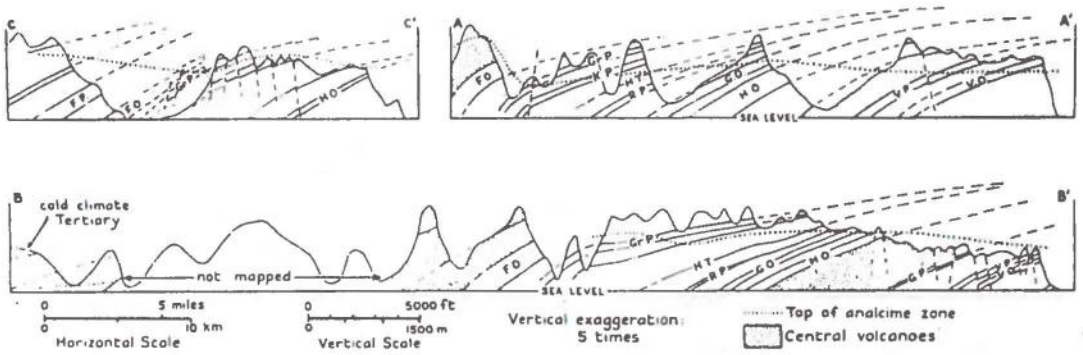

Fig. 5.2 Sections from east to west through the Tertiary series of eastern Iceland. The AA' section is the northernmost and the CC' section farthest to the south. Note thickness variations up dip and along strike. After Walker in G. Bödvarsson & Walker (1964).

Tertiary and Plio-Pleistocene areas (Haimson, 1979) yield not unexpected maximum compressive stress perpendicular to the active rift zones.

The volcanic rift zones display a great variety of volcanic forms, cut by numerous faults and open fissures running mainly NE-SW in southern Iceland but trending NNE-SSW in northern Iceland. Prevailing type of volcanoes are the eruptive fissures that may reach a length of several kilometers or even a few tens of kilometers. They erupt usually basaltic lavas which may flow over distances of tens of kilometers. Shield volcanoes are also fairly common and probably closely related to eruptive fissures (Walker, 1972). The other main type of volcanoes are the central volcanoes (Sæmundsson, 1978), characterized by repeated eruptions in a relatively small area. Most of the acidic rocks in Iceland are associated with the central volcanoes.

The volcanic rift zones have high heat flow as evidenced by the 15-20 high-temperature geothermal areas distributed more or less uniformly along the active zones. Most high-temperature areas are associated with central volcanoes, the Reykjanes peninsula being the main exception. In general, high heat flow results from long-term heating of the crust by intrusions. Outside the active zones of rifting and volcanism the presently available heat flow map for Iceland (Palmason et al, 1980) was obtained by measuring temperature gradient in boreholes (Fig. 5.3). The low heat flow values in eastern Iceland agree with the conclusion that the eastern volcanic zone is a relatively young feature formed perhaps 4 m.y. ago (see section 5.4). They indicate, when interpreted in terms of a cooling lithospheric plate moving away from a zone of crustal accretion, that the eastern Iceland lava pile is older than corresponds to its distance from the present eastern zone (Palmason, 1973).

Studies of postglacial lavas in Iceland have revealed a certain geographical pattern of composition (Jakobsson, 1972, 1979). Tholeiitic basalts are characteristic of the active zones of rifting. Alkali olivin basalts and transitional alkali basalts are found on the flank zones, at Snaefellsnes and in the southern part of the eastern zone (Fig. 5.4), which points to a different state of the upper mantle under the flanks compared to the active zones of rifting. This

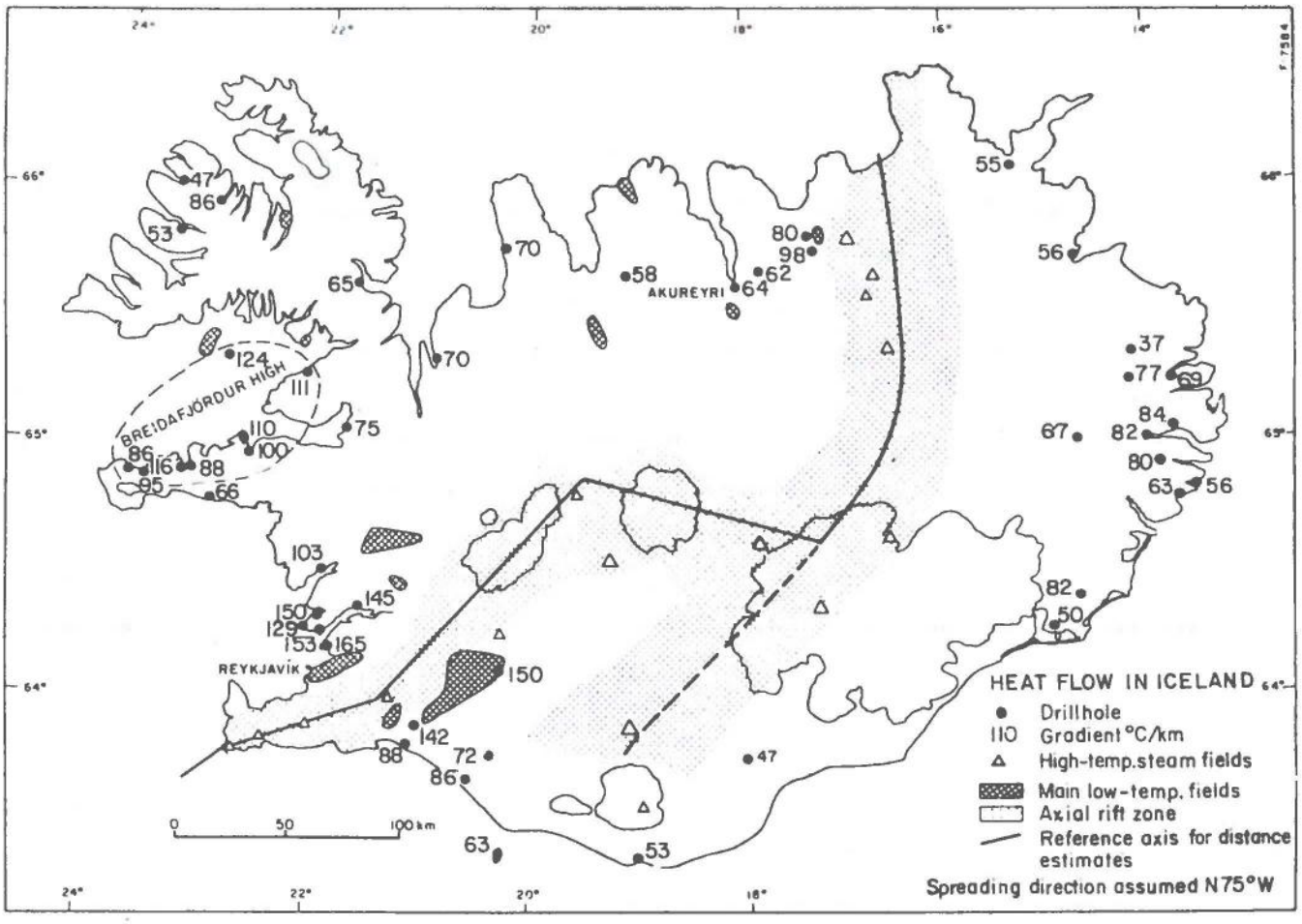

Fig. 5.3 The location of drillholes used to determine thermal gradients in Iceland. The main centers of geothermal activity are shown on the map. From Palmason et al (1979).

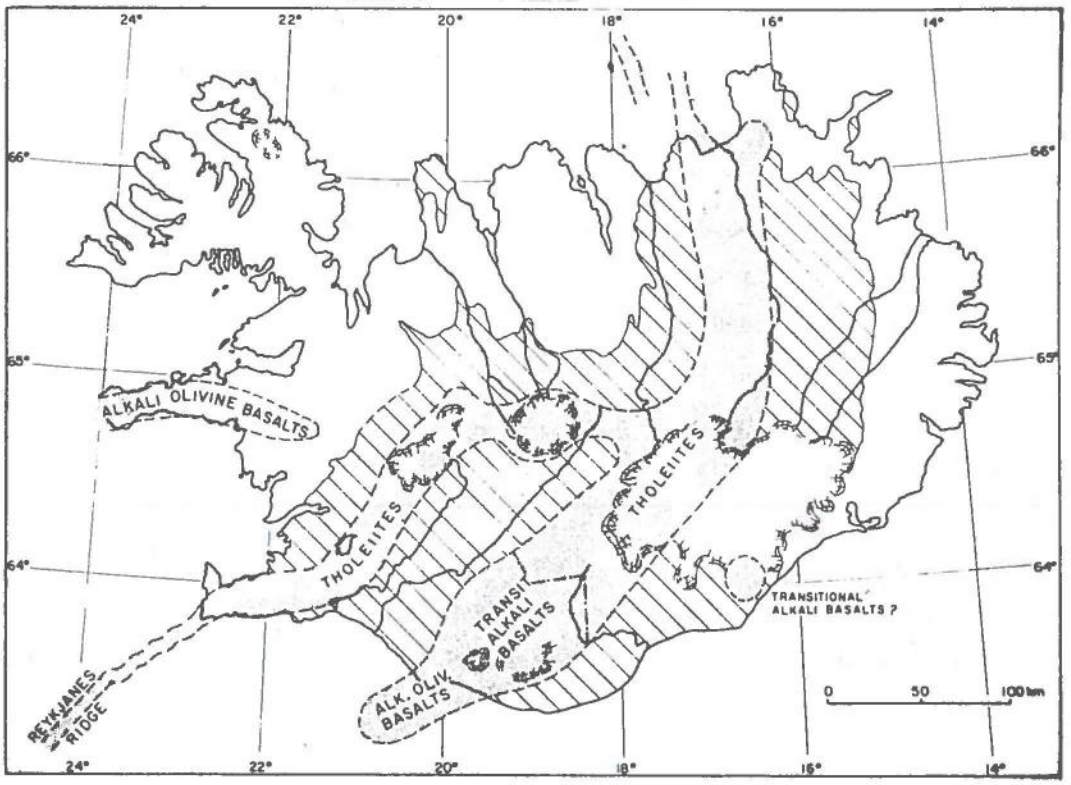

Fig. 5.4 Map of Iceland showing the Postglacial petrological zones (shaded), Plio-Pleistocene formations (oblique lines) and Tertiary formations (white). From Jakobsson (1979).

pattern appears to correlate with crustal structure and regional heat flow, (Palmason, 1973) such that the alkali basalts occur in areas of relatively low heat flow and relatively great depth to the upper mantle.

Two major shear or fracture zones connect the offset eastern volcanic rift zone to the Kolbeinsey Ridge and Reykjanes Peninsula, respectively (Figs. 5.5 and 5.11). A 75 km wide shear zone, by convention called Tjörnes Fracture Zone (TFZ), connects the Kolbeinsey Ridge to the eastern volcanic rift zone. Its existence is supported by earthquake distribution, submarine topography, strike slip faults on land, and offset of the volcanic zone (Sæmundsson, 1974). The TFZ trending approx. N67°W, which became operative around 4 m.y. ago, composes several subsiding troughs and volcanic chains in an echelon pattern. These features are distributed along the entire length (~ 100 km) of the fracture zone and are thought to be successively developed as spreading axes across it. The connecting segment between the Reykjanes Peninsula and the eastern volcanic zone has been referred to as the South-Iceland seismic zone. From the distribution of historic earthquakes, Stefansson (1967) noted the possibility of an E-W trending shear zone in southern Iceland at approximately 64°N. In addition, presently available focal mechanism solutions (Ward, 1971; Einarsson, 1979; Einarsson & Björnsson, 1979) indicate strike-slip movements there.

The Reykjanes Peninsula forms the transition between the submarine Reykjanes Ridge to the west and the south Iceland seismic zone to the east. The tectonics of the Peninsula show both ridge and transform fault characteristics but essentially it is rated as a leaky transform fault (e.g., Klein et al, 1977). A gradual transition from strike-slip to normal faulting (Fig. 5.5) occurs in the western part of it (Einarsson, 1979). Surface rupturing occurs along a series of northerly striking faults instead of one major easterly striking fault. The same applies for the South Iceland seismic zone and in general all transverse tectonic zones in Iceland, which might be natural when, e.g., taking into account the short age of these features compared to well developed ones like the San Andreas transform fault (Ward, 1971).

5.2 Previous Geophysical Research in Iceland

This section outlines major geophysical work contributing to present knowledge of the structure beneath Iceland. In addition the difference between Icelandic to adjacent mid-ocean structures is demonstrated.

Studies of the Icelandic crust by seismic refraction profiling were performed by Båth (1960), Tryggvason and Båth (1961), and Palmason (1963, 1971). Palmason's work included studies of more than 80 profiles distributed over Iceland, and resulted in a crustal model with four layers (0,1,2,3), a surface layer, two layers of Tertiary flood basalt and a layer with a mean P-wave velocity of 6.5 km/s, underlain by a mantle (layer 4) with an anomalously low P-wave velocity of 7.2 km/s. A reinterpretation of Palmason's data by Flovenz (1980) with the aid of synthetic seismograms gave a better fit to the data, especially as regards the observed amplitude variation. On this basis, Flovenz found it reasonable to divide the Icelandic crust into two seismic layers, the upper and the lower crust. The upper crust, corresponding to layers 0,1,2 in Palmason's four layer model, with continuously increasing P-wave velocity (2.0→6.5 km/s) with depth, and the lower crust with almost constant P-wave velocity (6.5 km/s) corresponds to layer 3 in the four layer model. The lower crust (layer 3) is considered to correspond to the oceanic layer 3 (Spudich & Orcutt, 1980). A typical depth in Iceland to the lower crust is 4-6 km but only 2-3 km for the standard oceanic crustal model.

In 1977 a long range seismic refraction experiment (RRISP 77) was performed with a profile (800 km) along the southeastern flank of the Reykjanes Ridge and across Iceland from SW to NE (drawn in on Fig. 5.5). Whereas earlier studies of comparatively short range profiles only permitted penetration of seismic waves down to 10-20 km, this deep seismic sounding experiment provided new information on the seismic structure down to 50-60 km depth (Gebrande et al, 1980). For the first time a rather sudden transition from the Icelandic to the oceanic crust and upper mantle structures was confirmed and localized. While the Icelandic crust differs from the oceanic one mainly by its greater thickness (10-15 km) and more definite lateral variations, the subcrustal structure is fundamentally different as visualized on Fig. 5.6. The Icelandic crust is underlain by a low P-wave

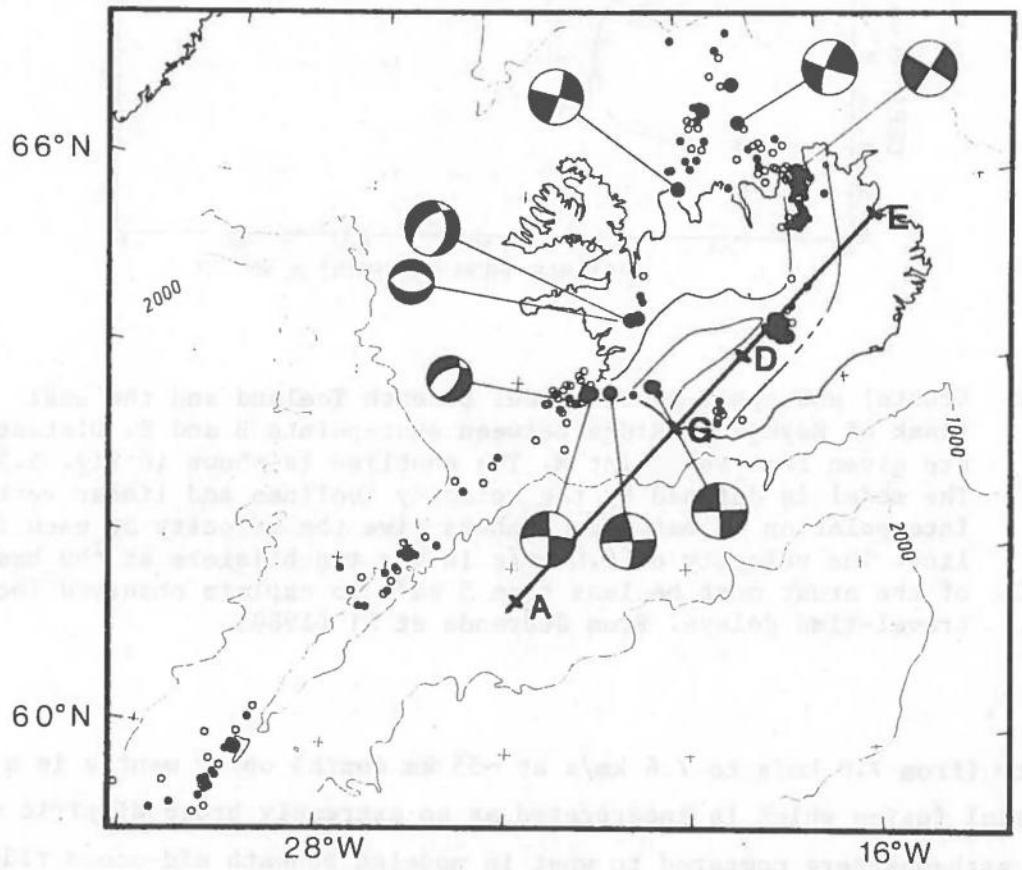

Fig. 5.5 Epicenters and focal mechanisms of earthquakes in Iceland and the northern part of the Reykjanes Ridge. Epicenters are taken from the PDE lists of USCGS, later NOAA and USGS, for the period 1962-1977. Open circles denote epicenters determined with fewer than ten P-wave readings or epicenters of earthquakes smaller than m_b = 4.5. Dots are epicenters of events of m_b = 4.5 and larger that are determined with ten or more readings. Large dots are epicenters of events of m_b = 5.0 and larger. The focal mechanisms are shown schematically as lower hemisphere equal area projections. The compressional quadrants (containing the least compressive stress axis) are shown black. The bathymetry is taken from a map by the Icelandic Hydrographic Service, Reykjavik, 1975. Depths are in meters. The volcanic rift zones of Iceland are shown. From Einarsson & Björnsson (1979).

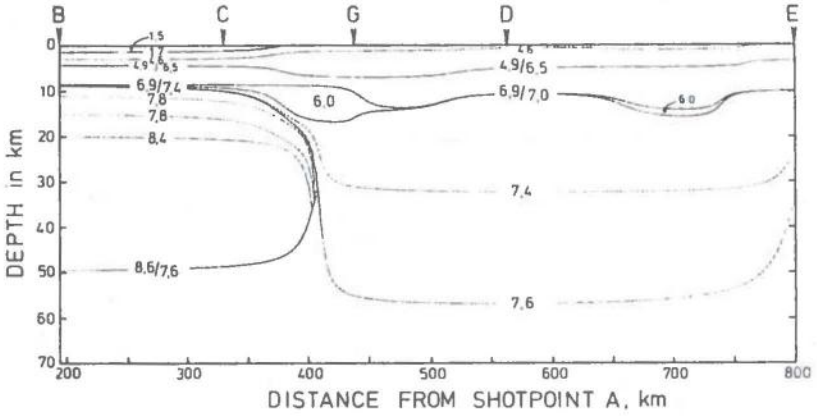

Fig. 5.6 Crustal and upper mantle model beneath Iceland and the east flank of Reykjanes Ridge between shot-points B and E. Distances are given from shotpoint A. The shotline is shown in Fig. 5.5. The model is defined by the velocity isolines and linear vertical interpolation in between. Numbers give the velocity at each isoline. The velocity of 6.0 km/s in the two blisters at the base of the crust must be less than 5 km/s to explain observed local travel-time delays. From Gebrande et al (1980).

velocity (from 7.0 km/s to 7.6 km/s at ~55 km depth) upper mantle in a state of partial fusion which is interpreted as an extremely broad diapiric updoming of the asthenosphere compared to what is modeled beneath mid-ocean ridges proper. The amount of partial melt was calculated from the P-wave velocity distribution and unusually high P/S ratio of up to 2.2 in the anomalous mantle compared to the normal ratio 1.76 found in the crust. The melt content is highest (17%-23%) in the uppermost mantle and decreases with increasing depth.

The transition of the subcrustal structure from Reykjanes Ridge to Iceland takes place within a very narrow zone below the shelf slope. Presumably this sharp boundary is not a special feature connected with the Reykjanes Fracture Zone but is present elsewhere around the island.

Palmason's model of crustal accretion mechanism (Fig. 5.7), which predicts the trajectories of lava elements being subject to both sagging and lateral movements, fits well with geological observations in eastern Iceland discussed earlier (see, e.g., Fig. 5.2). Later on, the staff of the Iceland Research Drilling Project (Gibson et al, 1979) found evidence for at least 2 km subsidence during crustal formation from the 2 km long core of a hole (lat. 65.0°N, long. 14.3°W) drilled near Reydarfjördur, Eastern Iceland. It was the continuously sub-aerial nature of the rock samples suggesting subsidence on a scale similar to the prediction of Palmason's model for crustal growth in Iceland. This model was further supported by recent crustal studies (Zverev et al, 1980) where combined reflection and refraction methods were used. The dip of refractors and reflectors toward the active zone of rifting and the absence of reflecting horizons below 8 km depth in the central part of the zone agrees with such a crustal accretion model.

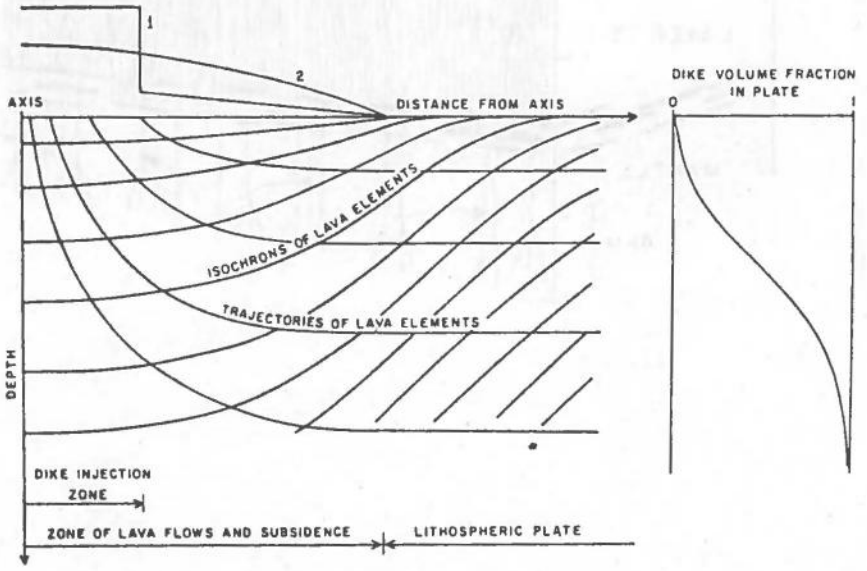

Fig. 5.7 Schematic model of crustal accretion in Iceland by dike intrusions and surface lavas in a single volcanic zone: 1. distribution of dike injection activity, 2. distribution of lava flows. Modified from Palmason (1973) in Palmason & Sæmundsson (1974).

Magnetotelluric soundings (Thayer et al, 1981) indicate an anomalous layer of high conductivity at the crust-mantle interface (Fig. 5.8). The depth to this layer is about 10 km beneath the active zone of rifting but increases to about 17 km below the Tertiary basalts in the east and the west. According to the RRISP results waves penetrating to greater depth show high P/S velocity ratio and this result is supported by a strong S wave attenuation across the Icelandic seismograph network. This in turn supports the magnetotelluric evidence for partially molten basalt immediately beneath the crust, not only underneath the volcanic rift zones, but under a major part of the country.

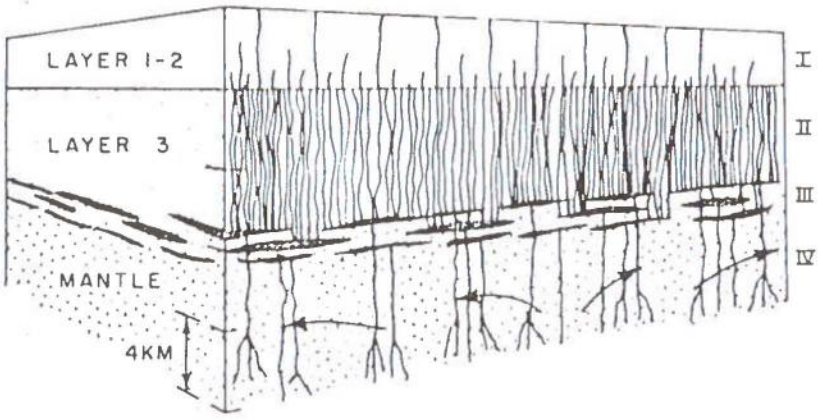

Fig. 5.8 Schematic representation of a vertical section through the northern neovolcanic zone. The seismic layering of Palmason (1971) is indicated on the left; the electrical zones are indicated on the right. Zone I is a highly permeable zone of hydrothermal circulation. Zone II is a zone of active intrusion and magma accumulation. Zone IV has a low melt concentration (0.5 - 15 per cent) and may represent the top of a mantle diapir. From Thayer et al (1981).

Several authors have studies dispersion of seismic surface waves generated by earthquakes on and near the Gibbs and Jan Mayen fracture zones SW and NNE of Iceland, respectively, and recorded by the WWSSN broadband station at Akureyri (AKU). The waves travel along paths nearly parallel to the Reykjanes and Kolbeinsey ridges, respectively. The models derived (extending down to ~ 100 km depth) reveal a lithospheric thickening with crustal age back to around 40 m.y. They are all fairly similar implying fast thickening the first few million years after crustal creation perhaps up to 20 m.y. (Evans & Sacks, 1980) but more slowly thereafter to some 80-100 km, which is the thickness typical of a standard oceanic lithosphere (see Fig. 5.9). Immediately beneath the lithosphere a low velocity layer was found with slightly increasing velocity with crustal age (Evans & Sacks, 1979, 1980). In general these results are in good agreement with lithospheric structures found in other young oceanic regions both by surface wave studies (Leeds et al, 1974; Forsyth, 1977) and thermal modelling of ocean ridges (Parker & Oldenburg, 1973). Jacoby and Girardin (1980) suggested an additional and interesting feature to former structural models for the Reykjanes Ridge. Additional constraints on their models in view of recent information from the RRISP project (Gebrande et al, 1980) enabled them to interpret the surface wave dispersion data to indicate a lithospheric low velocity zone between 20 and 30 km depth. This zone appears at some distance from the ridge axis and may then decay again towards older structures.

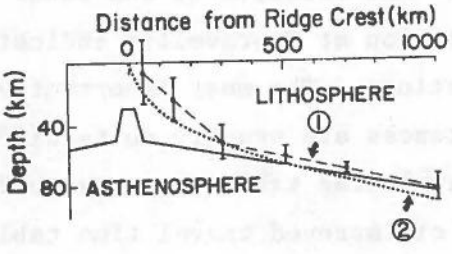

Fig. 5.9 Some models of the Reykjanes Ridge. Both Model 1 (Leeds et al, 1974), where the vertical bars are the error limits, and the model shown solid (Keen et al, 1980) are derived from surface wave studies. Model 2 is Parker and Oldenburg's (1973) model based on thermal studies. From Keen et al (1980).

Recent surface wave studies (Stefanson and Halldorsson, 1980, unpublished), comparison of phase velocities recorded in Reykjavik (REY) and Akureyri (AKU), indicate a low velocity layer beneath Iceland with top at about 60 km depth (see Fig. 4.2). This might indicate a mean lithospheric thickness beneath Iceland to be around 60 km and thus somewhat thicker than young oceanic lithosphere proper.

Previous 'delay studies' of seismic body wave phases indicate an anomalous low velocity mantle beneath Iceland. Tryggvason (1964) compared delays (residuals) of P-waves (relative to JB-tables) recorded at stations in Reykjavik (Iceland), Kiruna (Sweden) and Scoresbysund (Greenland) from a great number of teleseismic earthquakes. After applying a crustal correction, P-onsets were observed 2-3 seconds later in Reykjavik than in Kiruna and Scoresbysund. On the other hand Stefansson (1967) noted the possibility of a 'hidden' first cycle in the P-wave train at Reykjavik due to extremely high microseismic level which might have contributed to these large delays. To avoid such possible misinterpretation of arrival times, it is necessary to compare the actual waveforms at different places in Iceland (see Chapter 2).

When distances between stations are large, errors in travel time tables and hypocenter parameters may become important. In a study of Long and Mitchell (1970) these errors (see below) were reduced to some 'minimum', but they evaluated relative teleseimsic P-wave delays between stations in Iceland (AKU and a temporary station at Hveravellir), Scotland (EKA), Sweden (KIR) and Greenland (KTG). The evaluated delays at AKU relative to the other stations were 1-2 seconds, and the temporary station at Hveravellir indicated little variation between the two Icelandic stations. The most important error sources are the following: as epicentral distances are usually quite different for any station pair, the accuracy of the travel time tables has a significant effect on the residuals. Thus with the use of improved travel time tables (Herrin, 1968), they considered this error to be negligible. A 25 km error in focal position produces maximum 0.8 seconds in relative delay for a pair of stations 15° apart. Presumably they obtained some reduction in this error term as most events were from the North Pacific but a systematic error (25 km north of true

epicenters) was previously found (Davies & McKenzie, 1969) in event location there. In turn this means only fractional azimuthal event coverage, mainly from north to northeast. Furthermore a single station data may give rise to large random errors although subtracting the average reduces systematic errors. However, as discussed earlier, reading and timing errors can be further reduced by comparing waveforms to 'nearby' stations.

Sipkin and Jordan (1975) measured the ScS phase arrivals at several WWSSN stations from 10 globally distributed deep-focus earthquakes as to compare the relative delays beneath various tectonic provinces of the earth. The ScS time obtained for AKU (only one reading) gave about 3 seconds delay compared to the average for normal oceans. This result also implies a P-residual of about 1-2 seconds.

5.3 Mantle Convection

The idea of convective flow in the mantle predates the plate tectonic hypothesis, although the observational basis for the latter is much better established. Anyway, the only mechanisms that easily can provide enough energy to break up plates and move them apart are convective flow driven by the difference in density between the hot fluid and the cold (e.g., McKenzie and Richter, 1976). Also, it has long been known that the Rayleigh number of the mantle is so large as to make thermal convection likely or with other words the radioactive heat of the earth's interior must be removed by convection (e.g., Tozer, 1972). But it is still an open question whether the convection cells are restricted to the upper mantle or involve the whole mantle.

An early, thorough treatment of mantle convection is due to McKenzie et al (1974), assuming two layers of convective eddies (cells) in the mantle. Later on McKenzie and Weiss (1975) suggested a relatively thin layer (100 km) of higher viscosity at about 700 km depth associated with phase transition, which would have the effect of separating any flow in the upper and lower mantle.

Necessary conditions for whole-mantle convection are fairly uniform viscosity throughout the mantle plus a thermal boundary layer at the bottom of the mantle (Elsasser et al, 1979). The opponents of whole-mantle convection assume that descending lithospheric slabs cannot penetrate below 720 km (Richter, 1979) in order to explain the seismic cutoff at that range together with increasing energy release and compressive nature of earthquakes below a depth of 500 km. They therefore assume a high rigidity of the lower mantle prohibiting whole-mantle convection. On the other hand, uplift data (Cathles, 1975; Peltier, 1976, 1980) indicate a quite uniform viscosity (10^{22} p) throughout the whole mantle with even slightly lower viscosity of the lower mantle. This is in good agreement with previously estimated viscosity of the mantle from observations on deceleration of the earth's rotation by tidal friction (Dicke, 1969). Davies (1977) showed that there needs to be extreme viscosity contrasts to significantly affect large-scale flow patterns. His results indicate that the lower mantle has to be 10^4 times more viscous than the upper mantle in order to confine thermal convection to the upper mantle. The large horizontal scale of the steady moving lithospheric plates is evidence for convection currents on a vast scale, most likely involving the whole mantle for the fastest plates (e.g., Davies, 1977). Laboratory studies indicate that there might be smaller currents as well (McKenzie and Richter, 1976), especially in the upper mantle. Elsasser et al (1979) showed convincingly the possibility of reconciling plate sizes and speeds, mantle viscosity, heat flow, plus some seismic data with whole-mantle convection. But because of the pronounced heterogeneities in the uppermost mantle down to roughly 250 km, it presumably differs quite a lot in mechanical and thermal behavior from the mantle farther down, especially in localized regions. Anyhow, if the viscosity of the mantle is more or less uniform (10^{22}p) as suggested by post-glacial rebound data, the existence of a second scale of convection in the upper mantle seems extremely unlikely (Yuen et al, 1981).

Recent numerical experiments on convection in chemically layered mantle (Christensen, 1981) implicate a slight preference for whole-mantle convection. Because the viscosity of the lower mantle can hardly be extremely high, a substantial chemical boundary (e.g., associated with the 650 km seismic

discontinuity) is necessary for providing two separate layers of convection in the upper and lower mantle. For chemical density difference of 10% ($\Delta\rho/\rho$ = 10%) two separate layers of convection would come into being. At the dividing line a huge thermal boundary layer developed as a result of the fact that 75% of the surface heat flux must pass this barrier by thermal conduction. No such thermal layer has been detected yet by its influence on seismic velocity or by drop in the Q-factor, η or σ (viscosity). On the other hand it seems possible that smaller lumps (< 10 km) of the heavy material can be torn off and transported to the surface by the fast-rising flow in the spreading axis, provided that the chemical boundary is only a few per cent.

To conclude this section, it seems likely that the whole mantle is involved in thermal conductive currents. Presumably the large fast-moving plates are driven by whole-mantle convection cells while those with slower rates and especially the smallest ones are subject to rather localized motions.

5.4 The Iceland Hot Spot

According to the initial hot spot hypothesis (Wilson, 1963; Morgan, 1971) hot spots are the sites of rising regions within the mantle, which also consistutes the world-wide accepted idea up to date. The source depth of this mantle upwelling is at least a few hundred kilometers, and possibly as deep as the core/ mantle boundary (see the preceding section). The following geophysical and geochemical evidence support the existence of a positive thermal anomaly (hot spot) under Iceland:

- chemical and morphological changes of the Mid-Atlantic Ridge towards Iceland;
- the Icelandic transverse ridge;
- the pronounced offset of the volcanic rift zones in Iceland relative to the Kolbeinsey and Reykjanes ridges;
- the change in strike of the extensional features across Central Iceland;
- the elevation of Iceland and the thickness of its oceanic crust together with gravity data;
- the decrease in intensity of volcanism along the volcanic rift zones away from south central Iceland.

Axial high instead of axial valley

It has long been recognized that slow-spreading ocean ridges normally exhibit axial valley while the fast-spreading ridges are characterized by an axial high (e.g., Davies & Lister, 1974; Sleep & Rosendahl, 1979). Therefore the slow-spreading Reykjanes Ridge (Talwani et al, 1971) south of Iceland, characterized by an axial high similar to that occurring along the East Pacific Rise, is an anomalous feature of the Mid-Atlantic Ridge system. To the north, this axial high rises until it actually protrudes above sea-level as Iceland, whereas to the south it gradually increases in depth and gives way to the normal axial valley type morphology typical of the Mid-Atlantic Ridge. As noted by Schilling (1973), this morphologic variation is coincident with a systematic variation in the chemistry of young basalts erupted along the ridge axis (Jakobsen, 1972); both of which suggest that the Reykjanes Ridge is under the influence of the 'hot spot' centered under Iceland (Vogt, 1974; Sigvaldsson et al, 1974). The rate of magma generation must be abnormally high under the island and decreases systematically along the ridge axis away from it (Sleep and Rosendahl, 1979; Vogt, 1979). Another important structural feature of mid-ocean ridges is the correlation between spreading rate and transform spacing. With increasing spreading rate the transform spacing increases. Assuming the magma chamber is wider along the Reykjanes Ridge than it is further south, one would expect the usual short-offset transform spacing of the Mid-Atlantic Ridge to be noticeably larger there, which is evidently the case (Nelson, 1981; Fox, 1980).

The Icelandic transverse ridge

The aseismic Greenland-Iceland-Faeroes Ridge, also called the Icelandic transverse ridge, appears to be the trace of a hot spot contributing to the opening of the North Atlantic the past 60 m.y. according to Eldholm and Talwani (1977). Similarities between Iceland and its transverse ridge, setting it apart from typical North Atlantic Ocean floor areas (Bott, 1974; Schilling & Nygaard, 1974; Detrick et al, 1977), include large crustal thickness, geochemical features, poor development of magnetic lineations, and the occurrence of a number of central volcanoes, inferred from localized gravity and magnetic anomalies of several kilometer extent. This transverse ridge matures from ~ 10 km thick crust of Iceland to approximately 32 km beneath the Iceland-Fareoes Ridge.

There is some evidence from DSDP data, site 336 on the Iceland-Fareoes Ridge (Talwani et al, 1976; Luyendyk et al, 1979) that the ridge has been emergent for considerable time after it was formed. Presumably the ridge did not sink below sea level until after the westward shift in the spreading center north of Iceland around anomaly 7 ~ 27(30) m.y. ago (Talwani & Eldholm, 1977). The anomalously shallow depth of the Iceland-Fareoes Ridge present is in good agreement with predicted subsidence by a simple $t^{\frac{1}{2}}$ subsidence law (Parsons & Sclater, 1977), provided it has been emergent until 27(30) m.y. ago (Detrick et al, 1977). Ward (1971) proposed the idea of Iceland formed by a large volume of lava extruded from a broad fracture zone, particularly when the fracture zone was undergoing distortion as the center of spreading shifted (just quoted). Menard and Atwater (1969) called such a fracture zone 'leaky' and proposed that topographic (aseismic) ridges parallel to the main trend of the fracture zone can form in such a 'leaky' zone. By this hypothesis the huge land mass of Iceland compared to other mid-ocean islands (e.g., Jan Mayen) is mainly due to a greater number of fracture zones near Iceland (prior to the change in spreading) spanning over a wider range of latitude than elsewhere. This hypothesis therefore implies that Iceland is not necessarily as anomalous as commonly postulated.

Morgan (1971,1972) in his hot spot hypothesis, suggested a transverse ridge to be a continuous trace of a narrow plume rising from the lower mantle. However there is evidence suggesting that there has not always been only a comparatively narrow plume building up the Icelandic transverse ridge (Bott, 1974). The fact of the contemporaneous and wide extent of the early Tertiary volcanism supports the idea that convective overturn (large convective cells) occurred this time. The apparent decay in the intensity of the hot spot indicated by crustal thickness variation along the transverse ridge agrees with this hypothesis (Bott, 1974; Bott & Gunnarsson, 1980). The abrupt change in the pole of rotation roughly 30 m.y. ago and simultaneous focusing of the upwelling material probably occurred as a result of a change in global convective pattern. Most likely Iceland was created due to these changes.

Migration of the volcanic rift zones

Recent geological and geophysical evidence indicates that the volcanic rift zones have shifted during the geological history of Iceland between two or

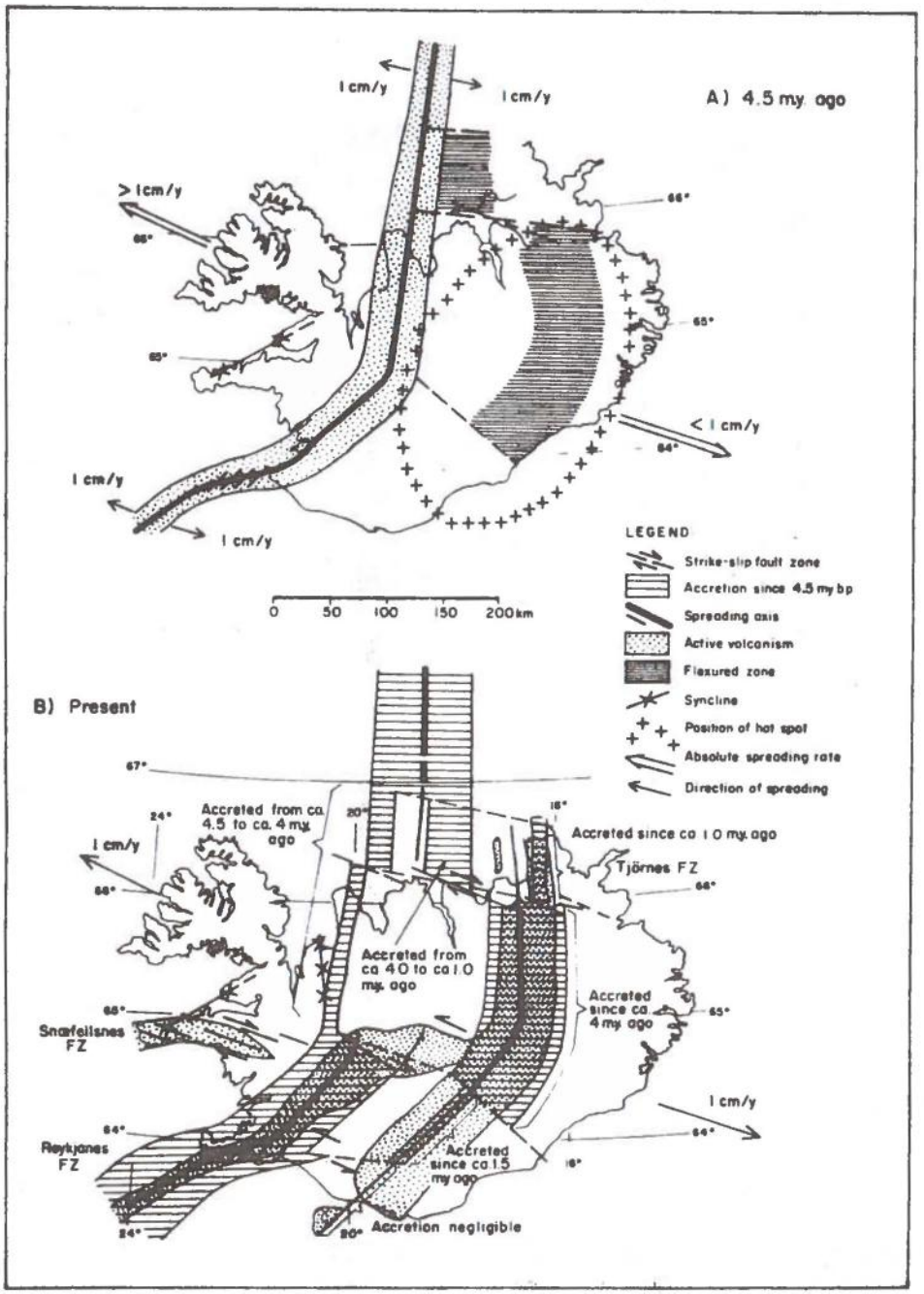

Fig. 5.10 A hypothetical development of the volcanic rift zones in Iceland.

A. Reconstruction of the rifting zones in Iceland before the eastward shift in northern Iceland ~ 4 m.y. ago.

B. The present pattern of the volcanic rift zones in Iceland. The reconstruction south of 65°N is based on the hypothesis that the eastern spreading axis in southern Iceland became active only 1.5 m.y. ago together with the diminishing rate of spreading and accretion of the western axis (Hengill-Langjökull) since that time. Evidence for the termination of the spreading axis in southeastern Iceland at about 64°N by a transverse fault is discussed in Thorarinsson et al (1973). From Sæmundsson (1974).

more zones (Ward, 1971; Sæmundsson, 1974; Palmason & Sæmundsson, 1974; Johannesson, 1980). The evidence comes from stratigraphic and structural studies (e.g., Walker, 1960; Bödvarsson & Walker, 1964; Sæmundsson, 1967) and from heat flow data (Palmason, 1973; Palmason et al, 1980).

Available K-Ar ages and paleomagnetic data (see Palmasson & Sæmundsson, 1974) indicate a hiatus in the stratigraphic succession in eastern Iceland between ~ 8 and ~ 4 m.y. ago. This hiatus may be correlated with a major eastward shift of the volcanic rift zones and probably a development of fracture zones as well.

Prior to 4 m.y. ago a volcanic zone existed between Langjökull and Skagi 150 km west of currently active rift zone in northern Iceland (see Fig. 5.10). The present-day active rift zone in northern Iceland opened up ~ 4 m.y. ago, but its southwestward continuation 2.5 m.y. later.

If one accepts this 150 km eastward jump or shift of an active rift zone, it is reasonable to relate it to the dimensions of the hot spot under Iceland. The hypothesis assumes the accreting plate margins in the Iceland region to move west-northwest relative to the more or less stationary hot spot. This can explain the shift of a ridge segment to a new position above the hot spot and east of the formerly active zone.

Triple-armed rift pattern

Hot spots or plumes are supposed to uplift the overlying lithosphere and cause a radial stress field. Ideally the lithosphere should break up along three major rift zones forming angles of about 120° with each other. This holds for several intraplate volcanoes, e.g., most Hawaiian volcanoes have these three principal rift arms (Wyss, 1980).

However, for tectonically active areas, those near plate margins, the regional tectonic stress field interferes with the plume generated radial stress field. Such superposition of stress fields can drastically alter the dike orientation from radial (Muller and Pollard, 1977). Einarsson et al (1977) found focal

Fig. 5.11 Map of Iceland and Mid-Atlantic rift system and 1000-m depth contour (After Sigurdsson, 1970). Shaded areas represent the neo-volcanic zones with focal mechanism from Einarsson et al (1977). The approximate location of the plume center and its conjectured three rift arms are sketched in. It is postulated that the actual trend of two of the arms (dashed) is due to the dominance of extensional stress field perpendicular to the Mid-Atlantic spreading axis. From Wyss (1980).

mechanism in the Borgarfjördur area which indicated NS extension (Fig. 5.11), which in turn suggests a plume-related origin of the Snaefellsnes volcanic zone. This observation strongly supports the idea that the Snaefellsnes volcanic zone is the third plume-generated rift arm (Wyss, 1980). The plume center, which coincides with geochemical data (Sigvaldason et al, 1974; Zindler et al, 1979; Rowe & Schilling, 1979), and its conjectured three principal rift arms are sketched on Fig. 5.11. This hypothesis assumes that the extensional stress field perpendicular to the Reykjanes Ridge caused the arm that should have trended SE to turn into SW direction so that intrusive dikes opened against least compressive stress. Accordingly, the present-day rift-arm orientation suggests that regional tectonic stress field due to the Mid-Atlantic Ridge dominates over the plume-induced stress field.

Gravity and topographic data

Anderson et al (1973) discovered a common feature for all hot spots, namely, that the free-air gravity anomaly over a rising region (hot spot) was always positive. Over a rising current the surface of the earth is elevated, owing to the dynamic effect of the flow, thereby causing a positive gravity anomaly. For a convecting fluid with a uniform viscosity, McKenzie et al (1974) have shown that the net gravity anomaly will be positive over an upwelling region, in spite of the higher temperature and lower density there.

Gravity surveys (Einarsson, 1954; Bott et al, 1971; Bott & Gunnarsson, 1980) indicate that Iceland is isostatically compensated as the free-air gravity anomalies are close to zero at the margin of the island and increase to a regional average of only +20 mgal over its interior.

Cochran and Talwani (1977,1978) examined the correlation between depth and free-air gravity anomalies in the North Atlantic Ocean. Taking into account the normal thermal subsidence of the oceanic lithosphere with age, they removed the depth-age related gravity effect (Parsons & Sclater, 1977; Sclater et al, 1971; Sclater and Francheteau 1970) from the observed free-air gravity anomalies, thereby allowing the residual anomalies due to other causes to be examined. They concluded that the overall elevation of the anomalous ridge north of 30°N must be maintained by a huge mass deficiency deep in the asthenosphere. An increase in temperature of about 75° can explain such mass deficit (Cochran & Talwani, 1978). On the other hand, the compensation for more local features, such as the topographic highs surrounding Iceland and the Azores, occurs at shallower depths (within the lithosphere). Thus the gravity data enabled them to establish the presence of a very large upper mantle hot spot that might be associated with the broad overall compensation of the entire North Atlantic north of 30°N.

The gravity effect of the mass deficiency needed in the mantle to compensate for the topographic high compared to the 'normal' Atlantic ocean basin has recently (Hermance, 1981) been reestimated. Previously estimated values values for this gravity effect were in the range -140 to -250 mgal whereas

Hermance's estimation is ~ -430 mgal, assuming the same density (2.9 g/cm^3) for both Icelandic crust (10 km thick) and the normal oceanic crust (7 km thick).

The characteristics of Icelandic volancism

The volcanic activity in Iceland during historical time is a direct continuation of the prehistoric Post-glacial activity and is confined to almost the same areas (Fig. 5.12), within the neovolcanic zones (Thorarinsson & Saemundsson, 1979). It is estimated that about 30 volcanoes have been active in historical times, and about 200 during postglacial time (Thorarinsson, 1965). Two main types of volcanoes have been active: purely basaltic ones and central volcanoes producing intermediate and acid rocks besides basalt. Approximately 90% of Iceland above sea level is made up of volcanic rocks (~ 80% basaltic), only ~ 10% being consolidated sediments.

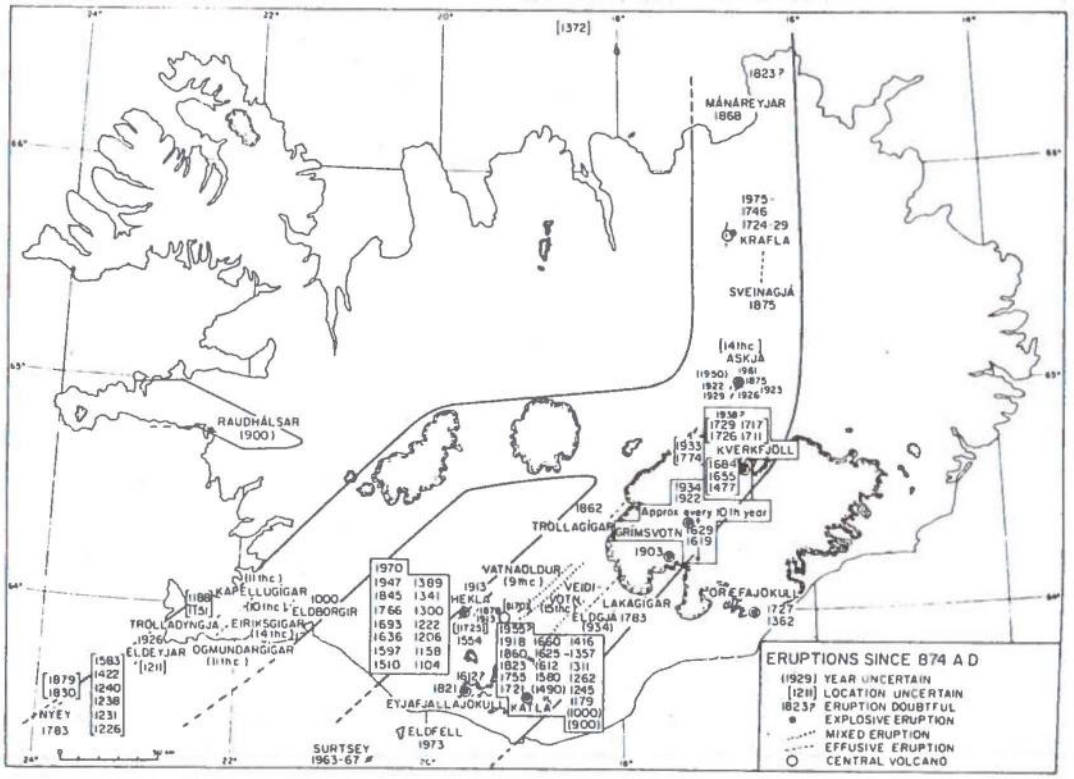

Fig. 5.12 Volcanic activity in Iceland in historical time. From Thorarinsson & Sæmundsson (1979).

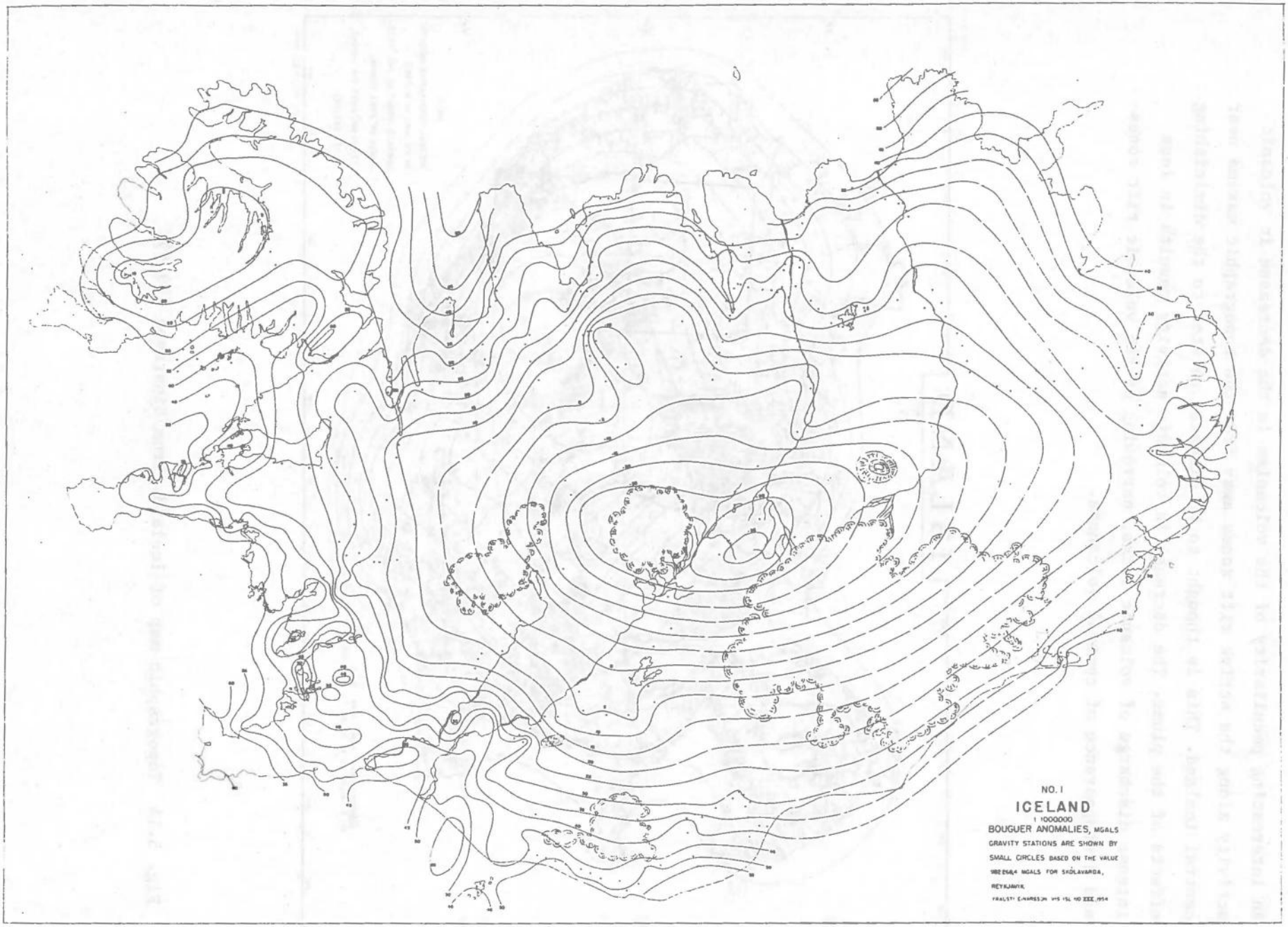

Fig. 5.13 Bouger-anomaly map of Iceland. From Einarsson (1954).

An interesting peculiarity of the volcanism is the decreasae in volcanic activity along the active rift zones away from the topographic maxima near central iceland. This is thought to be directly related to the diminishing effects of the plume. The decrease in volcanic activity results in less intense discharge of volcanic rocks, narrowing of the volcanic rift zones and disappearance of central volcanoes.

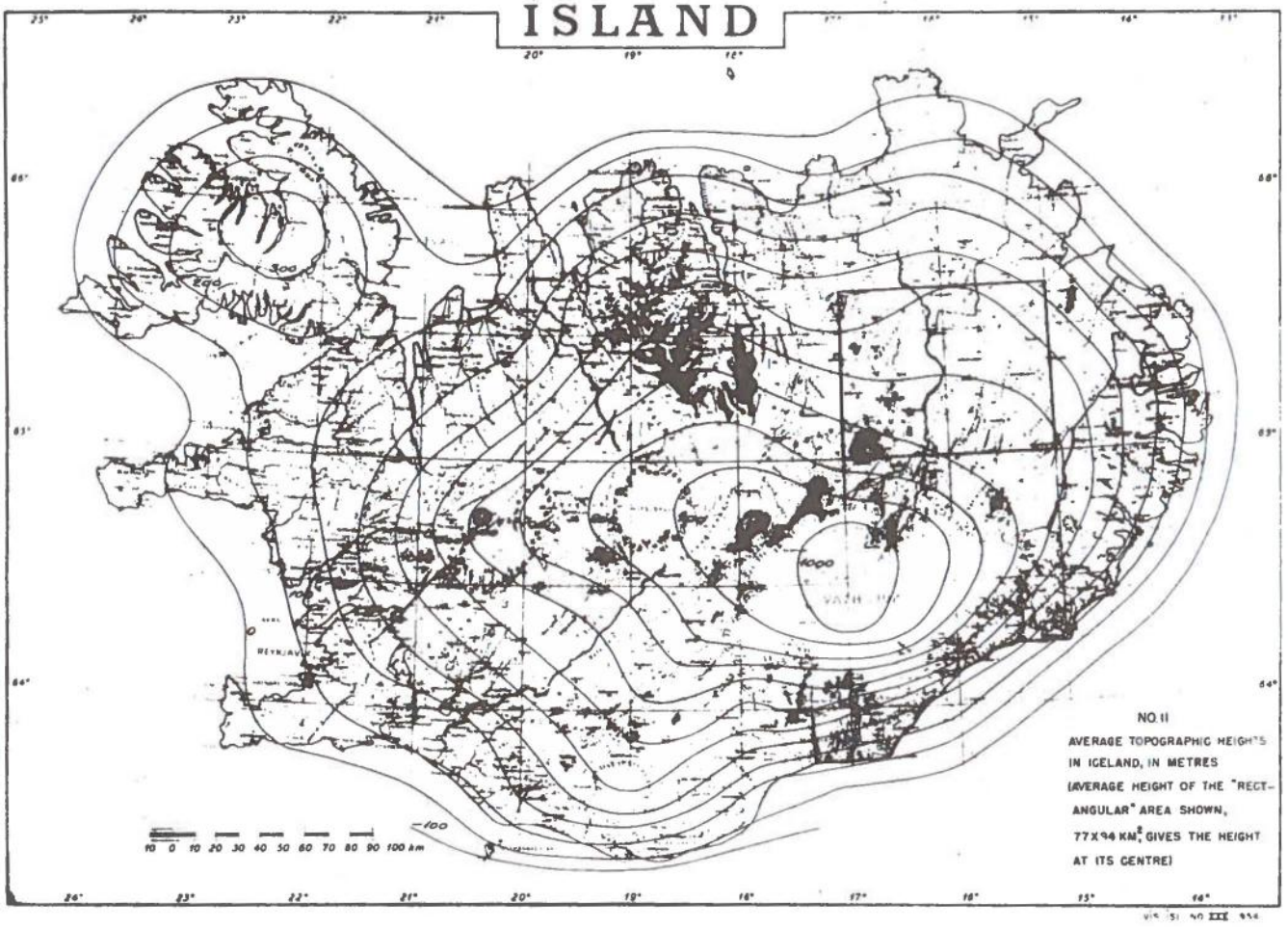

Fig. 5.14 Topographic map of Iceland. From Einarsson (1954).

To summarize, several geophysical and geochemical investigations lead to the same localization of the plume center, just southeast for central Iceland (see Fig. 5.11). The main implications for this are: (a) away from the presumed center the intensity in volcanic activity together with maximum content of potassium rare earth and minor elements in basalts on the volcanic rift zones decreases continuously with distance; (b) the center of the gravity low (Fig. 5.13) which matches also the topographically highest part of the country (Fig. 5.14) coincides with this area; and (c) the trend of linear tectonic features alludes to this location as well.

6. INTERPRETATION

There are two main factors restricting the size of inhomogeneities observable by 3-D seismic mapping using teleseismic P-waves. Firstly, incomplete data base, i.e., bad station coverage and/or insufficient event Az./dist. coverage. Secondly, teleseismic waves are of long wavelengths (2-10 km) and therefore not applicable on small-scale inhomogeneities, so even with perfect data base the scale length of observable anomalies would not become lower than of the order of 10 km. Anyway, the relation between P-velocity and gravity will be discussed and possible contribution to the gravity field as inferred from the observed P velocity anomalies. Also a rough quantitative estimate of the temperature influence on P-velocity will be given and correlation between heat flow and lateral P-velocity variations examined thereby.

6.1 On the Velocity-Density Relation and inferred Correlation with Gravity thereby

The establishment of the upper mantle compressional velocity anomalies beneath Iceland leads us to the primary question of their origin. Birch (1961) found empirically a linear relation between velocity and density anomalies for a great variety of crustal rocks. He used laboratory observations of P velocity at 10 kbar to ensure that the pores had collapsed so that the relationship $\Delta v_p = \alpha \Delta \rho$ would be valid beneath a few kilometers depth. The proportionality constant α has an average value of 3.3 km/s/g/cm^3 corresponding to a mean atomic weight of approximately m=21. For example, the transition between eclogite and garnet-granulite follows Birch's density-velocity relation. Just note in passing that the density anomalies originate from lateral variation in the temperature and/or chemical inhomogeneities. For most of the common mantle minerals α is also positive and not greatly different in magnitude if changes in velocity and density are related to differences in temperature (Anderson et al, 1968). In general the density contrast is somewhat less than expected for Birch's law when the density-velocity relation is purely due to temperature effect. On the other hand, differences in chemical and mineralogical composition may

cause negative α for example by nonisomorphic substitution or by substitution of a lighter element in a crystal structure by a heavier one (phase transition). Finally, the case of partial melts gives a wide range of velocity-density relations depending on the shape of melt (Aki, 1981). If the melt exists in pores of more or less spherical shape, the density contrast which is calculated by the formula of Sato (1952) can be significant and the resultant velocity-density relation becomes similar to the case of pure temperature effect. On the other hand, if the melt is constrained in thin cracks or grain boundaries, the density contrast becomes very small. Thus, if Birch's law is applied to the observed velocity anomaly a maximum estimate of the density contrast is obtained. Anyway, depending on the cause of a velocity anomaly, geophysical observations indicate either positive or negative correlation with the density in crust and upper mantle except for the case of partial melt in nonspherical pores. Thus, assuming proportionality of density and velocity perturbations, a relation between gravity and velocity anomalies should be visible as well.

As discussed in section 5.4 Cochran and Talwani (1978) found correlation between depth of compensation for topographic highs of different circumference and the free-air gravity anomalies in the North Atlantic Ocean. Thus the overall positive Bouguer gravity anomaly (up to +350 mgal) for the whole N. Atlantic region might have its counterpart of relatively light material in the lower mantle (possibly related with large-scale mantle convection) while the relative low observed at the Iceland region (Fig. 5.13) most likely originates from heterogeneities (low density regions) within the uppermost mantle.

Under the assumption of linearity between Δv_p and $\Delta\rho$ we may almost preclude the observed velocity anomalies of layers 2-4 as contributors to the observed gravity low due to the overwhelming effect of the inverse square proportionality with distance. Applying

$$\frac{\Delta v_p}{\Delta\rho} = \alpha = 3.3$$

on the low in layer 4 yields $\Delta\rho \sim 0.1$ g/cm^3 (for 4% velocity contrast) and calculating the gravity effect of a sphere at 300 km depth, with radius 50 km and 0.1 g/cm^3 density deviation yields only $\Delta g \sim 4$ mgal. Accordingly the absence of significantly strong velocity lows of sufficiently large extension in the intermediate layers also precludes any significant gravity effect. Thus the gravity low should practically be subject solely to the velocity low in the uppermost layer.

6.2 Layer 1

Correlation with gravity

Consider first the gravity map (Fig. 5.13) and note the variation in spacing of the isolines, especially the relatively large isoline spacing to the west from central Iceland and the NNE along the volcanic zone in NE Iceland. Compared to the velocity anomaly map (Fig. 4.7a; Appendix B) the match is essentially good. For example, the EW elongation of both the velocity and gravitational lows of Central Iceland together with the simultaneous increase in velocity and grvity away from Central Iceland, except for the SW and NNE directions incorporating parts of the neovolcanic zones. The density contrast inferred from the observed velocity anomalies by using Birch's law should cause more negative gravity anomalies than actually observed for these areas. This situation may correspond to the case of partial melt in nonspherical pores which gives small density contrast compared to that for Birch's law.

Correlation with Heat Flow and Main Tectonic Units

The neovolcanic zones constitute the areas of highest heat flow as evidenced by several high temperature steam fields. In view of this the main velocity low correlates with the most vigorous parts of the neovolcanic zones except for the Reykjanes Peninsula. Whereas outside the neovolcanic zones the velocity low covers entirely Quarternary and late Tertiary areas, the velocity highs correlate with the oldest regions with relatively low heat flow.

Considering the change in P velocity accounted for by temperature alone (Christensen, 1979), the estimate for basaltic rocks is:

$$\frac{\partial v_p}{\partial T} = -2.5 \cdot 10^{-4} \text{ kms}^{-1} \text{ }^{\circ}\text{C}^{-1}$$

for the temperature range 25-500°C.

The observed lateral P-velocity change of 3-5% may therefore be explained by a thermal gradient difference of averagely 32°C km^{-1}, provided a linear extrapolation of prescribed velocity-temperature relationship and a constant thermal gradient for the 75 km thick uppermost layer. However, it is very difficult to compare the heat flow map (Fig. 5.3) with the velocity anomaly map (Fig. 4.7a) because of the relatively large scatter in heat flow values. It must be taken into account that the seawater percolation and the groundwater circulation can greatly affect the thermal gradient, e.g., the highest values in Eastern Iceland are presumably too high due to hot groundwater effects. Anyway, geotherms of average 50-60°C km^{-1} are found both in the NW and SE, which compared to the geotherms of average 70-80°C km^{-1} west of the neovolcanic zone in NE Iceland show remarkable correlation with the velocity anomalies for these areas.

6.3 Layers 2 and 3

The anomalies in these two layers are much smaller than those in layer 1, which correlates with currently accepted views of generally more homogeneous material immediately beneath the lithosphere due to lower strength. Compared to layer 1 the low in layer 2 has shifted to the east. It is tempting to explain this eastward shift in terms of presumed westward drift of the plate margins. The low immediately south of the Tjørnes Fracture Zone in layer 3 correlates well with previous delay studies (discussed in section 5.2) where the AKU seismograph station's registrations of events from northward direction were used (Long & Mitchell, 1970; Sipkin and Jordan, 1975). The weak low covering central to SW Iceland in layer 3 may be explained as the top of the strong low observed in layer 4 (see below) when compared to the models of 300 km depth range, S_{300}, N_{300} (see Appendix B). Significant highs are found under the crust of 10-20 million years in age for layers 2 and 3.

6.4 Layer 4

A remarkable low is observed in this layer with maximum anomaly covering central Iceland tapering off within a radius of 60 km. This low may be related to relatively strong thermal anomaly or a mantle plume. As discussed earlier such plumes may originate from the core/mantle boundary, but they do not necessarily have to be continuous anomaly the whole way down. If there exists a sufficient chemical boundary between upper and lower mantle two separate layers of convection must develope, but comparatively small lumps can be torn off from the lower mantle and transported to the surface, provided that the chemical density difference is less than 3-4% (Christensen, 1981).

It is clear that an inhomogeneity with a significant density contrast cannot be in equilibrium and must therefore be moving. Actually we can calculate how fast an inhomogeneity moves by using Stoke's law. If we assume that the inhomogeneity is a sphere falling in a viscous fluid under the grvitational force the solution is:

$$V = \frac{2g\ r^2\ \Delta\rho}{9\eta}$$

The velocity V of the sphere is proportional to the gravitational acceleration g, square of the radius r of the sphere, the density difference $\Delta\rho$ between the sphere and fluid, and inversely proportional to the viscosity η of fluid. The radius r of the inhomogeneity in layer 4 is about 50 km (see Fig. 4.7d and Appendix B), and the density contrast $\Delta\rho$ is about 0.1 g/cm^3 where Birch's law has been applied on 4% velocity contrast. Recent estimates of the viscosity under Japan give about 10^{20} poise (see Aki, 1981). Applying 10^{20} poise for the viscosity η under Iceland, we obtain V=1.7 m/year. This gives a maximum estimate for the velocity of the asthenospheric upwelling below Iceland because Birch's law obeys a maximum density contrast inferred from the observed velocity low. Our maximum estimate of 1.7 m/year (only 0.2 m/year if the viscosity is 10^{21}) is comparable to that suggested by Morgan (1971), namely, 2 m/year for the plume velocity when he proposed the mantle plume as the driving force of plate tectonics.

A consistent feature between layers 2-4 are the highs around the country so far they are significant, but the region beneath the eastern flank of the Reykjanes Ridge show a slight preference for a low velocity 'band' along the ridge. On the other hand, the region underneath the Kolbeinsey Ridge has more or less positive anomalies in layers 2-4. It may be that the pulling apart mechanism of the plate motions causes negative anomalies in the uppermost 50 to 100 km below spreading ridges. On the other hand the deep extent of significant negative anomalies beneath Iceland indicate an interior origin (plume) rather than effects from the complicated, interactive mechanism of plate motions. In a recent paper of Anderson (1981) the plume was supposed to originate from the LVZ immediately beneath the lithosphere. This is clearly contradictory to our results, indicating a plume of at least deeper origin than that of LVZ.

7. CONCLUSIONS

The model explains about 0.1 s (18.2%) of the residuals leaving around 0.4 s unexplained almost as random errors as the model turned out to be quite linear (see section 4.4). We have identified significant anomalies with good resolution in four depth ranges. In the uppermost 75 km not unexpectedly the young volcanic zone in NE Iceland coincides with the minimum of the observed velocity low. There is a correlation between the observed gravity anomalies and observed velocity anomalies for the uppermost layer in the sense that both increase away from Central Iceland except for the velocity anomaly along the neovolcanic zone in NE Iceland. The discrepancy between the gravity map and the observed P velocity low covering the volcanic zone in NE Iceland implies that Birch's law is not applicable on the anomaly there, which presumably corresponds to partial fusion under the area. Addtionally, outside the neovolcanic zones the velocity anomalies seem to correlate with the observed thermal gradient variation. The deeper anomalies, at 75-275 km depth, are much smaller which agrees with the currently accepted view that the material immediately beneath the lithosphere is relatively homogeneous. Further down, 275-375 km, the structures are quite inhomogeneous. The strong low coinciding with central Iceland may be related with an upwelling mantle material, perhaps a mantle plume of deep origin.

We made a rough estimate of the asthenospheric upwelling velocity based on the size of inhomogeneity and density contrast inferred from the velocity low in layer 4. If the velocity anomaly is due to any effect which obeys Birch's law, the flow is quite rapid, but however somewhat less than that of Morgan's plume driving the plate motion. On the other hand, if partial fusion in thin cracks or grain boundaries is the effect causing the velocity anomaly, the flow is negligible corresponding to plates driven slowly by the ridge-push and slab-pull. In conclusion, our results suggest the possibility of a vigorous plume under Iceland, if Birch's law is applicable to the observed velocity anomaly.

EUREKA!

A bit tired after the successful 'earth-interior trip', which is considered the up-to-date bravest attempt to objectively test geophysical results. By the way, I found no remains from Jules Verne's voyage.

8. REFERENCES

Aki, K., 1981: 3-D seismic inhomogeneities in lithosphere and asthenophere: evidence for decoupling in lithosphere and flow in asthenosphere, m/s in preparation.

Aki, K., A. Christoffersson & E.S. Husebye, 1977: Determination of the three-dimensional seismic structure of the lithosphere, J. Geophys. Res., 82, 277-296.

Aki, K. & P.G. Richards, 1980: Quantitative Seismology, Theory and Methods. W.H. Freeman & Company, San Francisco.

Anderson, D.L., 1981: Hotspots, basalts and the evolution of the mantle. Science, 213, 82-89.

Anderson, O.L., E. Schreiber, R.C. Liebermann & N. Soga, 1968: Some elastic constant data on minerals relevant to geophysics. Rev. Geophys. Space Phys., 6, 491-524.

Anderson, R.N., D. McKenzie & J.G. Sclater, 1973: Gravity, bathymetry and convection in the earth. Earth Planet. Sci. Lett., 18, 391-407.

Båth, M., 1960: Crustal structure of Iceland. J. Geophys. Res., 65, 1793-1807.

Birch, F., 1961: The velocity of compressional waves in rocks to 10 kilobars, 2, f. Geophys. Res., 66, 2199-2224.

Bödvarsson, G. & G.P.L. Walker, 1964: Crustal drift in Iceland. Geophys. J.R. astr. Soc., 8, 285-300.

Bott, M.H.P., C.W.A. Browitt & A.P. Stacey, 1971: The deep structure of the Iceland-Faeroe ridge. Mar. Geophys. Res., 1, 328-351.

Bott, M.H.P., 1974: Deep structure, evolution and origin of the Icelandic Transverse Ridge. In Kristjansson (ed): Geodynamics of Iceland and the North Atlantic Area, D., Hingham Mass., 33-47.

Bott, M.H.P. & K. Gunnarsson, 1980: Crustal structure of the Iceland-Faeroe Ridge. J. Geophys., 47, 221-227.

Bullen, K.E., 1937: The ellipticity correction to travel-times of P and S earthquake waves. Mon. Not. R. Astr. Soc., Geophys. Suppl., 43, 143-157.

Bullen, K.E., 1963: An Introduction to the Theory of Seismology. Cambridge University Press.

Cathles, L.M., 1975: The Viscosity of the Earth's Mantle. Princeton Univ. Press, Princeton, N.J.

Christensen, U., 1981. Numerical experiments on convection in a chemically layered mantle. J. Geophys., 49, 82-84.

Christoffersson, A. & E.S. Husebye, 1979: On three-dimensional inversion of P wave time residuals: Option for geological modelling. J. Geophys. Res., 84, 6168-6176.

Cochran, J.R. & M. Talwani, 1977: Free air gravity anomalies in the world's oceans and their relationship to residual elevation. Geophys. J.R. astr. Soc., 50, 495-552.

Cochran, J.R. & M. Talwani, 1978: Gravity anomalies, regional elevation, and the deep structure of the North Atlantic. J. Geophys. Res., 83, 4907-4924.

Davies, D. & D.P. McKenzie, 1969: Seismic travel time residuals and plates. Geophys. J.R. astr. Soc., 18, 51-63.

Davies, E.E. & C.R.B. Lister, 1974: Fundamentals of ridge crest topography. Earth Planet. Sci. Lett., 21, 405-413.

Davies, G.F., 1977: Whole-mantle convection and plate tectonics. Geophys. J.R. astr. Soc., 49, 459-486.

Detrick, R.S., J.G. Sclater & J. Thiede, 1977: The subsidence of aseismic ridges. Earth Planet. Sci. Lett., 34, 185-196.

Dicke, G.F., 1969: The average acceleration of the earth' rotation and the viscosity of the deep mantle. J. Geophys. Res., 74, 5895-5902.

Dziewonski, A.M. & O.L. Anderson, 1981: Preliminary reference earth model. Phys. Earth Planet. Inter., in press.

Dziewonski, A.M. & G. Freeman, 1976: The effect of small, aspherical perturbations on travel times and a re-examination of the corrections for ellipticity. Geophys. J.R. astr. Soc., 44, 7-17.

Einarsson, P., F.W. Klein & S. Björnsson, 1977: The Borgarfjördur earthquakes of 1974 in west Iceland. Bull. Seism. Soc. Am., 67, 187.

Einarsson, P., 1979: Seismicity and earthquake focal mechanism along the mid-Atlantic plate boundary between Iceland and the Azores. Tectonophysics, 55, 127-153.

Einarasson, P. & S. Björnsson, 1979: Earthquakes in Iceland. Jökull 29, 37-43.

Einarsson, T., 1954: A survey of gravity in Iceland. Soc. Sci. Islandica XXX.

Elsasser, W.M., P. Oslon & B.D. Marsh, 1979: The depth of mantle convection. J. Geophys. Res., 84, 147-155.

Ellsworth, W.L., 1977: Three-dimensional structure of the crust and upper mantle beneath the island of Hawaii. Ph.D. Thesis, 327 pp., Mass. Inst. of Technology, Cambridge, Mass.

Evans, J.R. & I.S. Sacks, 1979: Deep structure of the Iceland Plateau. J. Geophys. Res., 84, 6859-6866.

Evans, J.R. & I.S. Sacks, 1980: Lithospheric structure in the North Atlantic from observations of Love and Rayleigh waves. J. Geophys. Res., 85, 7175-7182.

Flovenz, O.G., 1980: Seismic structure of the Icelandic crust above layer three and the relation between body wave velocity and the alteration of the basaltic crust. J. Geophys., 47, 211-220.

Fox, P., F. Schroeder, R. Moody, W. Pitman & P. Hoose, 1981: The Oceanographer Fracture Zone: morphology and evolution of structure at a slowly accreting plate boundary. Mar. Geophys. Res., in press.

Franklin, J.N., 1970: Well-posed stochastic extension of ill-posed linear problems. J. Math. Analysis Applic., 31, 682-716.

Gebrande, H., H. Miller & P. Einarsson, 1980: Seismic structure of Iceland along RRISP - Profile I. J. Geophys., 47, 239-249.

Gibson, I.L., et al, 1979: Crust of oceanic affinity in Iceland. The Iceland Research Drilling Project. Nature, 281, 347-351.

Goldflam, P., W. Weigel & B.D. Loncarevic, 1980: Seismic structure along RRISP - Profile I on the southeast flank of the Reykjanes Ridge. J. Geophys., 47, 250-260.

Haimson, B.C., 1979: New stress measurements in Iceland reenforce previous hydrofracturing results. σ H max is perpendicular to the axial rift zones. Abstract.

Hermance, J.F., 1981: Gravity compensation in the mantle beneath the neovolcanic zone of Iceland. Earth Planet. Sci. Lett., 54, 157-166.

Herrin, E., 1968: Seismological tables for P phases. Bull. Seism. Soc. Am., 58, 1193-1242.

Hovland, J., 1980: Inversion of P-wave travel time residuals to map lateral velocity anomalies in the upper mantle under central Europe. Cand. real thesis, 101 pp., University of Oslo.

Hovland, J., D. Gubbins & E.S. Husebye, 1981: Upper mantle heterogeneities beneath central Europe. Geophys. J.R. astr. Soc., 66, 261-284.

Jackson, D.D., 1972: Interpretation of inaccurate, insufficient and inconsistent data. Geophys. J.R. astr. Soc., 28, 97-109.

Jacobi, W.R. & N. Giradin, 1980: The evolution of the lithosphere at the southeast flank of Reykjanes Ridge from surface wave data. J. Geophys. 47, 271-277.

Jakobsson, S.P., 1972: Chemistry and distribution pattern of Recent basaltic rocks in Iceland. Lithos., 5, 365-386.

Jakobsson, S.P., 1979: Outline of the petrology of Iceland. Jökull, 29, 57-73.

Jeffreys, H. & K.E. Bullen, 1940: Seismological tables. Brit. Ass., Gray-Milne Trust, 50 pp.

Johannesson, H., 1980: Evolution of rift zones in western Iceland. Natturufrædingurinn, 50(1), 13-31.

Jordan, T.H., 1977: Lithospheric slab penetration into the lower mantle beneath the Sea of Okkotsk. J. Geophys., 43, 473-496.

Keen, C.E., A. Fricker, M.J. Keen & L. Blinn, 1980: Reykjanes Ridge crest studied by surface waves with an earthquake-pair technique. J. Geophys., 47, 265-270.

Klein, F.W., P. Einarsson & M. Wyss, 1977: The Reykjanes Peninsula, Iceland, earthquake swarm of September 1972 and its tectonic significance. J. Geophys. Res., 82, 865-888.

Lanczos, C., 1961: Linear Differential Operators. London: Van Nostrand.

Leeds, A., L. Knopoff & E. Kausel, 1974: Variations of upper-mantle structure under the Pacific Ocean. Science, 186, 141-143.

Levenberg, K., 1944: A method for the solution of certain non-linear problems in least squares. Quart. Appl. Math., 2, 162-168.

Long, R.E. & M.G. Mitchell, 1970: Teleseismic P-wave delay time in Iceland. Geophys. J.R. astr. Soc., 20, 41-48.

Luyendyk, B.P., A. Shor & J.R. Cann, 1979: General implications of the leg 49 drilling program for North Atlantic ocean geology. Initial reports of the deep sea drilling project, Vol. 49, No. 37, pp 825-839. Washington (U.S. Government Printing Office).

Marquardt, D.W., 1963: An algorithm for least squares estimation of non-linear parameters. J. Soc. Ind. Appl. Math., 11, 431-441.

Marquartdt, D.W., 1970: Generalized inverses, ridge regression, biased linear estimation and nonlinear estimation. Technometrics, 12, No. 3, 591-612.

McKenzie, D.P., J.M. Roberts & N.O. Weiss, 1974: Convection in the earth's mantle: Towards a numerical solution. J. Fluid Mech., 62, 465-538.

McKenzie, D.P. & N.O. Weiss, 1975. Speculations on the thermal and tectonic history of the earth. Geophys. J., 42, 131-174.

McKenzie, D.P. & F. Richter, 1976: Convection currents in the earth's mantle. Scientific Amer., 235, 72-89.

Menard, H.W. & T. Atwater, 1969: Origin of fracture zone topography. Nature, 222, 1037-1040.

Morgan, W.J., 1971: Convection plumes in the lower mantle. Nature, 230, 42-43.

Morgan, W.J., 1972: Deep mantle convection plumes and plate motions. Am. Assoc. Petr. Geol. Bull., 56, 203-213.

Muller, O.H. & D.D. Pollard, 1977: The stress state near Spanish Peaks, Colorado, determined from a dyke pattern. Pure Appl. Gephys., 115, 69.

Nelson, K.D., 1981: A simple thermal-mechanical model for mid-ocean ridge topographic variation. Geophys. J.R. astr. Soc., 65, 19-30.

Palmason, G., 1963: Seismic refraction investigation of the basalt lavas in northern and eastern Iceland. Jökull, 13, 39-60.

Palmason, G., 1971: Crustal structure of Iceland from explosion seismology. Soc. Sci. Isl. XL.

Palmason, G., 1973: Kinematics and heat flow in a volcanic rift zone, with application to Iceland. Geophys. J.R. astr. Soc., 33, 451-481.

Palmason, G., S. Arnorsson, I.B. Fridleifsson, H. Kristmundsdottir, K. Sæmundsson, V. Stefansson, B. Steingrimsson, J. Tomasson & L. Kristjansson, 1979: The Iceland crust: Evidence from drillhole data on structure and processes. In: Deep Drilling Results in the Atlantic Ocean: Ocean Crust (M. Talwani, C.G. Harrison & D.E. Hayes, eds.), Am. Geophys. Union, Maurice Ewing Series 2, 43-65.

Parker, R. & D. Oldenburg, 1973: Thermal model of ocean ridges. Nature Phys. Sci., 242, 137-139.

Parsons, B. & J.G. Sclater, 1977: An analysis of the variation of ocean floor bathymetry and heat flow with age. J. Geophys. Res., 82, 803-827.

Peltier, W.R., 1976: Glacial-isostatic adjustment, II; The inverse problem. Geophys. J., 46, 669-705.

Peltier, W.R., 1980: Mantle convection and viscosity, In: Physics of the Earth's Interior, Enrico Fermi International School of Physics, Course 78, (A. Dziewonski & E. Boschi, eds.), Elsevier, North Holland.

Richter, F.M., 1979: Focal mechanism and seismic energy release of deep and intermediate earthquakes in the Tonga-Kermadec Region and their bearing on the depth extent of mantle flow. J. Geophys. Res., 84, 6783-6795.

Ringdal, F., E.S. Husebye & J. Fyen, 1977: Earthquake detectability estimates for 478 globally distributed seismograph stations. Phys. Earth Planet. Inter., 15, P24-P32.

Rowe, E.C. & J.G. Schilling, 1979: Fluorine in Iceland and Reykjanes Ridge basalts. Nature, 279, 33-37.

Sato, Y., 1952: Velocity of elastic waves propagated in media with small holes. Bull. Earthq. Res. Inst., 30, 178-190.

Schilling, J.G., 1973. Iceland mantle plume: geochemical study of the Reykjanes Ridge. Nature, 242, 565-571.

Schilling, J.G. & A.N. Nygaard, 1974: Faeroe-Iceland plume: rare-earth evidence. Earth Planet. Sci. Lett., 24, 1-14.

Schultz, M.H., 1973: Spline Analysis, Prentice-Hall, Englewood Cliffs, New Jersey.

Sclater, J.G. & J. Francheteau, 1970: The implications of terrestrial heat flow observations on current tectonic and geophysical models of the crust and upper mantle of the earth. Geophys. J.R. astr. Soc., 20, 509-542.

Sclater, J.G., R.N. Anderson & M.C. Bell, 1971: The elevation of ridges and the evolution of the central eastern Pacific. J. Geophys. Res., 76, 7888-7915.

Sigvaldsson, G.E., S. Steinthorsson, N. Oskarsson & P. Imsland, 1974: Compositional variation in recent Icelandic tholeiites and the Kverkfjöll hot spot. Nature, 251, 579.

Sipkin, S.A. & T.H. Jordan, 1975: Lateral heterogeneity of the upper mantle determined from the travel times of ScS. J. Geophys. Res., 80, 1474-1484.

Sleep, N. & B. Rosendahl, 1979: Topography and tectonics of mid-ocean ridge axes. J. Geophys. Res., 84, 6831-6839.

Smith, M.L., D. Gubbins & B.R. Julian, 1979: Some notes on the method of travel time inversion developed by Smith, Gubbins and Julian. Internal NORSAR report.

Spudich, R. & J. Orcutt, 1980: A new look at the seismic velocity structure of the oceanic crust. Rev. Geophys. Space Phys., 18, 627-645.

Stefansson, R., 1967: Some problems of seismological studies on the Mid-Atlantic Ridge. In: Iceland and Mid-ocean Ridges, Report of a symposium, 80-89.

Sæmundsson, K., 1978: Fissure swarms and central volcanoes of the neovolcanic zones of Iceland. Geol. J. Spec. Iss. 10, 415-432.

Sæmundsson, K., 1974: Evolution of the axial rifting zone in northern Iceland and the Tjörnes Fracture Zone. Geol. Soc. Am. Bull., 85, 495-504.

Sæmundsson, K., 1967: An outline of the structure of SW-Iceland. In Iceland and Mid-ocean ridges (S. Björnsson, ed.), Soc. Sci. Islandica, 38, 151-161.

Talwani, M., V. Windisch & M. Langseth, 1971: Reykjanes Ridge crest: a detailed geophysical study. J. Geophys. Res., 76, 473-517.

Talwani, M. & O. Eldholm, 1977: Evolution of Norwegian-Greenland Sea. Geol. Soc. Am. Bull., 88, 969-999.

Talwani, M., G. Udintsev, et al, 1976: Initial reports of the deep sea drilling project, vol. 38, Washington, D.C. (U.S. Government Printing Office).

Thayer, R.E., A: Björnsson, L. Alvarez & J.F. Hermance, 1981: Magma genesis and crustal spreading in the northern neovolcanic zone of Iceland: telluric-magnetotelluric constraints. Geophys. J.R. astr. Soc., 65, 423-442.

Thomson, C.J. & D. Gubbins, 1981: Three-dimensional lithospheric modelling at NORSAR: Linearity of the method and amplitude variations from the anomalies. Geophys. J.R. astr. Soc., in press.

Thorarinsson, S., 1965: The median zone of Iceland. In: The World Rift System, UMP Symposium, Ottawa, Canada. Geol. Surv. Canada Pap. 66-14, 187-211.

Thorarinsson, S. & K. Sæmundsson, 1979: Volcanic activity in historical time. Jökull, 29, 29-36.

Tozer, D.C., 1972: The present thermal state of the terrestrial planets. Phys. Earth Planet. Int., 6, 182-197.

Tryggvason, E. & M. Båth, 1961: Upper crustal stucture of Iceland. J. Geophys. Res., 66, 1913-1925.

Tryggvason, E., 1964: Arrival times of P-waves and upper mantle structure. Bull. Seis. Soc. Am., 54, 727-736.

Vogt, P.R., 1974: The Iceland phenomenon: Imprints of a hot spot on the ocean crust, and implications for flow below plates. In: Geodynamics of Iceland and the North Atlantic Area (Kristjansson, ed.), D. Reidel Publ. Co., Hingham Mass., 105-126.

Vogt, P.R., 1979: Global magmatic episodes: New evidence and implications of the steady state mid-ocean ridge. Geology, 7, 93-98.

Walker, G.P.L., 1960: Zeolite zones and dyke distribution in relation to the structure of the basalts in eastern Iceland. J. Geol., 68, 515-528.

Walker, G.P.L., 1972: Compound and simple lava flows and flood basalts. Bull. Volcanol., 35, 579-590.

Ward, P.L., 1971: New interpretation of the geology of Iceland. Bull. Geol. Soc. Am., 82, 2991-3012.

Wiggins, R.A., 1972: The general linear inverse problem: implications of surface waves and free oscillations for earth structure. Rev. Geophys. Space Phys., 10, 251-285.

Wilson, J.T., 1963: A possible origin of the Hawaiian Islands. Can. J. Phys., 41, 863.

Wyss, M., 1980: Hawaiian rifts and recent Icelandic volcanism: Expressions of plume-generated radial stress fields. J. Geophys., 47, 19-22.

Yuen, D.A., W.R. Peltier & G. Schubert, 1981: On the existence of a second scale of convection in the upper mantle. Geophys. J.R. astr. Soc., 65, 171-190.

Zindler, A., S.R. Hart, F.A. Frey & S.P. Jakobsson, 1979: Nd and Sr isotope ratios and rare earth element abundances in Reykjanes Peninsula basalts: Evidence for mantle heterogeneity beneath Iceland. Earth Planet. Sci. Lett., 45, 249-262.

Zverev, S.M., I.V. Litvinenko, G. Palmason, G.A. Yaroshevskaya & N.N. Osokin, 1980: A seismic crustal study of the axial rift zone in southwest Iceland. J. Geophys., 47, 202-210.

APPENDIX A

Appendix to Chapter 3

A.1 The stochastic inverse operator

A.2 The covariance-resolution relation

A.1 The stochastic inverse operator H

$$H = C_{xx}A^t(AC_{xx}A^t+C_{ee})^{-1} \tag{A.1}$$

and we want to show that H also may be written as

$$H = C_{xx}(A^tC_{xx}A+C_{ee})^{-1}A^t \tag{A.2}$$

Since from the fundamental decomposition theorem (Lanczos, 1961), the matrix A can be decomposed into two orthogonal matrices U and V of eigenvectors and a diagonal matrix Λ of eigenvalues, $A = U\Lambda V^t$, $A^t = V\Lambda U^t$, eq. (A.1) may be written as

$$\begin{aligned} H &= C_{xx}V\Lambda U^t(U\Lambda V^tC_{xx}V\Lambda U^t+C_{ee})^{-1} \\ &= C_{xx}V\Lambda U^t(U(C_{xx}\Lambda^2+C_{ee})U^t)^{-1} \\ &= C_{xx}V\Lambda U^t(U^t)^{-1}(C_{xx}\Lambda^2+C_{ee})^{-1}U^{-1} \\ &= C_{xx}V\Lambda(C_{xx}\Lambda^2+C_{ee})^{-1}U^t \end{aligned}$$

Analogously for eq. (A.2)

$$\begin{aligned} H &= C_{xx}(V\Lambda U^tC_{xx}U\Lambda V^T+C_{ee})^{-1}V\Lambda U^T \\ &= C_{xx}V(C_{xx}\Lambda^2+C_{ee})^{-1}V^tV\Lambda U^t \\ &= C_{xx}V\Lambda(C_{xx}\Lambda^2+C_{ee})^{-1}U^t \end{aligned}$$

Q.e.d.

A.2 The covariance-resolution relationship

$$C_\delta = \sigma_d^2 HH^t = \sigma_d^2 R(A^tA+\theta^2 I)^{-1} \tag{A.3}$$

As in Appendix A.1 we use the fundamental decomposition theorem.

$$R = (A^tA+\theta^2 I)^{-1}A^tA = (V\Lambda^2V^t+\theta^2 I)^{-1}V\Lambda^2V^t$$

$$R = V(\Lambda^2+\theta^2 I)^{-1}\Lambda^2V^t = V\Lambda^2(\Lambda^2+\theta^2 I)^{-1}V^t = R^t \tag{A.4}$$

Substituting (A.4) in (A.3) and further decomposing (A.3), we obtain

$$C_\delta = \sigma_d^2 V(\Lambda^2+\theta^2 I)^{-1}\Lambda^2V^tV(\Lambda^2+\theta^2 I)^{-1}V^t$$

$$C_\delta = \sigma_d^2 V(\Lambda^2+\theta^2 I)^{-2}\Lambda^2V^t$$

$$= \sigma_d^2 V\Lambda^2(\Lambda^2+\theta^2 I)^{-2}V^t = C_\delta{}^t \tag{A.5}$$

Eqs. (A.4) and (A.5) tell us that both R and C_δ are symmetric.

Now we define $R_d = \Lambda^2(\Lambda^2+\theta^2 I)^{-1}$, then

$$R_d - R_d{}^2 = \Lambda^2(\Lambda^2+\theta^2 I)^{-1} - \Lambda^4(\Lambda^2+\theta^2 I)^{-2}$$

$$= \Lambda^2(\Lambda^2+\theta^2 I)^{-1}(I-\Lambda^2(\Lambda^2+\theta^2 I)^{-1})$$

$$= \Lambda^2(\Lambda^2+\theta^2 I)^{-1}\theta^2 I(\Lambda^2+\theta^2 I)^{-1}$$

$$= \theta^2\Lambda^2(\Lambda^2+\theta^2 I)^{-2} \qquad \text{or}$$

$$\Lambda^2(\Lambda^2+\theta^2 I)^{-2} = \frac{1}{\theta^2}(R_d - R_d{}^2) \tag{A.6}$$

Putting (A.6) into (A.5), we obtain

$$C_\delta = \sigma_d^2 \, V \frac{1}{\theta^2} (R_d - R_d^2) V^t$$

$$= \frac{\sigma_d^2}{\theta^2} VR_d(I-R_d)V^t = \frac{\sigma_d^2}{\theta^2} (VR_dV^t - VR_dR_dV^t)$$

Now $R = VR_dV^t$ and $R^2 = (VR_dV^t)(VR_dV^t) = VR_dR_dV^t$ which finally gives us

$$C_\delta = \frac{\sigma_d^2}{\theta^2} (R-R^2) \qquad (A.7)$$

APPENDIX B

Appendix to Chapter 4

The S_{300} and N_{300} solutions.

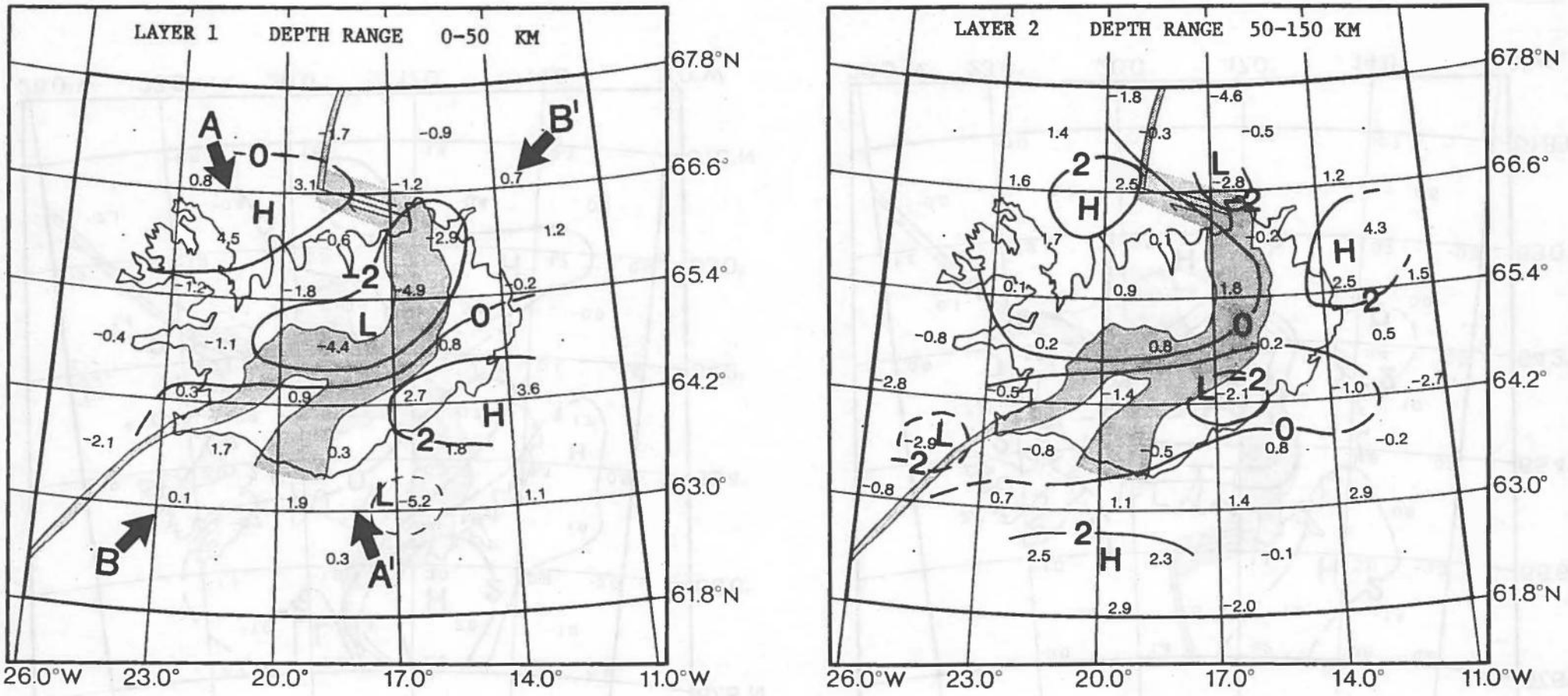

(a) (b)

Fig. B.1 Anomaly maps for S_{300}. For details see caption for Fig. 4.7.

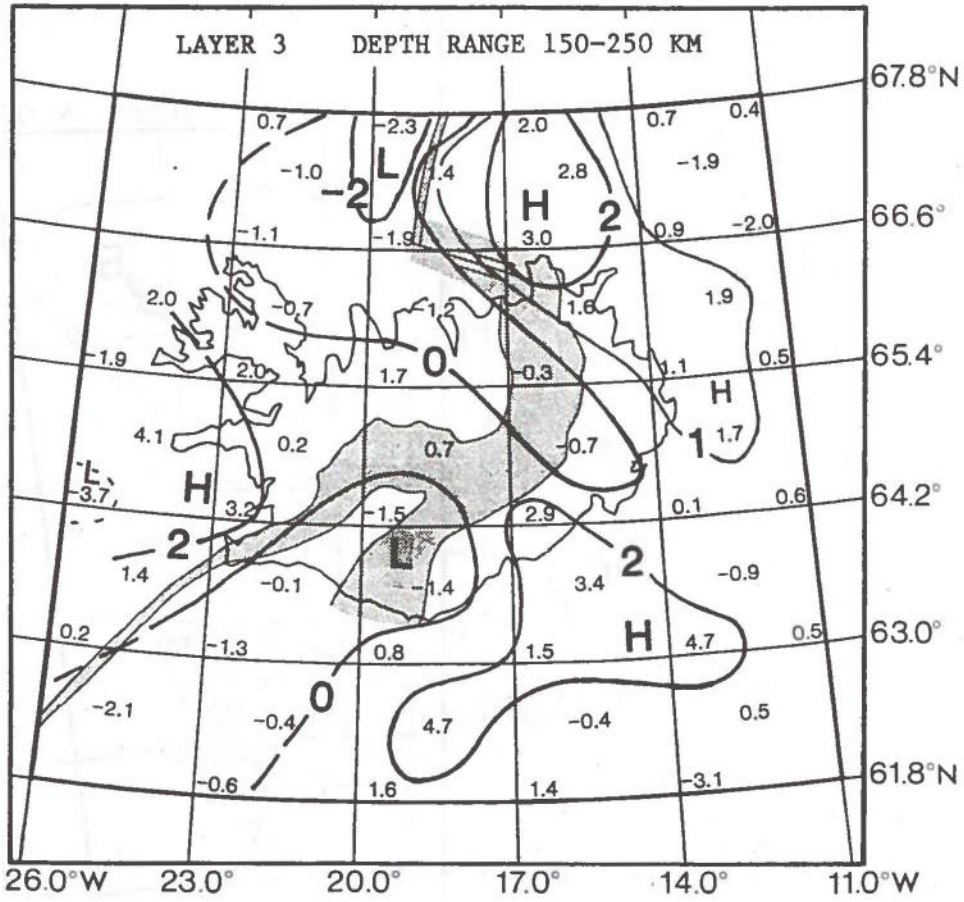

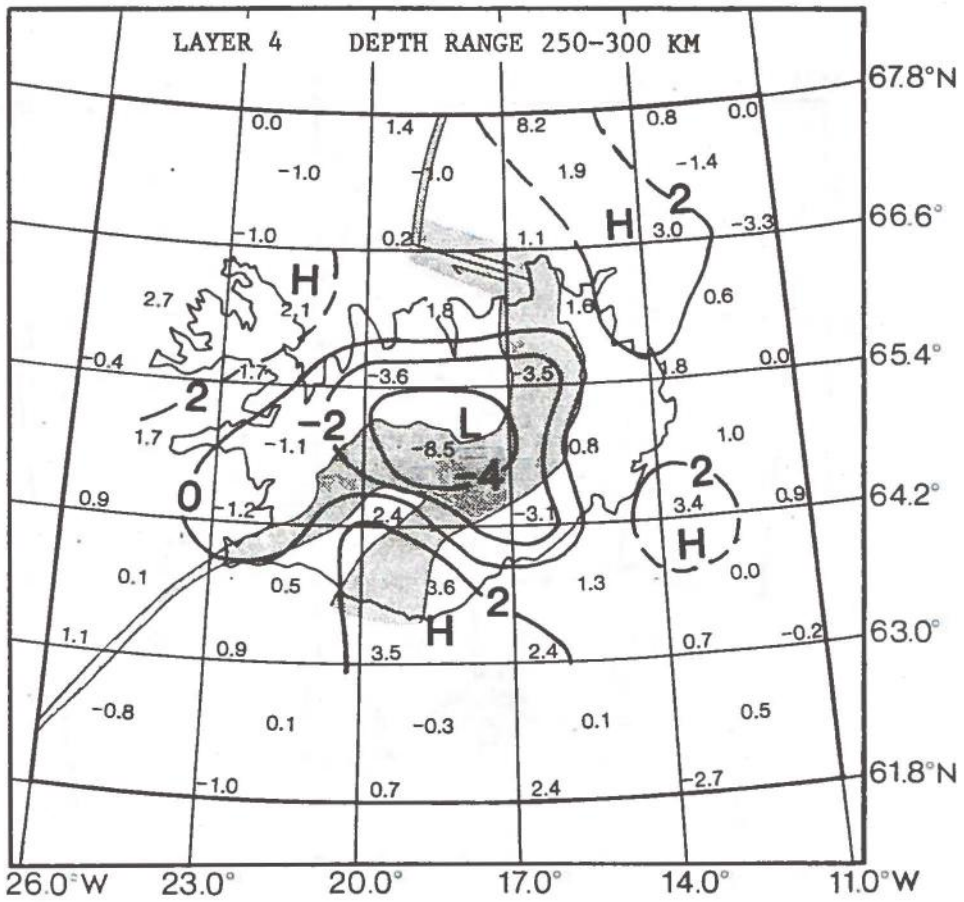

Fig. B.1 - continued

RESOLUTION DISTRIBUTION IN LAYER...1...

0.0	0.0	0.0	0.0	0.0	0.0
	0.0	0.0	0.2	0.1	0.0
0.0	0.1	0.6	0.6	0.3	0.0
	0.0	0.5	0.7	0.6	0.1
0.0	0.4	0.7	0.8	0.7	0.0
	0.1	0.6	0.7	0.6	0.2
0.0	0.6	0.7	0.6	0.5	0.0
	0.2	0.6	0.7	0.5	0.0
0.0	0.2	0.6	0.4	0.1	0.0
	0.0	0.0	0.2	0.0	0.0
0.0	0.0	0.0	0.0	0.0	0.0

RESOLUTION DISTRIBUTION IN LAYER...2...

0.0	0.0	0.1	0.3	0.0	0.0
	0.0	0.2	0.5	0.4	0.0
0.0	0.3	0.6	0.7	0.6	0.0
	0.0	0.5	0.7	0.6	0.5
0.0	0.5	0.7	0.7	0.7	0.3
	0.4	0.6	0.7	0.7	0.5
0.1	0.6	0.7	0.7	0.6	0.2
	0.5	0.6	0.7	0.6	0.2
0.1	0.6	0.7	0.7	0.3	0.0
	0.0	0.4	0.5	0.1	0.0
0.0	0.0	0.2	0.1	0.0	0.0

RESOLUTION DISTRIBUTION IN LAYER...3...

0.0	0.1	0.5	0.5	0.4	0.1
	0.0	0.4	0.7	0.6	0.3
0.0	0.5	0.7	0.7	0.7	0.4
	0.2	0.6	0.7	0.7	0.7
0.2	0.6	0.7	0.8	0.7	0.6
	0.5	0.7	0.8	0.7	0.6
0.5	0.6	0.7	0.8	0.7	0.6
	0.7	0.7	0.7	0.7	0.4
0.4	0.7	0.7	0.7	0.7	0.2
	0.2	0.6	0.5	0.6	0.1
0.0	0.4	0.5	0.4	0.2	0.0

RESOLUTION DISTRIBUTION IN LAYER...4...

0.0	0.2	0.3	0.3	0.3	0.1
	0.0	0.2	0.4	0.4	0.1
0.0	0.3	0.4	0.4	0.5	0.3
	0.2	0.3	0.4	0.4	0.4
0.2	0.4	0.5	0.6	0.5	0.5
	0.1	0.4	0.5	0.4	0.4
0.2	0.4	0.5	0.6	0.5	0.4
	0.3	0.3	0.4	0.4	0.2
0.2	0.4	0.5	0.5	0.5	0.1
	0.1	0.3	0.2	0.3	0.1
0.0	0.3	0.4	0.1	0.3	0.0

STD-ERR. DISTRIBUTION IN LAYER...1...

0.0	0.3	0.5	1.0	0.3	0.2
	0.1	0.4	1.3	0.9	0.2
0.1	1.3	1.7	1.6	1.9	0.3
	0.3	1.3	1.1	1.1	0.8
0.3	2.0	1.8	1.4	1.4	0.8
	0.8	1.3	1.2	1.3	1.1
0.7	1.5	1.5	1.7	2.0	0.4
	1.1	1.1	1.1	1.3	0.4
0.3	1.9	1.6	2.1	1.0	0.3
	0.2	0.6	1.2	0.3	0.1
0.1	0.4	0.4	0.3	0.3	0.1

STD-ERR. DISTRIBUTION IN LAYER...2...

0.0	0.4	1.1	1.9	0.9	0.2
	0.1	1.2	1.3	1.4	0.7
0.2	2.0	1.3	1.3	1.6	0.7
	0.5	1.0	1.0	0.9	1.5
0.5	1.6	1.3	1.3	1.4	1.8
	1.4	0.9	1.0	1.0	1.4
1.4	1.2	1.3	1.4	1.3	1.6
	1.3	0.9	1.0	0.9	1.3
0.9	1.4	1.3	1.3	1.8	0.4
	0.6	1.5	1.4	1.0	0.2
0.1	0.6	2.0	1.1	0.4	0.1

STD-ERR. DISTRIBUTION IN LAYER...3...

0.2	1.6	2.0	1.9	2.0	1.4
	0.2	1.4	1.3	1.3	1.6
0.3	1.8	1.2	1.2	1.3	2.2
	1.4	0.9	0.9	0.9	1.3
1.8	1.1	1.2	1.3	1.3	2.0
	1.5	0.8	0.8	0.9	1.5
1.9	1.3	1.3	1.3	1.3	2.2
	1.4	1.0	0.9	0.9	1.6
1.8	1.3	1.3	1.3	1.5	2.0
	1.4	1.4	1.6	1.4	0.9
0.5	2.0	2.1	2.2	1.7	0.3

STD-ERR. DISTRIBUTION IN LAYER...4...

0.2	1.7	2.2	1.9	2.1	1.6
	0.3	1.3	1.6	1.6	1.1
0.5	1.9	2.0	1.9	1.9	2.1
	1.2	1.3	1.3	1.3	1.7
1.7	1.8	1.9	2.0	1.9	2.4
	1.1	1.3	1.3	1.4	1.6
1.9	1.9	2.1	2.0	2.0	2.3
	1.6	1.3	1.4	1.3	1.4
1.4	1.8	2.0	2.0	2.0	1.4
	1.2	1.4	1.3	1.5	0.8
0.7	2.3	2.4	1.6	1.9	0.5

Table B.1 Resolution and standard error for model S_{300}. These data are also plotted in Fig. 4.5.

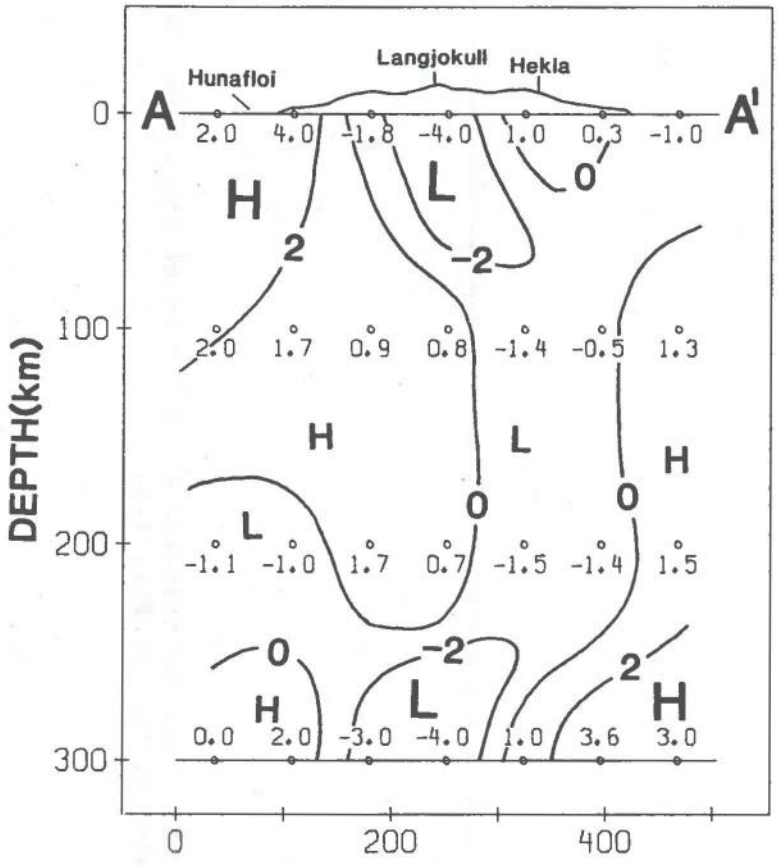

CROSS SECTION A-A' THROUGH THE S_{300} MODEL BOX

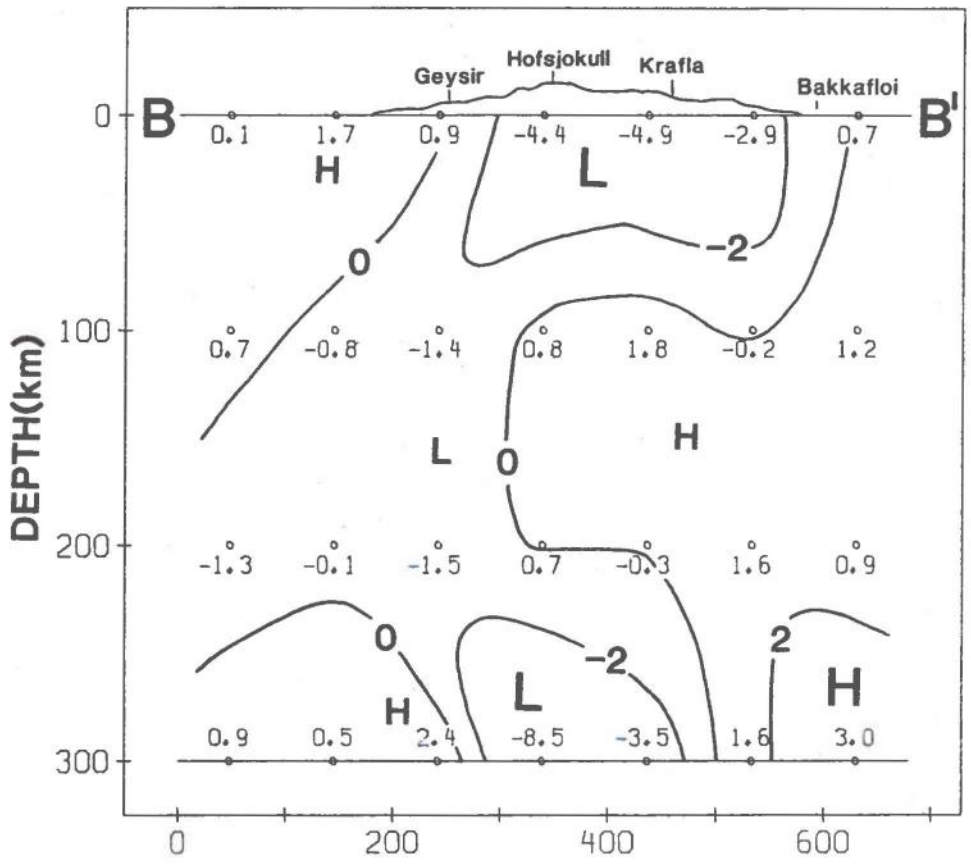

CROSS SECTION B-B' THROUGH THE S_{300} MODEL BOX

Fig. B.2 The cross sections span the latitude range from 63.0°N to 66.0°N, from NW to SE (A-A') and from SW to NE (B-B'). The depth to distance ratio is 2:1.

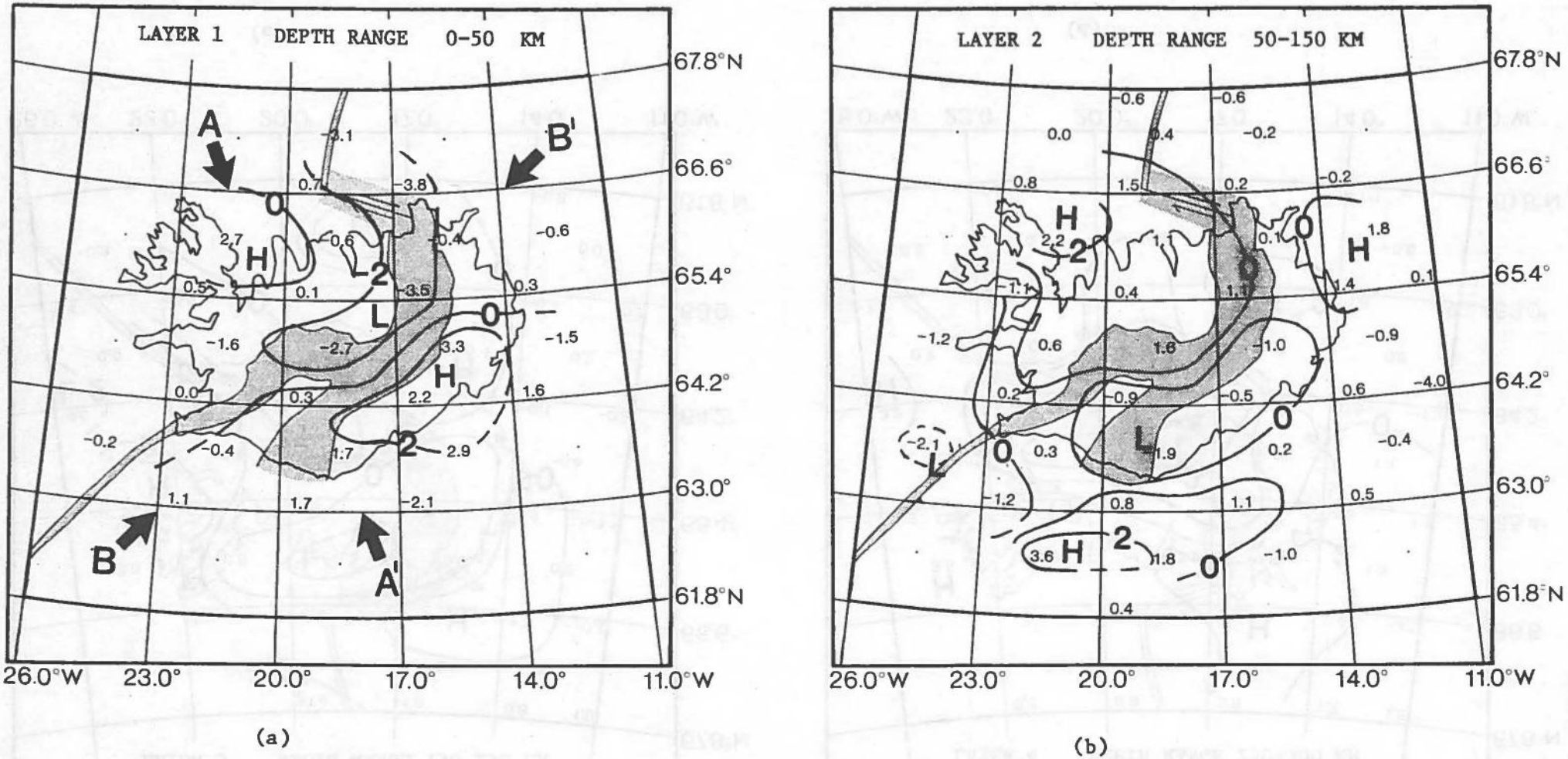

Fig. B.3 Anomaly maps for N_{300}. For details see caption for Fig. 4.7.

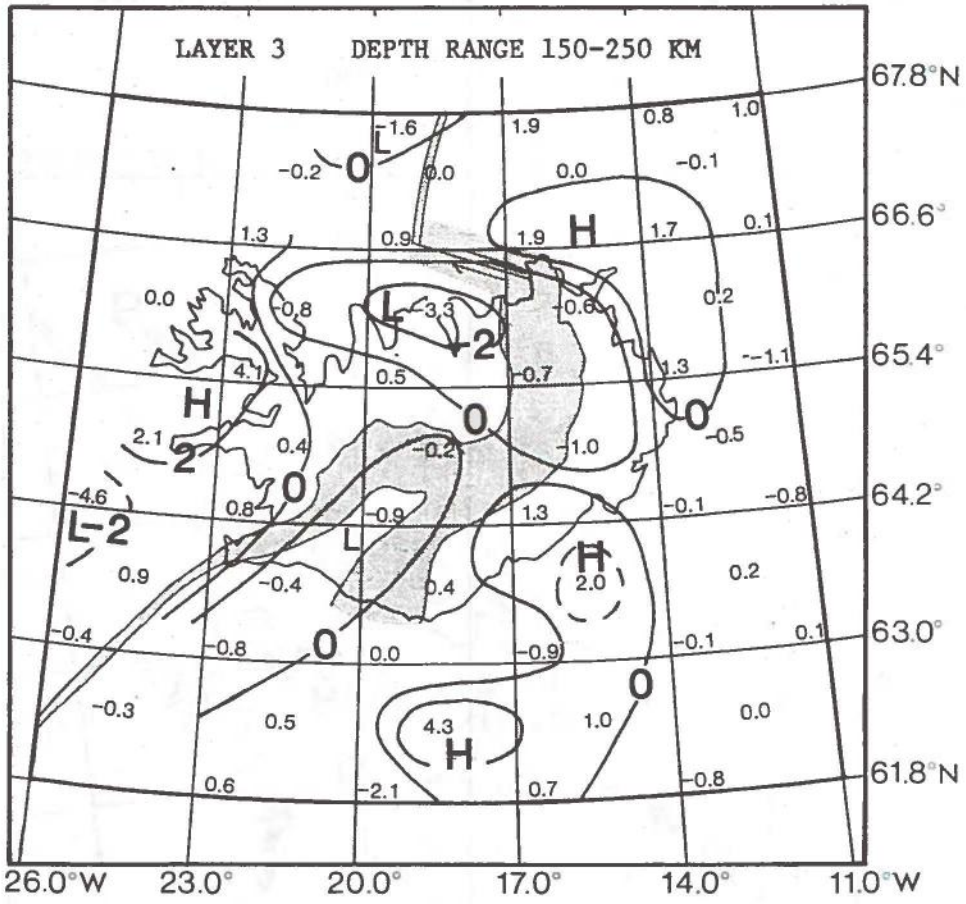

(c)

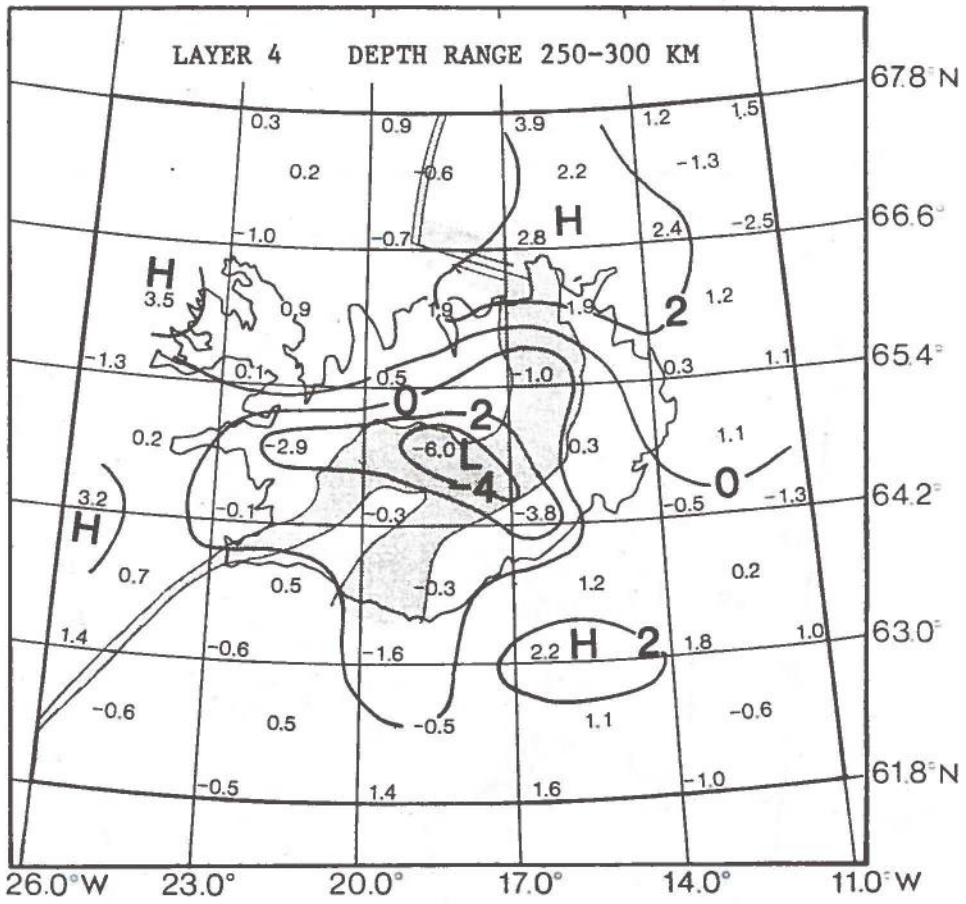

(d)

Fig. B.3 - continued.

RESOLUTION DISTRIBUTION IN LAYER...1...

0.0	0.0	0.0	0.0	0.0	0.0
	0.0	0.0	0.0	0.0	0.0
0.0	0.0	0.8	0.8	0.0	0.0
	0.0	0.6	0.8	0.8	0.0
0.0	0.0	0.8	0.9	0.8	0.0
	0.0	0.8	0.8	0.8	0.2
0.0	0.8	0.9	0.9	0.7	0.0
	0.1	0.8	0.8	0.7	0.0
0.0	0.1	0.9	0.6	0.0	0.0
	0.0	0.0	0.0	0.0	0.0
0.0	0.0	0.0	0.0	0.0	0.0

RESOLUTION DISTRIBUTION IN LAYER...2...

0.0	0.0	0.0	0.2	0.0	0.0
	0.0	0.2	0.7	0.5	0.0
0.0	0.0	0.8	0.9	0.8	0.0
	0.1	0.6	0.9	0.9	0.6
0.0	0.7	0.9	0.9	0.9	0.2
	0.6	0.8	0.9	0.9	0.7
0.0	0.9	0.9	0.9	0.8	0.2
	0.7	0.9	0.9	0.8	0.3
0.0	0.8	0.9	0.8	0.1	0.0
	0.0	0.5	0.7	0.1	0.0
0.0	0.0	0.1	0.0	0.0	0.0

RESOLUTION DISTRIBUTION IN LAYER...3...

0.0	0.0	0.7	0.6	0.5	0.1
	0.0	0.5	0.8	0.8	0.4
0.0	0.6	0.9	0.9	0.9	0.2
	0.0	0.8	0.9	0.9	0.9
0.0	0.8	0.9	0.9	0.9	0.8
	0.7	0.9	0.9	0.9	0.8
0.7	0.9	0.9	0.9	0.9	0.7
	0.8	0.9	0.9	0.9	0.5
0.6	0.8	0.9	0.9	0.8	0.0
	0.2	0.7	0.6	0.8	0.0
0.0	0.5	0.7	0.4	0.1	0.0

RESOLUTION DISTRIBUTION IN LAYER...4...

0.0	0.2	0.6	0.6	0.4	0.3
	0.0	0.3	0.6	0.7	0.3
0.0	0.5	0.7	0.7	0.8	0.5
	0.4	0.6	0.7	0.7	0.7
0.2	0.6	0.8	0.8	0.8	0.7
	0.2	0.7	0.8	0.8	0.6
0.6	0.7	0.8	0.8	0.8	0.6
	0.6	0.7	0.7	0.7	0.5
0.5	0.8	0.8	0.8	0.8	0.3
	0.3	0.6	0.4	0.6	0.1
0.0	0.5	0.6	0.2	0.5	0.0

STD-ERR. DISTRIBUTION IN LAYER...1...

0.0	0.0	0.0	0.0	0.0	0.0
	0.0	0.0	1.4	0.0	0.0
0.0	0.0	1.1	1.0	0.0	0.0
	0.0	1.2	0.8	0.8	0.4
0.0	0.7	1.1	0.8	1.2	0.0
	0.0	1.0	0.9	0.9	1.2
0.0	1.1	0.8	0.9	1.6	0.0
	0.7	0.8	0.8	1.1	0.0
0.0	1.0	0.9	2.0	0.0	0.0
	0.0	0.0	0.0	0.0	0.0
0.0	0.0	0.0	0.0	0.0	0.0

STD-ERR. DISTRIBUTION IN LAYER...2...

0.0	0.0	0.3	1.8	0.0	0.0
	0.0	1.1	1.2	1.5	0.0
0.0	0.5	1.2	1.0	1.5	0.0
	0.0	1.3	0.8	0.8	1.4
0.0	1.7	0.9	0.8	1.1	1.9
	1.4	0.8	0.8	0.8	1.2
0.0	1.1	0.8	0.9	1.5	1.8
	1.3	0.8	0.7	1.1	1.3
0.0	1.4	1.1	1.1	1.1	0.0
	0.0	1.4	1.3	0.9	0.0
0.0	0.0	1.4	0.0	0.0	0.0

STD-ERR. DISTRIBUTION IN LAYER...3...

0.0	0.0	2.0	2.1	2.1	1.0
	0.0	1.4	1.0	1.0	1.5
0.0	2.0	1.2	1.1	1.1	1.8
	0.5	1.0	0.8	0.8	1.0
0.0	1.3	1.0	0.9	1.0	1.7
	1.3	0.8	0.7	0.8	1.2
1.9	1.2	0.9	0.9	1.3	1.8
	1.1	0.9	0.7	0.9	1.5
2.0	1.3	1.1	1.2	1.6	0.5
	1.0	1.2	1.4	1.2	0.6
0.0	2.0	1.8	2.1	0.9	0.0

STD-ERR. DISTRIBUTION IN LAYER...4...

0.0	1.9	2.0	1.8	2.1	2.0
	0.0	1.3	1.5	1.4	1.4
0.0	2.0	1.8	1.7	1.6	2.2
	1.5	1.4	1.4	1.3	1.3
1.7	2.0	1.4	1.5	1.5	1.8
	1.1	1.3	1.1	1.2	1.5
2.1	1.8	1.6	1.4	1.5	2.1
	1.5	1.3	1.3	1.2	1.5
2.0	1.6	1.7	1.6	1.7	1.8
	1.2	1.4	1.5	1.5	1.1
0.0	2.2	2.1	1.6	2.0	0.0

Table B.2 Resolution and standard error for Model N_{300}. These data are also plotted in Fig. 4.5.

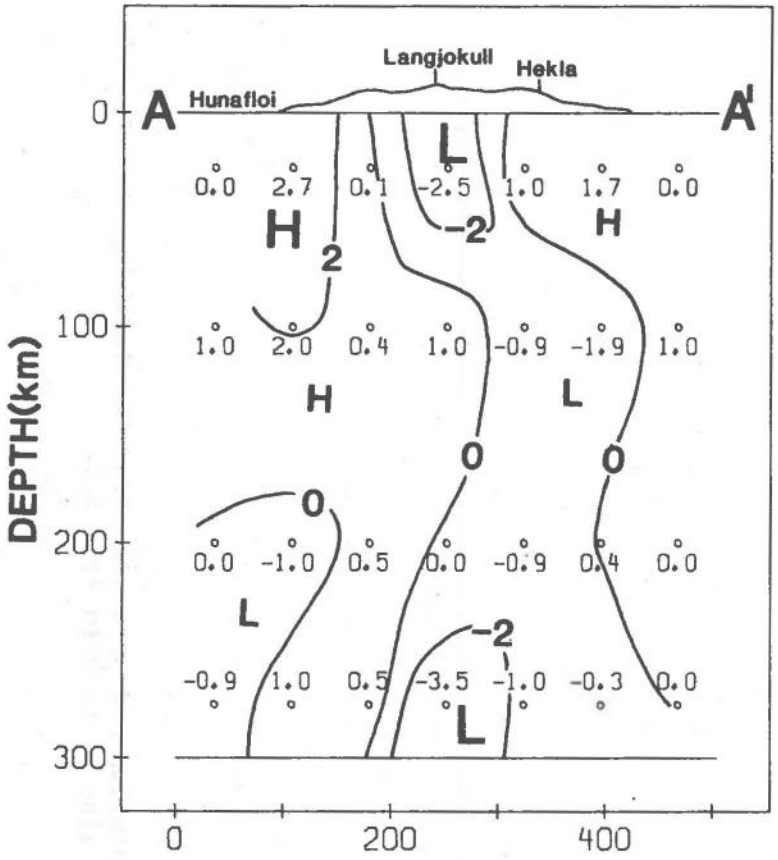

CROSS SECTION A-A' THROUGH THE N_{300} MODEL BOX

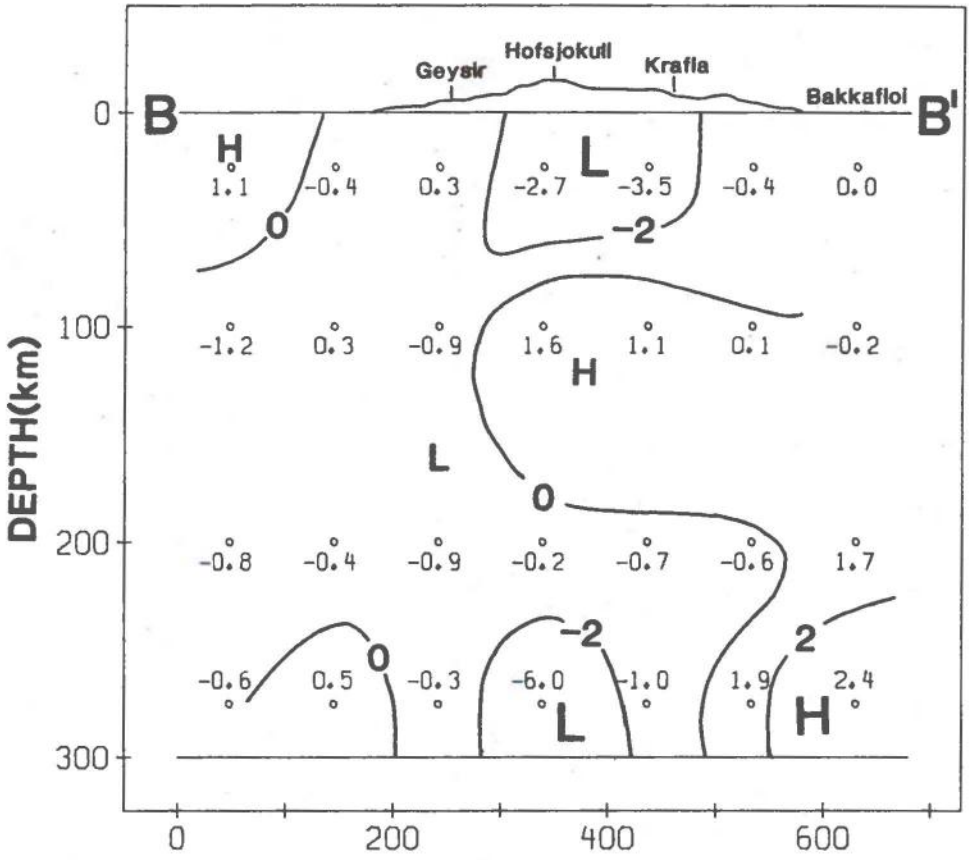

CROSS SECTION B-B' THROUGH THE N_{300} MODEL BOX

Fig. B.4 The cross sections span the latitude range from 63.0°N to 66.0°N, from NW to SE (A-A') and from SW to NE (B-B'). The depth to distance ratio is 2:1.